D I S S E R T A T I O N

Stress and Microstructural Evolution of Electroplated Copper Films

ausgeführt zum Zwecke der Erlangung des akademischen Grades
eines Doktors der technischen Wissenschaften

eingereicht an der Technischen Universität Wien
Fakultät für Elektrotechnik und Informationstechnik

von

M.Sc. Rui Huang

Matrikelnummer: 0627437

Kompetenzzentrum für Automobil-und Industrieelektronik GmbH

Europastrasse 8, A-9524 Villach

München, im November 2012   _____

Kurzfassung

Um die Komplexität und Multifunktionalität von Halbleiterbauelementen weiterentwickeln zu können, lag das Augenmerk auch im vergangenen Jahrzehnt auf einer fortschreitenden Miniaturisierung der zugrunde liegenden Strukturen. Die Realisierung von Bauelementen im Mikro-, Submikro- und Nanobereich erfordert eine Dickenreduzierung der eingesetzten dünnen Filme, wobei Größeneffekte bei solchen Systemen an Bedeutung gewinnen. Für die Entwicklung und Integration geeigneter und zuverlässiger dünner Schichten ist ein umfassendes Verständnis der Materialeigenschaften notwendig. Diese hängen von unterschiedlichen Faktoren wie Abscheidebedingungen, Filmdicke und Temperaturbehandlungsprozessen ab. Die Existenz von Größeneffekten aufgrund von reduzierten Schichtdicken und geometrischen Beschränkungen sowie deren Auswirkung auf das plastische Verformungsverhalten macht eine grundlegende Erforschung dieser Effekte erforderlich.

Eine wesentliche Voraussetzung für die Untersuchung der mechanischen Eigenschaften in dünnen Schichten ist eine geeignete Messanordnung zur Bestimmung der temperaturabhängigen mechanischen Filmspannungen. Im Rahmen dieser Arbeit wurde deshalb ein modernes und innovatives Messgerät zur Filmspannungsmessung entwickelt. Ein Multi-Laser-System zur Erfassung der Substratkrümmung wurde mit einer Temperaturbehandlungskammer kombiniert, in der schnelle und kontrollierte Temperaturänderungen auf der untersuchten Probe ermöglicht wurden. Damit konnte die Entwicklung der mechanischen Spannungen in metallischen Dünnschichtsystemen als Funktion von Temperatur und Zeit bestimmt werden.

In dieser Doktorarbeit wurde das mechanische und thermo-mechanische Verhalten von elektro-chemisch abgeschiedenen Kupferschichten erforscht, wobei die Schwerpunkte auf den Aspekten Mikrostruktur, Filmdicke und Temperaturbehandlung lagen. Die Veränderungen der mechanischen Spannungen bei Schichtdicken von 1,5µm bis 20µm wurden mit Hilfe der Messung der Substratkrümmung systematisch untersucht. Die Kupferschichten zeigten nach der elektro-chemischen Abscheidung und Lagerung bei Zimmertemperatur ein auffälliges „self-annealing" Verhalten. Dabei wurden signifikante Änderungen der Mikrostruktur und des elektrischen Schichtwiderstands beobachtet. Zum ersten Mal konnten eindeutig verschiedene Tendenzen bei dünnen und dicken Kupferschichten hinsichtlich der mechanischen Spannungsentwicklung nachgewiesen werden. Dieser Größeneffekt im Verhalten der mechanischen Spannungen konnte durch die konkurrierenden Mechanismen von Kornwachstum und Versetzungsplastizität erklärt werden. Die experimentellen Messwerte und die im Rahmen dieser Arbeit entwickelten analytischen Modelle wiesen dabei eine gute

Übereinstimmung auf. Des Weiteren wurden die thermisch induzierten Spannungsänderungen in elektro-chemisch abgeschiedenen Kupferschichten im Temperaturbereich zwischen Raumtemperatur und 600°C untersucht. Die nach den Temperaturzyklen auf verschiedene Anlasstemperaturen gemessenen Spannungswerte können nicht mit der erwarteten klassischen Hall-Petch-Beziehung beschrieben werden. Kornwachstum, Versetzungsplastizität oder sogar Diffusionskriechen beeinflussen abwechselnd die Entwicklung der mechanischen Spannung während des Temperprozesses, was dazu führt, dass die Hall-Petch-Beziehung außer Kraft gesetzt wird.

Abstract

Over the past decade, there has been a great deal of motivation to produce semiconductor devices in a smaller scale in order to accomplish the enhanced complexity in multi-functions. The fabrication of devices in the micro, sub-micron or even nanometre scale requires manufacturers to reduce the thickness of thin films, which raises the issue of the size effect of thin films. The successful development of a thin film system relies on a thorough understanding of the material's properties. The quality and mechanical response of thin films depends on many factors, such as deposition conditions, thermal treatment, and film thickness. The existence of size effects in thin films due to film thickness and geometrical constraints, particularly on plasticity, leads to the necessity of exploring the fundamentals of thin films.

A prerequisite for the study of the mechanical properties of thin films is an appropriate measurement setup that is capable of accurately acquiring the film stress data. Therefore an innovated and advanced apparatus which integrates a multiple laser beam technique with a rapid thermal processing (RTP) chamber has been developed in this work and established in order to characterise the stress evolution of metal thin films.

In this work, mechanical and thermo-mechanical behaviours of electroplated copper films are studied, with an emphasis on the aspects of microstructure, film thickness, and annealing temperature. The stress evolution of electroplated copper films with the thickness range of 1.5µm to 20µm was systematically investigated by wafer curvature measurements. Copper thin films, after electroplating deposition and aging at room temperature, show a noticeable self-annealing phenomenon. Microstructure and sheet resistance changes were also observed. A clear disparate tendency of stress evolution in thin and thick copper films was observed for the first time. This strong size effect of stress evolution can be explained by competing mechanisms between grain growth and dislocation plasticity. Furthermore, the results of the analytical modelling also show good agreement with the experimental data. In addition, the thermal stress evolution in electroplated Cu films was investigated from room temperature up to 600°C. However, the residual stresses, after thermal cycles up to different annealing temperatures, do not follow the classical Hall-Petch law as expected. Grain growth, dislocation plasticity, or even diffusional creep alternatively control the stress evolution during the thermal annealing process and thus induce the breakdown of the Hall-Petch law of residual stress.

献□我的父母

To my parents

Acknowledgements

First of all, I would like to thank Prof Tibor Grasser and Dr Hajdin Ceric who gave me academic supervision during my doctoral study over the past few years. I appreciate all the support from them, the fruitful discussions, paper reviewing and academic direction.

I am very grateful to my second supervisor, Prof Gerhard Dehm, at the University of Leoben. He gave me important feedback on my experimental study and I thank him for his time, effort and the encouragement he gave to guide me through.

My special thanks go to Dr Thomas Detzel, my project leader during my work at KAI and Infineon. Whenever there was a difficulty, either technical or non-technical, he was always at my side, supporting me far more than his role as project leader required. I learned so much from him, not only valuable technical knowledge but also the priceless traits of being optimistic, motivated and rational.

Furthermore, I thank Prof Herbert Grünbacher and Josef Fugger for giving me the opportunity to work at KAI, and for providing me with the excellent infrastructure and the great industrial and academic network connecting KAI, Infineon, and TU Vienna.

I would also like to thank all my colleagues who contributed to this work: Dr Werner Robl from Infineon Regensburg, Dr Manfred Schneegans, and Dr Peter Nelle from Infineon Munich for helping me to prepare experimental samples and develop this measurement setup. I must thank Dr Chuck Taylor, Stefan Himmelsbach, Richard Thomson and Dr Thomas Bitzer for their creative ideas during the development of the measurement apparatus. I also thank Dr Javad Zarbakhsh, Stefan Puchner, Martin Smolka, Dr Stefan Wöhlert, Dr Markus Leicht, Marion Roemet, Christian Lechner, Stefan Reimann, Dr Thomas Berthold, Angela Collantes for the helpful discussions, measurements and characterisations, and Dr Thang Nguyen and Dr Bala Karunamurthy for editing and correcting my thesis. Furthermore, my appreciation extends to all my other colleagues at KAI for providing such a very supportive and friendly environment.

Last but not least, I would like to express my deep gratitude to my parents for their endless love. They have made all of this possible.

Contents

List of Figures

List of Tables

Acronyms

MEMS .... **M**icro-**E**lectro-**M**echanical **S**ystems

RTP .... **R**apid **T**hermal **P**rocessing

IC .... **I**ntegrated **C**ircuits

SEM .... **S**canning **E**lectron **M**icroscopy

TEM .... **T**ransmission **E**lectron **M**icroscopy

FIB .... **F**ocused **I**on **b**eam

EBSD .... **E**lectro**n** **B**ack**s**catter **D**iffraction

FEM .... **F**inite **E**lement **M**ethod

FCC .... **F**ace-**c**entred **C**ubic

CCD .... **C**harge **C**oupled **D**evice

CVD .... **C**hemical **V**apour **D**eposition

MSA .... **M**ethane **S**ulphonic **A**cid

CTE .... **C**oefficient of **T**hermal **E**xpansion

STEM .... **S**canning **T**ransmission **E**lectron **M**icroscopy

EDX .... **E**nergy **D**ispersive **X**-ray spectroscopy

1 Introduction

Nowadays, a variety of electronic and information technologies have become essential parts of modern daily life. All these technologies are based on integrated circuits (IC). The development of integrated circuits over the past decades is one of the most amazing achievements in the history of technology. Due to the application requirements of constantly reducing IC size and its enhanced complexity, most materials used in advanced microelectronic devices are in the form of thin films [1]. Most of components in devices are fabricated in the micro-scale from thin films integrated together by using numerous techniques in semiconductor industry [2]. For instance, smart power technology provides on-chip integration of power and logic devices, which leads to a particular challenge in process integration. Metallisation, especially when involved in the power devices, has a critical impact on the performance and reliability of the entire device.

Thin films are chosen in semiconductor industry primarily because of their unique electronic and thermal properties. Mechanical characteristics of thin films, however, are indeed very important because they are frequently subjected to large mechanical stresses during the manufacturing processes, reliability tests and by the electronic end-uses.

In general, mechanical stress in thin films can be divided into two types: intrinsic and extrinsic stresses [3-6]. Intrinsic stress is developed during film deposition and growth, or storage. Extrinsic stress is induced by external processing effects, such as thermal annealing or pulsed electrical cycling. Large mechanical stresses are unfavourable in semiconductor devices as they cause material degradation, that is, voids, cracks or delaminations which may lead to the failure of the final product. Thus, it is extremely important to fabricate robust thin films in devices which can tolerate the large mechanical stresses. The achievement of gaining this fundamental understanding will benefit industrial manufacturing and testing from paving the way forward for the engineering design rules of semiconductor devices. For example, for power devices used in automobiles, thicker metallisation can tolerate a larger power density. As a drawback, thicker metallisation usually has a lower yield stress due to its coarse microstructure. This study helps to determine the suitable film thickness and grain structure for the designed metallisation. Regarding the electroplating itself, different electrolytes contain different organic and inorganic components that involve different sorts of impurities, which play an important role in determining the subsequent stress evolution. Therefore, it is vital to choose the proper electrolyte for electroplating. Furthermore, during the thermal annealing process of thin films, different annealing temperatures result in different microstructures which represent its maximum bearable stress status. With the investigation of thermal annealing, the optimal

annealing temperature can be advised for the post-processing after film deposition. Therefore, understanding and controlling the mechanical properties of thin films is of paramount importance to improving the reliability and lifetime of devices which is the ultimate target for quality management.

In addition to these tremendous technological incentives, there is also a strong academic motivation to study the mechanical properties of thin films, which are generally very different from those of bulk materials. This phenomenon is usually referred to as the size effect and reflects the scaling laws of physical properties [7-9]. Generally, the size effect can be attributed to dimensional and microstructural constraints on dislocation activity in thin films [10, 11]. Dimensional constraints are imposed by the film surface and interfaces. It is important to explore how the grain structure of metallic films, seen in cross-section view as well as from a top view, evolves during both deposition and post-deposition processing. The issues raised here are applicable to all polycrystalline metallic thin films, irrespective of application. However, our major interest in grain microstructure stems largely from reliability concerns about metallisation and metal films, and this is an important issue in microelectronics. These concerns have created the incentive to study the contact and interconnect metal microstructure, both in blanket films and in films confined to line, fill trenches and via holes.

Copper has frequently been used to replace aluminium for interconnect applications in semiconductor devices. This is because it has higher electrical conductivity, increased electro-migration resistance and better thermal conductivity [12-21]. Electroplating of copper has been demonstrated to be one of the best methods both for high-performance logic devices using dual damascene technology and for power devices using pattern plating technology [22-25].

The objective of the current work is to extend the fundamental understanding of the mechanical mechanisms which control the elastic-plastic properties of thin metal films, particularly, in this case, of Cu films. The preparation of blanket Cu samples has been specially established. A prototype measurement setup has been developed to characterise the stress evolution of Cu films. The stress has been measured at room temperature after the Cu film deposition and at elevated temperatures during thermal cycles. The mechanical properties have then been correlated with the microstructure of Cu films. Experimental results have also been compared with existing theoretical models, and show a quantitatively good agreement.

2 Fundamentals of material mechanics

In both front-end and back-end processes of the semiconductor industry, mechanical issues always arise and subsequently reflect on reliability qualifications. The fabrication of a wafer that contains thousands of chips is a typical example of a composite structure that undergoes thermal loading. It is composed of different sorts of conducting and insulating layers and evolves non-homogeneous thermal distributions. Because of the geometry of its construction, the material composition, and the thermal expansion mismatch of different layers, stress is generated inside the wafer/chip system while it is being manufactured, assembled in an electronic package and then used. The complexity of a chip layer structure is shown in Figure 2.1.
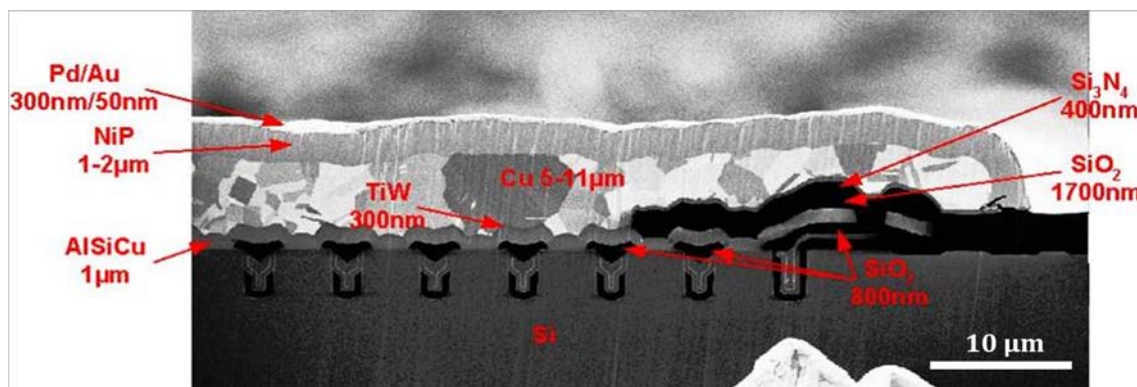
Figure 2.1: Cross-section of the SMART technology chip

The root cause of most failure modes of a package, either induced by thermal or electrical loads, can be attributed to mechanical phenomena. Stress and strain are the most common parameters used to describe the mechanical properties of materials. Unfortunately it is not a simple and straightforward task to determine stress in a complex multiple layer system. Some compromise solutions can only be derived for a very simple chip structure. Therefore, the finite element method (FEM) has become one of the best alternatives for obtaining numerical results for stress and strain. However, the successful execution of the FEM can be realized only when the material properties of each material used in a chip system have been correctly obtained and a fundamental understanding of material mechanics has been gained.

In this chapter, the fundamentals of material mechanics needed for mechanical analysis are introduced. The chapter begins with an analysis of stress and strain, and follows with a discussion of the relationship between them. The dislocation theory is then presented in Section

2.2. Last but not least, the plasticity of metals will be emphasized by means of strengthening mechanisms in metals.

2.1   Stress and strain relationship

The strength of a material is the key to its ability of withstanding an applied stress, which is the relation between internal forces, deformation, and external loads. Applied external loads generate internal stresses which cause deformations of the material. Mechanical properties of metals usually refer to stress and strain. The plasticity theory and all of the models are based on the formulation of the stress and strain relationship.

2.1.1   Stress and strain analysis

If a force is applied along the direction of elongation, this will induce a normal stress. Normal stress can be categorised according to the direction of the applied force. If the applied force reduces the length of the material in the direction of the applied force, it is compressive stress. The forces pushing in opposite directions can create uniaxial compression which leads to compressive stress of the material in the direction of the applied forces. Conversely, if the applied forces have the effect of elongating the material along the axis of the applied forces by pulling, this generates tensile stress in the material. By contrast, shear stress is caused by a pair of opposing forces acting along two opposite surfaces of the material. The resultant shear stress is generated by the faces of the material sliding relative to each other.

Uniaixial stress is expressed by the equation:

$$\sigma = \frac{F}{A} \tag{2.1}$$

where F is the force acting on the cross-section area A.

Strain is a mathematical term, which is used to describe the deformation percentage. For uniaxial loading, strain ε can be expressed as the displacement ΔL to the original length L of the material.

$$\varepsilon = \frac{\Delta L}{L} \tag{2.2}$$

In general, a force will not be uniformly distributed over any cross section of a body [26] as illustrated in Figure 2.2.
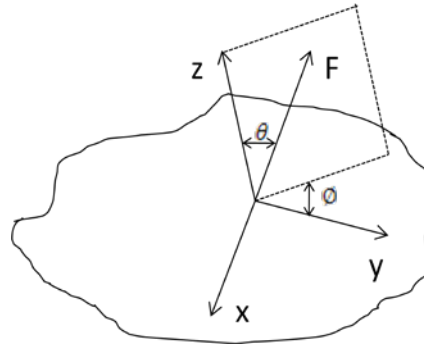
Figure 2.2: Resolution of total stress into its components [26]

Instead, it usually acts over an area with some arbitrary angle. Nevertheless, this total stress can be split into two components as mentioned above: a normal stress; and a shear stress. The force F is inclined at an angle θ with the normal z to the plane of the area A. Additionally, an additional plane containing the normal z and F intersects the plane A that makes an angle $\emptyset$ with the y axis. The normal stress can be calculated by the following formula:

$$\sigma = \frac{F}{A}\cos\theta \tag{2.3}$$

The shear stress in the plane A can be expressed as:

$$\tau = \frac{F}{A}\sin\theta \tag{2.4}$$

The shear stress can be further decomposed into components parallel to the x and y axes.

$$\tau_x = \frac{F}{A}\sin\theta\sin\emptyset \tag{2.5}$$

$$\tau_y = \frac{F}{A}\sin\theta\cos\emptyset \tag{2.6}$$

In conclusion, a given plane has one normal stress and two shear stresses being applied to it.

We can further extend the stress analysis to a three-dimensional case [27]. The general condition of the constraints of a cubic element is shown in Figure 2.3. For normal stress, only one index is needed which identifies the direction of the stress. For shear stress, the first index denotes the normal direction of the plane on which the stress is being applied and the second index indicates the direction of the stress.
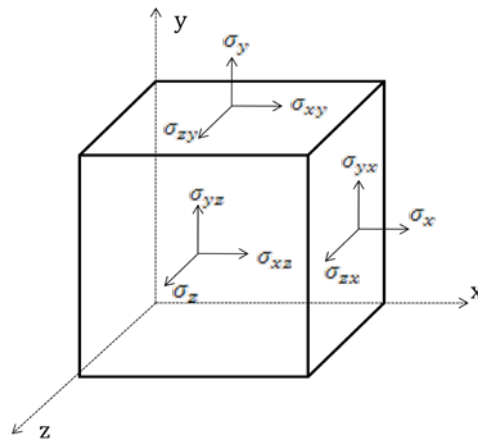
Figure 2.3: Stress components on a cubic element [27]

The general three-dimensional state of stress consists of three unequal principal stresses. All the components of the stress can be expressed as a second-rank tensor.

$$\sigma_{ij} = \begin{bmatrix} \sigma_x & \tau_{xy} & \tau_{xz} \\ \tau_{yx} & \sigma_y & \tau_{yz} \\ \tau_{zx} & \tau_{zy} & \sigma_z \end{bmatrix} = \begin{bmatrix} \sigma_{11} & \sigma_{12} & \sigma_{13} \\ \sigma_{21} & \sigma_{22} & \sigma_{23} \\ \sigma_{31} & \sigma_{32} & \sigma_{33} \end{bmatrix} \tag{2.7}$$

The stress tensor is symmetric due to the fact that $\tau_{xy} = \tau_{yx}$, $\tau_{xz} = \tau_{zx}$, and $\tau_{zy} = \tau_{yz}$.

Similarly to the stress analysis, the strain can also be divided into normal strain and shear strain. As shown in Figure 2.4(a), the elongation of a cubic element per unit of length refers to normal strain $\varepsilon_x = \frac{\Delta L}{L}$. The angle change γ due to the distortion of the cubic element can be represented by shear strain $\varepsilon_{xy} = \varepsilon_{yx} = \gamma$, as shown in Figure 2.4(b). Similarly to stress, strain is a symmetric second order tensor which can be expressed as:

$$\varepsilon_{ij} = \begin{bmatrix} \varepsilon_x & \varepsilon_{xy} & \varepsilon_{xz} \\ \varepsilon_{yx} & \varepsilon_y & \varepsilon_{yz} \\ \varepsilon_{zx} & \varepsilon_{zy} & \varepsilon_z \end{bmatrix} \tag{2.8}$$
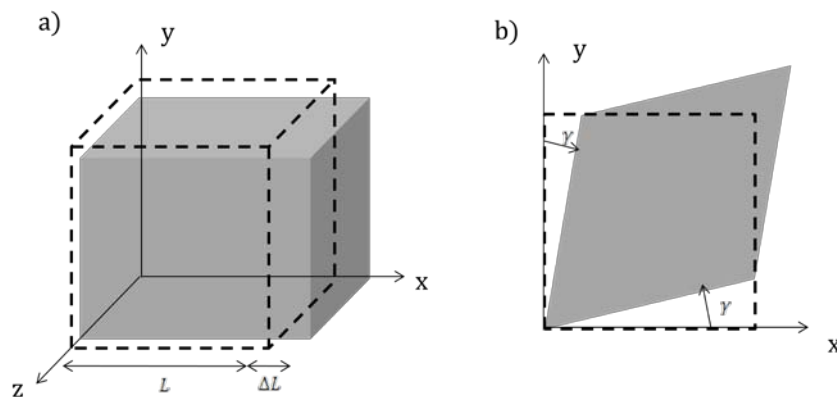
Figure 2.4: Representation of principal deformations of a cubic element [27]. The dotted lines show the structure of the original shape before deformation. The grey areas refer to the deformed shape: a) normal strain; b) shear strain.

The strain tensor is also symmetric, because $\varepsilon_{xy} = \varepsilon_{yx}, \varepsilon_{xz} = \varepsilon_{zx}$ and $\varepsilon_{zy} = \varepsilon_{yz}$. The strain-displacement relations have six equations for three unknown displacement component functions u, v, and w:

$$\varepsilon_x = \frac{\partial u}{\partial x} \tag{2.9}$$

$$\varepsilon_y = \frac{\partial v}{\partial y} \tag{2.10}$$

$$\varepsilon_z = \frac{\partial w}{\partial z} \tag{2.11}$$

$$\varepsilon_{xy} = \frac{1}{2}\left(\frac{\partial u}{\partial y} + \frac{\partial v}{\partial x}\right) \tag{2.12}$$

$$\varepsilon_{yz} = \frac{1}{2}\left(\frac{\partial v}{\partial z} + \frac{\partial w}{\partial y}\right) \tag{2.13}$$

$$\varepsilon_{zx} = \frac{1}{2}\left(\frac{\partial w}{\partial x} + \frac{\partial u}{\partial z}\right) \tag{2.14}$$

Our attention will be focused on thin films whose thicknesses are much less than their lateral dimensions. There is no stress acting perpendicular to the surface of the thin film. Thus, the stress system contains only two normal stresses, σ_x and σ_y , and a shear stress, τ_{xy}, which are also called in-plane stresses. In the case of a thin film, the strain system can be also simplified into two normal strains, ε_x and ε_y, and one shear strain, ε_{xy}. This thesis focuses particularly on a thin film/substrate system. The films deposited on such substrates are much thinner than the thickness of the substrates. Therefore, simple bending mechanics can be adopted to analyze the mechanical properties of such thin film/substrate systems. If the thin film and substrate are isotropic materials, and the external loading is uniform, the bending of the system will be biaxial, which will result in biaxial normal stress and strain in the system: $\sigma_x = \sigma_y$ and $\varepsilon_x = \varepsilon_y$. It must also be noted that the thin film/substrate system is subjected to pure bending. This means that the shear force is zero, and that no torsional or axial loading are present. All stress and strain components which are related to the shear force will not be considered in this study.

2.1.2 Stress-strain curve

The stress-strain curve is the most important means of visually representing the relationship between stress and strain [28]. Figure 2.5 shows a typical stress-strain curve measured by pulling tensile testing. The stress value can be obtained by measuring the applied force and the area of cross section. The strain value can be calculated based on the dimension deformation of the material.
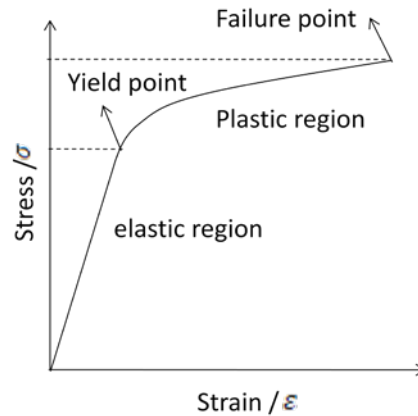
Figure 2.5: An ideal uniaxial stress-strain curve showing elastic and plastic deformation regimes [28]

In Figure 2.5, the first linear region represents the elastic behaviour of a material. The material can recover its initial shape after the loading has been removed. In terms of elasticity, the relation between stress and strain is linear and can be described by the following equation:

$$\sigma = E\varepsilon \tag{2.15}$$

The slope E is commonly known as the elastic modulus or Young's modulus. This relation is also known as Hooke's law. The elastic limit is the maximum stress which will not result in permanent deformation. The stress at yield point is the yield stress for the material. Plasticity or plastic deformation is the further region beyond the yield point. The plastic strain is not recoverable even if the loading is removed. The plastic deformation or plasticity will be described in more detail in section 2.3. The ultimate strength refers to the point on the stress-strain curve corresponding to the stress that generates fracture.

Based on Hooke's law, the stress-strain relation can be extended to the three dimensional case in the Cartesian coordinate system for isotropic materials that have equal elastic properties in all directions [29]. When a tensile stress in x direction σ_x, for example, produces an extension ε_x along the axis, it also produces a contraction, ε_y and ε_z , in the transverse y and z directions, respectively. The transverse strain can be determined as a constant fraction of the strain in the longitudinal direction. This is known as Poisson's ratio, denoted by the symbol v.

$$\varepsilon_x = \frac{\sigma_x}{E} \tag{2.16}$$

$$\varepsilon_y = \varepsilon_z = -\frac{v\sigma_x}{E} \tag{2.17}$$

If we consider a cubic element subjected to normal stresses σ_x, σ_y, σ_z and shear stresses τ_{xy}, τ_{yz}, τ_{zx}, as in Figure 2.3, we can apply the principle of superposition to determine the strain produced by more than one stress component. The stress components are directly proportional to the strain components in accordance with the physics of elastic interaction as follows:

$$\varepsilon_x = \frac{1}{E}\left(\sigma_x - v\sigma_y - v\sigma_z\right) \tag{2.18}$$

$$\varepsilon_y = \frac{1}{E}\left(-v\sigma_x + \sigma_y - v\sigma_z\right) \tag{2.19}$$

$$\varepsilon_z = \frac{1}{E}\left(-v\sigma_x - v\sigma_y + \sigma_z\right) \tag{2.20}$$

The shear stresses acting on the cubic element produce shear strain as below:

$$\varepsilon_{xy} = \frac{\tau_{xy}}{2G} \tag{2.21}$$

$$\varepsilon_{yz} = \frac{\tau_{yz}}{2G} \tag{2.22}$$

$$\varepsilon_{zx} = \frac{\tau_{zx}}{2G} \tag{2.23}$$

where G represents the shear modulus that is usually determined from a torsion test. However, shear stresses are not the focus of this thesis.

Table 2.1 summarizes typical elastic properties of various isotropic materials [26, 30]. Young's modulus E, shear modulus G, and Poisson's ration v are correlated by the equation:

$$G = \frac{E}{2(1+v)} \tag{2.24}$$

Materials	Elastic modulus E (GPa)	Shear Modulus G (GPa)	Poisson's ratio v
Al	70	25	0.33
Cu	120	45	0.36
Ti	117	44.8	0.31
W	400	157	0.27
Fe	150	53	0.28
Al_2O_3	300	160	0.20
SiC	475	123	0.28
Si_3N_4	310	123	0.28

Table 2-1: Typical elastic properties for isotropic materials at room temperature

In the case of plane stress ($\sigma_z = 0$), like that which occurs in a thin plate, the stress can be calculated by the following equations:

$$\sigma_x = \frac{E}{1-v^2}\left(\varepsilon_x + v\varepsilon_y\right) \tag{2.25}$$

$$\sigma_y = \frac{E}{1-v^2}\left(\varepsilon_y + v\varepsilon_x\right) \tag{2.26}$$

Thus, in a thin film/substrate system, biaxial stress ($\sigma_x = \sigma_y$ and $\varepsilon_x = \varepsilon_y$) can be derived as follows:

$$\sigma = \frac{E}{1-v}\varepsilon \tag{2.27}$$

This approach to calculating the stress resulting from elastic strain is usually applied in the mechanical study of a thin film/substrate system. One must keep in mind that this calculation involves several assumptions. Firstly, it is usually valid only in a thin film/substrate system where the film thickness is much less than that of the substrate, and both the thicknesses of the film and substrate are much less than their lateral dimensions. Secondly, materials must be in-plane isotropic. Moreover, only small elastic strains accumulate in the system and therefore no coupling between normal and shear stress occurs.

2.1.3 Yielding criteria for metals

It is crucial to define yielding criteria so that the failure of a material can be predicted. The factor which causes a ductile material (e.g. metals) to yield is quite different from that which causes a brittle material (e.g. ceramics) to yield. Since this thesis only focuses on the mechanical behaviour of metals, this section will be mainly concerned with the yielding criteria for metals.

In uniaxial loading, for instance in a tensile pulling testing, plastic deformation starts at the point of yield stress. In a complex three-dimensional stress state, it is expected that yielding will be related to some particular combination of principal stresses. Unfortunately there is no theoretical method available for calculating the stress components that correlate yielding for a three dimensional state of stress (multiaxial loading) with one-dimensional yield stress (uniaxial loading) from a tension test. The yielding criteria are empirical relationships. At present there are two commonly used yielding criteria for predicting the onset of yielding in ductile metals: the von Mises and the Tresca criteria [31].

The von Mises criterion assumes that yielding will occur when the second invariant J_2 of the stress deviator exceeds a critical value k^2.

$$J_2 = k^2 \tag{2.28}$$

where $J_2 = \frac{1}{6}[(\sigma_1 - \sigma_2)^2 + (\sigma_2 - \sigma_3)^2 + (\sigma_3 - \sigma_1)^2]$, and k is the yield stress in pure shear $(k = \frac{\sigma_y}{\sqrt{3}})$.

Substituting J_2 in terms of the principal stresses gives us the von Mises criterion equation:

$$[(\sigma_1 - \sigma_2)^2 + (\sigma_2 - \sigma_3)^2 + (\sigma_3 - \sigma_1)^2] = 2\sigma_y^2 \tag{2.29}$$

This equation defines the yield surface as a circular cylinder, as shown in Figure 2.6. The yield curve with the deviator plane is a circle.
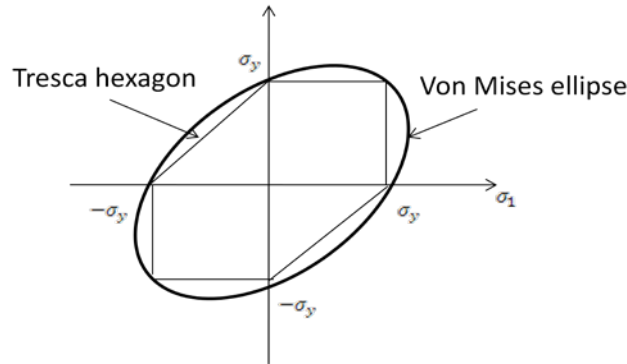
Figure 2.6: Von Mises and Tresca criteria for plane stress condition [31]

In the case of plane stress ($\sigma_3 = 0$), the von Mises criterion becomes:

$$\sigma_1^2 - \sigma_1 \sigma_2 + \sigma_2^2 = \sigma_y^2 \qquad (2.30)$$

This equation represents an ellipse, as shown in Figure 2.6. Originally, the von Mises criterion was proposed because of its mathematical simplicity. Nevertheless, some scientists have attempted to give it physical interpretations. It was suggested by Hencky [32] that yielding starts when the distortion energy reaches a critical value. By contrast, Nadai [33] claimed that yielding begins when the octahedral shear stress reaches a critical value.

The second generally accepted criterion, the Tresca criterion, assumes that yielding occurs when the maximum shear stress reaches the value of the shear stress in the uniaxial tension test.

$$\tau_{max} = \frac{\sigma_1 - \sigma_3}{2} \qquad (2.31)$$

where σ_1 is the algebraically largest and σ_3 is the algebraically smallest principal stress.

For uniaxial tension, the shear yield stress is equal to $\frac{\sigma_y}{2}$. Therefore, the Tresca criterion can be given by:

$$\sigma_1 - \sigma_3 = \sigma_y \qquad (2.32)$$

As shown in Figure 2.6, the Tresca's yield surface is circumscribed by von Mises' criterion. Therefore, it predicts plastic yielding for stress states that are still elastic, according to the von Mises criterion. As a model for plastic material behaviour, the Tresca criterion is therefore more conservative. Moreover, the Tresca criterion does not take into account the intermediate principal stress. It is necessary to know in advance which are the maximum and minimum principal stresses.

2.2 Dislocation

The dislocation theory plays an important role in the analysis of plastic deformation. Before introducing the subject of plasticity mechanisms, it is necessary to gain some qualitative understanding about dislocation.

2.2.1 Crystalline structure of metals

The atoms in metallic solids are spatially arranged in a regularly repeated order of a three-dimensional pattern. In a crystalline structure, the atoms can be represented by points in space. The pattern around which the points are arranged is called a lattice. The periodic pattern of a crystal lattice can be described by its smallest crystal unit which is known as a unit cell. The unit cells stacked in three-dimensional space show the atomic arrangement of metals.
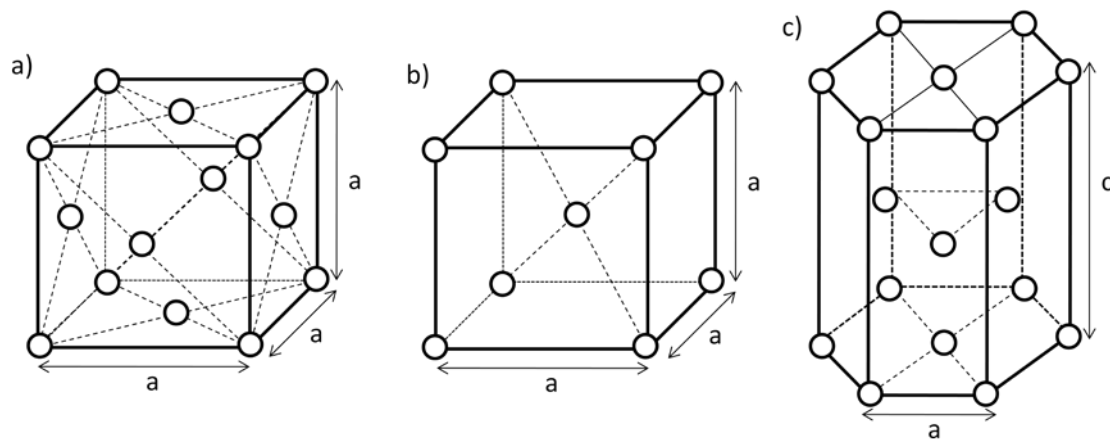
Figure 2.7: Unit cells of: a) FCC; b) BCC; c) HCP lattices [34]

There are three common lattice types: face-centered-cubic (FCC); body-centered-cubic (BCC); and hexagonal closed-packed (HCP) lattices [34]. Many of the common metals have either a BCC or an FCC crystal structure. The unit cell of the FCC lattice depicted in Figure 2.7(a) has one atom at each corner and one atom at the centre of each cubic face. The lengths of the edges of the unit cell are equal and are denoted by a. Since each corner atom is shared by eight adjacent unit cells and each surface atom belongs to two unit cells, there are four atoms per unit cell for the FCC lattice. Many metals crystallize in an FCC lattice structure, such as aluminum, copper, gold, silver, lead and nickel. In Figure 2.7(b), a BCC lattice with one atom at each corner and another atom at the body centre is shown. Therefore, there are two atoms per unit cell. The edge lengths are again equal. Typical metals which have a BCC lattice structure include iron, columbium,

tantalum, chromium, molybdenum, niobium and tungsten. The unit cell of an HCP lattice is shown in Figure 2.7(c). The upper and lower planes are regular hexagons with an edge length a, while the distance between both planes is given by c. Zinc, cadmium, titanium and magnesium are the common HCP metals. The FCC and HCP lattice structures are both close-packed structures.

2.2.2 Dislocations in crystals

Defects are imperfections which deviate from an orderly arranged lattice structure. If defects occur only at or around a single lattice point, they are known as point defects. The three main types of point defects are: vacancy; interstitial; and impurity atoms. If point defects propagate as lines in the crystal, they become line defects. Dislocations are typical line defects which can be divided into two basic types: edge; and screw dislocations [35]. If line defects cluster into a plane, then they become plane defects. Grain boundaries are surface defects.

The presence of dislocations strongly influences the mechanical properties of materials. As has been discussed in section 2.1.3, metals can deform plastically due to dislocation glide. As the dislocation moves, slip occurs in the area over which it moves. If there is no obstacle to prevent it, a dislocation can move easily under an applied small force. In general, dislocations are intimately connected to nearly all other mechanical phenomena such as strain, hardening, yielding, creep, fatigue, and brittle fracture.

Dislocations that exist in real materials are typically mixed, which means they are characterised by both edge and screw dislocations. The edge dislocation was first highlighted by Orowan, Polanyi, and Taylor [31]. A schematic drawing is shown in Figure 2.8(a), illustrating a typical edge dislocation AB, which is located as the boundary between the slipped part on the right and the part on the left that has not yet slipped. Dislocation glide occurs in the direction of the slip vector and proceeds towards the left unslipped region. Additionally, a Burgers vector b is introduced to describe the magnitude and direction of displacement to the lattice, as shown in Figure 2.8(b). In an edge dislocation, the Burgers vector is always perpendicular to the dislocation line. When the dislocation moves, the atoms along the dislocation line slip over by the distance between adjacent atoms. The shaded area in Figure 2.8(a), which represents the slip plane, gradually extends towards the left side as the dislocation line passes through the whole plane. In addition to dislocation glide/slip, there is another type of dislocation motion called climb, which allows an edge dislocation to move out of its slip plane. The driving force for dislocation climb is the movement of vacancies through a crystal lattice. As illustrated in Figure

2.9, if a vacancy moves next to an edge dislocation, the atom that belongs to the edge dislocation can jump and fill the vacancy. This atom shift is the essential precondition that causes the climb of the dislocation. Since dislocation climb is diffusion controlled, it occurs much more rapidly at high temperatures than at low temperatures. Diffusion of atoms or vacancies can take place at an appreciable rate at high temperatures. Thus, the climb of an edge dislocation normal to its slip plane is easily possible at elevated temperatures by means of atom self-diffusion, during which the atoms along the dislocation line transfer to other lattice vacancies. On the other hand, dislocation glide is much slower and less likely to occur at low temperatures. In perfect single crystalline materials, dislocation motion terminates when dislocations reach a free surface. In polycrystals, it stops when dislocations arrive at grain boundaries.
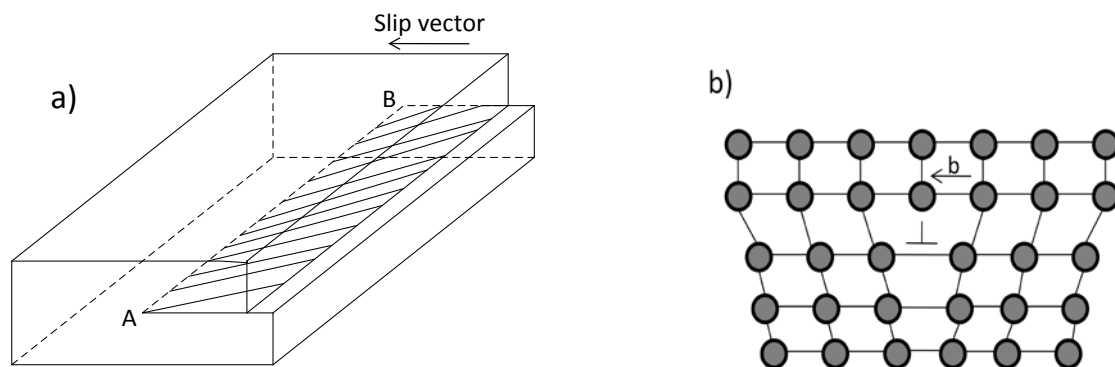
Figure 2.8: a) edge dislocation with the dislocation line AB and slip plane on the shaded area; b) distorted lattice plane normal to an edge dislocation [31]. Grey circles represent atoms.
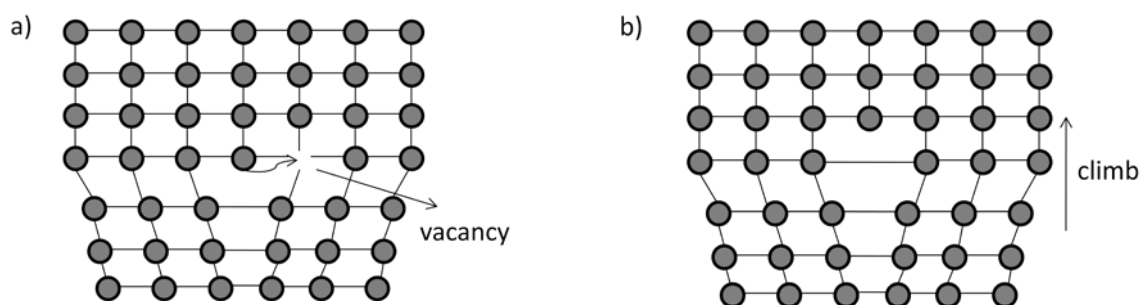
Figure 2.9: Climb of an edge dislocation [31]: a) diffusion of vacancy and atom; b) dislocation line moves upwards.

The second basic type of dislocation is the screw dislocation. Figure 2.10 shows a schematic drawing of a screw dislocation. The upper part of the crystal has moved towards the left side relative to the lower part. The dislocation line *CD* is parallel to the Burgers vector *b*. Unlike edge dislocation, screw dislocation has no particular slip plane. Therefore, the motion of a screw

dislocation is less restricted. The screw dislocation is able to glide on different planes that contain the dislocation line, which results in a cross slip. A standoff dislocation climb is not possible with a screw dislocation.
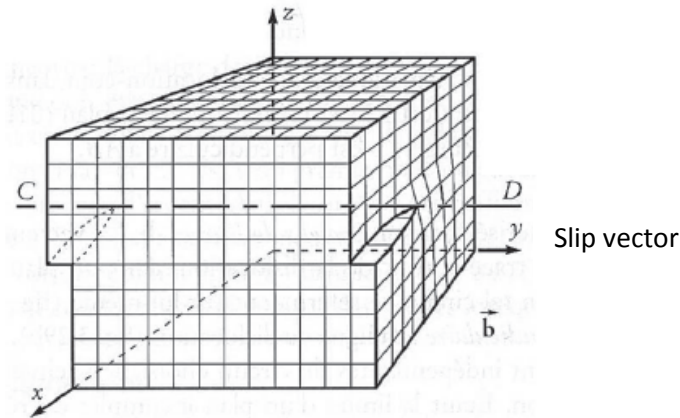
Figure 2.10: Screw dislocation lies along the line CD, parallel to the slip direction y [31].

As mentioned previously, in reality, for imperfect crystals dislocations exist not only in straight configurations, such as edge or screw dislocations, but also in the form of dislocation loops which are mixtures consisting of both edge and screw characters [26]. As shown in Figure 2.11, the dislocation line is a closed loop which represents the boundary between the slipped and unslipped region on the slip plane. Each point on the dislocation line can be decomposed into edge and screw components by resolving the Burgers vector b into two mutually orthogonal components represented by the equation:

$$\vec{b} = \vec{b}_1 + \vec{b}_2 \tag{2.33}$$

where $|b_1| = |b| \sin\theta$ and $|b_1| = |b| \cos\theta$. $\vec{b}_1$ and $\vec{b}_2$ are perpendicular and parallel to the tangential line of the point on the dislocation loop. The angle between the dislocation line and its Burgers vector is denoted by θ.

Dislocations can move in crystals under stress. One of the most prevalent movements of dislocations is glide. Dislocation glide is confined to the slip planes of the crystals and is considered to be the most important mechanism responsible for plastic deformation. Additionally, dislocation climb also plays a role at elevated temperatures. Since the Burgers vector for edge dislocations is perpendicular to the dislocation line, the slip plane can be uniquely defined. There is only one slip plane whose normal direction is conformal to the direction of the Burgers vector. The glide of edge dislocation can occur on this slip plane. For screw dislocation, the glide is more complex. Since its Burgers vector is parallel to the

dislocation line, the slip plane can be easily defined. The screw dislocation is able to glide on different planes that contain the dislocation line, which results in a cross-slip.
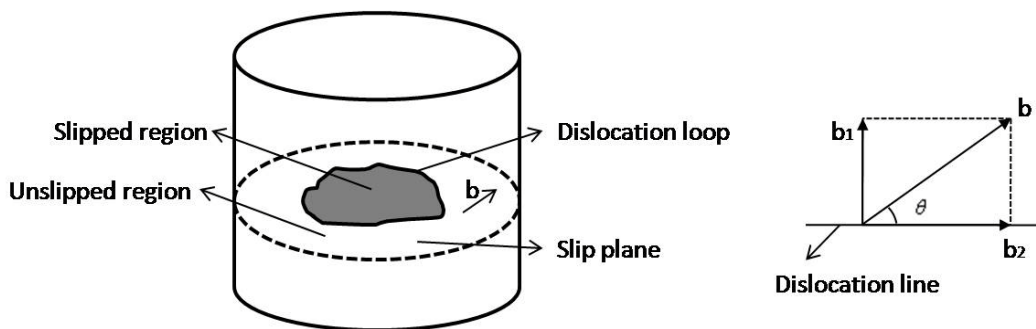
Figure 2.11: Decomposition of a dislocation loop [26].

2.2.3 Stress field and its impact on dislocations

As explained in the previous chapter, a dislocation is a defect in a crystal which causes a disturbance among the regularly arranged atoms. This disordered atomic arrangement leads to elastic distortion around the dislocation line. Thus, the local stress field induced by a dislocation can be described by linear elasticity theory, as described in section 2.1.2. Associated with the stress field around a dislocation, there is also elastic energy stored in the region. Understandably, when dislocations are located very close together, they will interact with each other which results in a reduction in the total stored strain energy.

One of the most important concepts in dislocation theory, which is related to the local stress field, is dislocation pile-up [36]. In polycrystalline materials such as copper, grain boundaries act as the main obstacles to dislocation glide. If dislocations generated from a source reach a grain boundary, they will pile up against this obstacle, as illustrated in Figure 2.12. The dislocations near the grain boundary will be more closely packed, while those further from the grain boundary will be more widely spaced. The total number of dislocations which can be constrained by a grain boundary depends on the type of grain boundary (high angle or low angle), the angle between the slip plane and the grain boundary, the material and the temperature. The breakthrough of dislocation to a grain boundary can occur by slippage on a new plane, by dislocation climb around the grain boundary, or by the generation of sufficiently high tensile stresses to produce a crack.
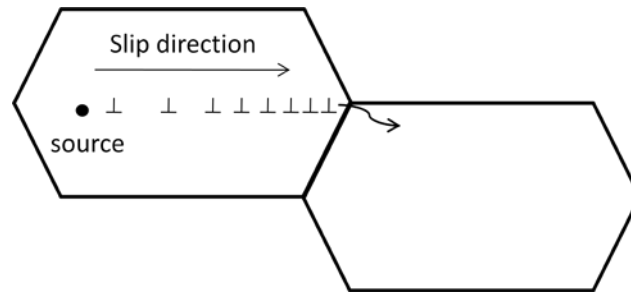
Figure 2.12: Dislocation pile-ups against a grain boundary and breakthrough to the adjacent grain [36]. The hexagons represent the grains.

The dislocation pile-up produces a back stress which acts to oppose the motion of additional dislocations along the slip plane in the slip direction. In a state of equilibrium, the dislocations hindered by the grain boundary exert a force on the grain boundary while the grain boundary exerts a force of the same magnitude back onto the dislocations. Consequently, an internal stress field is generated by the force coming back from the grain boundary, which causes hardening effects in materials. For instance, strain hardening can be attributed to the dislocation pile up. All the hardening mechanisms which are relevant to plastic deformation in metals will be discussed in more detail in section 2.3. In addition, the stress field built up by dislocation pile-up can also initiate plastic deformation in the neighbouring grain by activating dislocation glide, which is generally ruled out as a Hall-Petch relation [37, 38].

Dislocation pile-up which affects the strength of the material is a very important concept for understanding the Hall-Petch law [37, 38] which will be discussed in more detail in section 3.3.2. A material with a larger grain size is able to contain more dislocation pile-up, which generates a larger back stress field on the dislocation. As a result, less force is needed in order to move a dislocation. In other words, materials with a larger grain size exhibit lower yield stress.

So far we have discussed the internal local stress field in relation to dislocation and dislocation motion in microscopic scope [31]. However, external global stress also plays an important role in the effect of dislocation motion, which must be taken into account. When a sufficiently high stress, which is beyond yield stress, is applied to a crystalline material, the dislocations inside can move, leading to plastic deformation. The effect of applying a stress is equal to applying a force onto the dislocation line. To consider a rectangular slip plane with a width l_1 and length l_2, the total force on the plane can be calculated as:

$$T = \tau l_1 l_2 \tag{2.34}$$

where τ is the shear stress acting on the plane. If a dislocation line with a length of l_1 and Burgers vector b then moves all the way along from one end of the slip plane to the other, the total

movement is l_2. The displacement of the atoms is equivalent to b. Thus, the work done by the shear stress during this process can be expressed as:

$$W_1 = \tau l_1 l_2 b \tag{2.35}$$

On the other hand, an external force F can also contribute to the movement of the dislocation. Therefore, the work done by the force can be calculated as:

$$W_2 = F l_2 \tag{2.36}$$

As both correspond to the same dislocation movement, the above two equations should be equal. Consequently, we can obtain the force required to cause dislocation glide as follows:

$$F = \frac{\tau b}{l_1} \tag{2.37}$$

In conclusion, the shear stress, Burgers vector and the length of a dislocation determine the minimum external force needed in order to activate dislocation glide.

2.3 Plasticity

The irreversible deformation in shape of a material without any increase in loads or stresses can be described as plasticity. As discussed in section 2.1.2, Hooke's law can be used to formulate elastic deformation. For plastic deformation, the mathematical description is much more complicated. This section will be devoted to discussing plasticity models and strengthening mechanisms.

2.3.1 Plasticity models

For many years, researchers have created different sorts of numerical or analytical models to describe the plasticity of metals. Those plasticity models can be practically used for the prediction of mechanical behaviours of metals under plastic deformation. Usually, plasticity models refer to the mathematical relationships between stress and strain, or between stress and temperature for plastically deformed materials.

Numerical plasticity models which are composed of constitutive equations can calculate stress (force) and strain (displacement) which are widely used in finite element method (FEM)

simulation. The first attempt to formulate the stress-strain relationship for plastic deformation was made by Saint-Venant (1870). Since then, many researchers have continued to develop plasticity models. The most predominant plasticity models are known as isotropic work hardening (Drucker, 1951) and kinematic hardening (Prager, 1955), which describe the changing of the yield surface with progressive yielding, so that the conditions, such as stress states, for subsequent yielding can be established [31]. In isotropic work hardening, the yield surface remains centred at its initial centre point and expands in size as the plastic strains develop. By contrast, kinematic hardening assumes that the yield surface remains constant in size and the surface translates into stress space with progressive yielding.

The classical isotropic hardening and kinematic hardening models can be used to satisfactorily interpret the plasticity properties of metals in the case of proportional loading where the load is increasing monotonically and no unloading occurs. However, when metals undergo a cyclic loading, their mechanical responses are much more complicated. Within the last half-century some models have been proposed to meet this challenge. Various models have been used to represent the different characteristics of plastic deformation [31]. The multisurface model was developed by Mroz [39], the two-surface model by Dafalias and Popov [40-42], the nonlinear kinematic hardening model was initiated by Armstrong and Frederick [43, 44], and further developed by Chaboche [45], while endochronic theory was proposed by Valanis [46] and later further developed by Watanabe and Atluri [47, 48]. The aforementioned models all have advantages as well as disadvantages in the ways that they reflect plasticity theory.

Nevertheless, plasticity models which represent the relationship between stress and strain are not the focus of this study. Instead, models that can illuminate the relationship between stress and temperature are more relevant [49]. Flinn [50] first proposed a model designed to describe stress-temperature curves of aluminum films with the thermally activated dislocation glide as the dominant deformation mechanism. Thouless [51] created a model for passivated noble metal films with the same mechanism. Thermally activated dislocation glide in the presence of rectangular obstacles was expressed by Frost and Ashby [52, 53] as:

$$\dot{\varepsilon} = \dot{\varepsilon}_0 \, exp\left[-\frac{E_a}{kT}\left(1 - \frac{s\sigma}{\hat{\tau}} \right) \right] \tag{2.38}$$

where $\dot{\varepsilon}_0$ is a strain constant dependent on dislocation density, E_a is the activation energy, k is Bolzmann's constant, $\hat{\tau}$ is a critical stress and s is the Schmid factor. The activation energy is a measure of how much energy a dislocation needs in order to overcome an obstacle.

For a thin film/substrate system which undergoes a thermal cycle, thermal strain must be included in the model in order to predict the stress evolution during the thermal cycle. Thermal strain results from the mismatch in the coefficients of thermal expansion (CTE), between the film and substrate material, which can be mathematically derived by:

$$\varepsilon_{thermal} = \int_{T_1}^{T_2} \left[\alpha_f(T) - \alpha_s(T) \right] dT \qquad (2.39)$$

where α_f and α_s are the CTEs of the film and substrate, respectively. T_1 is the temperature at the stress free state, which is usually the deposition temperature.

For films with a stabilized microstructure, thermal strain must be accommodated by elastic and plastic strain. In other words, the total strain of the system must be zero all the time during thermal cycles.

$$\varepsilon_{thermal} = -\left(\varepsilon_{elastic} + \varepsilon_{plastic} \right) \qquad (2.40)$$

As discussed in section 2.1.2, in a thin film/substrate system, film stress σ and elastic film strain are related by the biaxial film modulus M_f ($M_f = \dfrac{E}{1-v}$).

$$\sigma = M_f \varepsilon_{elastic} \qquad (2.41)$$

Due to the fact that a thin film is constrained in the direction parallel to the film plane, it is only necessary to focus on the biaxial stress in plane stress if the film is isotropic. A thin film is free to relax in the direction normal to the film plane. Thus, the out-of-plane stress can be neglected.

Finally, a model of stress evolution during the thermal cycle can be derived by taking the derivative of the film strain balance with respect to temperature instead of time in a combination of (2.39)-(2.41) as follows:

$$\frac{d\sigma}{dT} = -M_f \left\{ \Delta\alpha - \frac{1}{\dot{T}} \varepsilon_0 \, exp\left[-\frac{E_a}{kT}\left(1 - \frac{s\sigma}{\hat{\tau}} \right) \right] \right\} \qquad (2.42)$$

The CTE difference between the film and substrate is defined as $\Delta\alpha = \alpha_f - \alpha_s$ and $\dot{T}$ is the temperature ramp rate.

Weiss (2000) used this model to simulate stress evolution during a thermal cycle [49]. The resulting stress-temperature curves calculated conform well to experimental results. Nevertheless, it is worth noting some limitations and assumptions associated with this model.

Firstly, the obstacles which are taken into account in the plasticity model are point defects such as vacancies, interstitials and impurities. The effect of grain boundary restraining dislocation glide, which is predominant in polycrystalline metals, is not reflected in this model. Secondly, intrinsic strain, which can be induced by the development of film microstructure during deposition or annealing, is not included. The model assumes that there is good adhesion between the thin film and substrate.

2.3.2 Strengthening mechanisms of metals

Plastic deformation happens due to the movement and multiplication of a large number of dislocations. In other words, it is dislocation which allows plasticity. In order to strengthen metals, thereby increasing the yield stress, the key concept is to introduce some kind of interfering medium to prohibit the mobility of dislocations. Although the physical mechanisms that influence plastic deformation can vary widely, the primary difference of strengthening mechanisms is the obstacles which are able to oppose dislocation motion. These obstacles are all defects. Nevertheless, they can be point defects (impurity atoms), line defects (dislocations) or plane defects (grain boundaries). Based on the type of defects, there are four main strengthening mechanisms for metals [36, 54].

The most common mechanism is called work hardening, also known as strain hardening. The primary species responsible for work hardening is dislocations. A stress field is generated by the interaction of dislocations against each other. Therefore, the movement and propagation of dislocations can be impeded by repulsive interactions between stress fields. Additionally, dislocation motion can also be opposed by a dislocation jog which is formed when two dislocations cross each other and dislocation line entanglement occurs. The jogs and entanglements then act as pinning points. In work hardening, dislocation density determines the yield stress because dislocation interactions are more likely to occur when more dislocations are involved in metals.

The second strengthening mechanism is solid solution hardening. In this case, solute atoms such as impurities are added to the body material which results in either substitutional or interstitial point defects in metals. The solute atoms cause lattice distortion which generates a stress field and consequently hinders the motion of dislocations. The strengthening effect depends on the concentration and the size of solute atoms.

The next type of strengthening mechanism is precipitation hardening. The second phase can be created by mechanical or thermal treatment in a binary material system. The precipitate particles of the second phase act as pinning points for dislocations in a similar manner to solutes. If the particles are small, dislocations can cut through them, while if the particles are large, dislocations will readily bow and loop to overcome the obstacle. Thus, the strengthening effect depends on the concentration and the size of precipitate particles.

The last but also one of the most important strengthening mechanisms is grain boundary hardening. In polycrystalline metals, grain structure has a tremendous influence on the mechanical properties. Grain boundaries act as an impediment to dislocation motion. Therefore, grain size and grain boundary density play a role in the determination of yield stress in this case. The stress generated from dislocation pile-up has been discussed in Section 2.2.3, which contributes to the activation of dislocation motion from one grain to another. The plastic deformation occurs in dependence of grain size. The number of dislocations which can be involved in one grain is limited by the grain size. Smaller grains can contain fewer dislocations which results in a lower stress field build up at grain boundaries. This means that dislocations need greater external stress in order to overcome the grain boundary and move into the adjacent grain. The grain boundary hardening mechanism can be also described as a Hall-Petch relationship which will be discussed in more physical and mathematical detail in the Section 3.3.2.

3 Mechanical properties of electroplated Cu films

Investigations concerning the mechanical behaviour of thin films were initiated as a result of the technological challenges and there is continuing motivation in this field as microelectronics adopts new material systems and as the dimensions of devices continue to shrink. The unusual material behaviour observed in thin films with very small scales is encouraging further academic interest. This presents a unique opportunity to extend the fundamental understanding of material properties to multiple film thickness scales. Moreover, the intensive research on thin films has been initiated due to its broad usage in various engineering applications.

Thin film behaviour has been intensively studied over the past few decades and the deviations from bulk material properties have been analysed [55]. Compared to their bulk counterparts, thin metal films exhibit remarkably high flow stresses [56, 57]. This chapter presents a summary of a number of attempts that have been made to enrich our knowledge of thin films, especially Cu films. As a review, the typical deposition technique, mechanical measurement test, as well as the main experimental and theoretical advances regarding thermo-mechanical properties of Cu thin films will be addressed.

3.1 Electroplating of Cu films

Since the mechanical properties are sensitively dependent on the thin film fabrication process, it is crucial to have some knowledge of typical film deposition techniques for Cu films. Usually, methods such as drawing, casting, rolling, or moulding are used to manufacture bulk materials. Thin films are produced utilising other techniques. The most common methods for thin film deposition can be divided into physical deposition and chemical deposition. The physical deposition uses mechanical or thermodynamic methods to produce a thin film. Typical physical deposition includes evaporation, sputtering and pulsed laser deposition. The target material is usually placed in an energetic, entropic environment so that particles of the target material can escape from its surface. Meanwhile, the target material faces towards a cooler surface which hosts for the arrival particles, allowing them to form a solid layer. The whole system is facilitated in a vacuum chamber. Since particles tend to travel along a straight path from the target material to the free surface, film deposited by physical methods is commonly directional, which means the texture of the film will be strong. In chemical deposition, a fluid precursor undergoes a chemical reaction at a solid surface, forming a solid layer. It includes electroplating, chemical vapour deposition and chemical solution deposition. As the deposition substrate is usually

surrounded by the reaction fluid, deposition occurs everywhere on the surface. Thus, thin films produced by chemical deposition are commonly not directional but rather conformal and therefore their texture is relatively weak.

Electroplating, which is also called electrochemical deposition, is a process that uses electrical current to reduce the cations of a desired material from a solution and deposit a thin layer onto a conductive surface [58]. During the plating, the surface to be coated is immersed into a solution called an electrolyte, containing one or more dissolved metal salts as well as other ions that permit the flow of electricity. The surface needs to be conductive and acts as the cathode of the electrical circuit. The anode is made of the metal to be plated. A power supply provides either a direct current (DC), an alternating current (AC), or an AC-DC combination, to the anode, oxidising the metal atoms that comprise it and stimulating them to dissolve in the solution. At the cathode, the dissolved metal ions in the electrolyte solution are reduced at the interface between the solution and the cathode, such that they "plate out" onto the cathode. The rate at which the anode is dissolved is equal to the rate at which the cathode is plated. In this manner, the ions in the electrolyte bath are continuously replenished by the anode. Electroplating is a simple and economical way to deposit uniform coatings, and it has been used across a wide range of industries.

Electroplating is now frequently introduced for Cu film deposition in power metallisation plating and dual damascene of advanced integrated circuits. Compared with other deposition methods, electroplating has its particular advantages, for example, low cost, low deposition temperature, and high gap-filling capability. However, there are also some drawbacks involved with electroplating. For instance, it cannot be applied for the deposition of alloys and non-metallic films. Because of the room temperature deposition, the resulting defect density in the film may be very high. Due to the exposure of the film growth to the electrolyte, impurities may be introduced. A seed Cu layer is necessary to be sputtered prior to the plating process because a conductive surface is required as a cathode for the electro-deposition.

3.2 Mechanical measurements for thin films on a substrate

In order to gain a good understanding of the mechanical behaviour of thin films, it is essential to acquire accurate values which describe various mechanical properties. The traditional mechanical testing methods used for bulk materials cannot be applied directly to the study of thin films, because thin films simply have a significantly different dimension scale from bulk materials. Several specialised techniques have been developed over the past few decades to measure the mechanical response of thin films [59, 60]. One of the most widely used and

commercialised techniques to test thin films on substrate is the substrate curvature technique [7, 9, 61-63].

The substrate curvature is induced during film deposition or post-processing due to the atomic mismatch between the film and the substrate. It provides valuable insight into the mechanical properties of thin films and the relevant mechanisms which drive the stress development. The stress in the film is caused by the bending of the film/substrate system and can be related to the substrate curvature through Stoney's equation [64-67]:

$$\sigma = \frac{Eh^2}{(1-v)6t}(\frac{1}{R_2} - \frac{1}{R_1})$$

(3.1)

where σ is the film stress, E corresponds to the elastic modulus of the substrate, v denotes the Poisson's ratio of the substrate, h and t are the thickness of the substrate and film, R_1 and R_2 are the measured radii of curvature before and after the electroplating deposition of Cu films, respectively.

The methods to measure the substrate curvature in a film/substrate system can be classified into several types: the mechanical method, capacitance method, X-ray diffraction method, and the optical method. Except for the X-ray diffraction method, which directly measures the elastic strains, other methods have the common feature that they measure the out-of-plane deflection of the film/substrate system. The mechanical method usually uses a stylus which touches the surface and scans along the radial direction of the film. The capacitance method involves non-contact probes, which record the change in capacitance between the film surface and the probes. Although the mechanical and capacitance methods provide accurate measurements of substrate curvature, they are not suitable to be incorporated into a furnace or deposition chamber for an in-situ stress measurement during a thermal annealing process or deposition process. The x-ray diffraction method estimates substrate curvature by determining the Bragg angle. However, the limitation of the X-ray method is that care must be taken to ensure that the substrate is crystalline in order to create Bragg diffraction. Compared to other methods, optical methods can overcome the drawbacks mentioned above and offer more convenient, accurate and flexible measurement possibilities for probing the curvature of the film/substrate system. Different kinds of techniques can be employed for the optical methods, such as single laser scanning, multiple laser beam optics, grid reflection and a coherent gradient sensor. With the technique of single laser scanning, an incident laser beam scans across the wafer surface. The reflection angle and the relative position of the reflected laser beam back on a position-sensitive detector are used for the calculation of wafer curvature. With multiple laser beam optics, there is no need to scan the laser beams on the wafer surface. Instead, wafer curvature can be captured instantaneously by the illumination of multiple laser beams on a single spot of the wafer surface. The wafer curvature is determined from the relative distance of the adjacent beams. The grid

reflection method can provide a full-field reflection of a grid or grating from the surface of a curved substrate. Based on the distortion of a periodic pattern, which is imaged by a CCD camera, the entire wafer curvature can be obtained. The coherent gradient sensor method is a full-field interferometric technique that produces fringe patterns by laterally shearing an incident wavefront. A great variety of equipment based on the above methods has been developed and continues to evolve, implementing different sample geometries and novel instrumental technologies.

3.3   Plasticity of Cu films

The perfect crystalline copper has a face-centred cubic (FCC) structure in crystallography. Each unit cell contains 4 Cu atoms. The lattice parameter of Cu is equal to 0.361nm and its density 8.92g/cm³ [38]. However, Cu thin films which are deposited for the application of metallisation in semiconductor devices usually contain various kinds of defects, such as vacancies, interstitials, impurities, dislocations and grain boundaries. The presence of defects plays an extremely important role in determining the electrical and mechanical properties of Cu thin films.

For polycrystalline Cu films, material properties can be isotropic or anisotropic which is determined by the directional probability of individual Cu crystallites whether they are oriented through the film equally or not. In this way, the texture of a film can be defined as the preferred crystallographic orientation of individual crystallites. The revealed effective values of macroscopic properties can be calculated by averaging the directional values over all orientations in a film. Therefore, the texture affects material properties. For instance, the correlation of stress and sheet resistivity evolution at room temperature with film texture has been reported. Some reviews also discussed the observed texture of Cu films in relation to film thickness [68-73]. The (111) oriented grains should be more favourable in thinner films, based on surface energy considerations. This is a result of the fact that thinner films have a larger surface-film thickness ratio.

One of the promising techniques that can be used to examine the stress state in microscopic features is the finite element method (FEM). By the implementation of material models containing the elastic modulus, Poisson's ratio and coefficient of thermal expansion in FEM, stress information can be obtained in any geometrical shape. However, one must note that it is not possible to simulate a detailed layer structure of an entire chip which would require unrealistic calculation times. Thus, certain reasonable assumptions that can simplify the target geometry are necessary.

Below yield stress, polycrystalline films deform elastically and elastic stress is linearly related to strain. Based on the elastic modulus and Hooke's law, film stress in elasticity can be easily calculated. In contrast to this, plastic flow is a kinetic process. In general, film stress in plasticity not only depends on strain but also on the strain rate. The kinetics of plasticity processes on the atomic scale determines the strain rate; for example, the coupled dislocation glide and climb, the atomic diffusion, the grain boundary sliding and so on [9, 14, 50, 51, 74-76].

Dislocation motion is believed to be one of the major mechanisms responsible for the plasticity in thin films [77, 78]. Theoretic models based on dislocation motion barriers, such as discrete obstacles or grain boundaries, have been developed.

3.3.1 Plasticity limited by discrete obstacles

Dislocation motion is a kinetic process [79-81]. Therefore the plastic deformation rate $\dot{\varepsilon}$ (strain rate) is related to the density of mobile dislocations ρ_m and the average velocity of dislocation motion $\bar{v}$ as follows,

$$\dot{\varepsilon} = \rho_m b \bar{v} \tag{3.2}$$

where b is the Burgers vector of the dislocation.

The dislocation density depends on stress and temperature evolved in the material system at a steady state. Argon [82] has proposed a simple function which is consistent with both the theory and experiment:

$$\rho_m = \alpha \left(\frac{\sigma_s}{\mu b} \right)^2 \tag{3.3}$$

where α is a constant of order unity which leads to values between 0.05 and 0.1 depending on the crystal structure, σ_s is the shear stress, and μ is the shear modulus.

The velocity of dislocation movement in a polycrystalline film is actually determined by the waiting time of dislocations at obstacles. This means that if dislocations can easily cut or bypass an obstacle in a short time, dislocation motion is fast. The mean velocity of a dislocation motion can be given by:

$$\bar{v} = \beta b v \exp \left(-\frac{\Delta G}{kT} \right) \tag{3.4}$$

where ΔG is the Gibbs energy of activation for overcoming an obstacle, β is a dimensionless constant, and v is a frequency.

The Gibbs energy can be calculated by

$$\Delta G = \Delta F \left(1 - \frac{\sigma_s}{\hat{\tau}} \right)$$

(3.5)

where ΔF is the activation energy required to overcome an obstacle, and $\hat{\tau}$ is the shear stress in the absence of thermal energy (at 0K).

If we combine (4.2)-(4.4), the strain rate equation for discrete-obstacle controlled plasticity can be obtained as follows [51, 61, 83]:

$$\dot{\varepsilon} = \dot{\varepsilon}_0 \, exp \left[-\frac{\Delta F}{kT} \left(1 - \frac{\sigma_s}{\hat{\tau}} \right) \right]$$

(3.6)

where $\dot{\varepsilon}_0 = \alpha\beta v \left(\dfrac{\sigma_s}{\mu} \right)$. If ΔF is large, $\dot{\varepsilon}_0$ can be considered constant.

Dislocations which are either already existent after deposition or are simply generated by polycrystalline plastic deformation certainly strengthen the film. However, due to the mobility of dislocation, they cannot prevalently situate near grain boundaries. Therefore, they are not as effective strengthening agents as grain boundaries.

3.3.2   Plasticity limited by grain boundaries

Grain boundaries also act as obstacles and are particularly effective against dislocation motion [2, 8, 14, 84]. Due to crystallographic factors, a dislocation cannot move from one grain to an adjacent one through a grain boundary. Based on geometrical considerations, grain boundaries are expected to be stronger obstacles than discrete obstacles (line defects or point defects). The intersection of a planar defect (a grain boundary) with a moving dislocation is a line, while the intersection of a dislocation or a point defect with another dislocation is only a point. Thus, grain boundaries provide a larger resistance than discrete obstacles. It should be noted that if the grain size is large, dislocation motion occurs more easily, which results in a lower yield stress.

The Hall-Petch law [26, 85, 86], which predicts that the yield stress of a polycrystal will be proportional to the inverse square root of the grain size, has been substantiated in a number of metallic materials. Yield stress increases with decreasing grain size following the relationship:

$$\sigma_y = \sigma_0 + k_{HP} d^{-\frac{1}{2}}$$

(3.7)

where σ_y is the yield stress, σ_0 is the intrinsic stress induced by the crystal lattice to resist dislocation motion and k_{HP} is the Hall-Petch coefficient representing the resistance of grain boundaries to dislocation penetration. The Hall-Petch coefficient is related to the crystal structure and can be experimentally determined. A higher value of the Hall-Petch coefficient

reflects a greater resistance of grain boundaries. Likewise, a higher magnitude of k_{HP} is correlated with increasing inherent strength.

Although grain boundaries are remarkably effective barriers to dislocation motion, twin boundaries are considerably different from grain boundaries in terms of mechanical properties. Twin boundaries are not completely impenetrable to dislocations. The resistance of twin boundaries to dislocations is therefore much less than that of normal grain boundaries. If a film has a high density of twin boundaries, the overall k_{HP} will be dramatically reduced, which is typically 1/2 to 1/5 of the usual constant k_{HP}.

3.4 Microstructure of Cu films

The microstructure of thin films is sensitively dependent on the deposition processes and fabrication conditions [87-89]. Also, the microstructure of thin films can strongly influence material properties such as strength, toughness, hardness, ductility, and high/low temperature behaviour, which in turn govern the application of these thin films in industrial practice [90-93]. Thus, a thorough characterisation of the thin film microstructure is essential in order to complete the investigation of material properties of thin films. Microstructure is a comprehensive description of the arrangement of crystallites and defects in a thin film. Some of the most important characteristics include the shape, size and orientation of the crystallites and their distributions, the density and distribution of defects such as impurities, vacancies, interstitials, dislocations, and grain boundaries, as well as the surface and interface morphologies.

The microstructural characteristics of metal films can be influenced by many factors such as film deposition methods, film thickness, post-processing such as heat treatment, and the surface properties of the substrate [89, 94-96]. In the early stage of film growth, the first few atomic layers usually nucleate as islands at many sites on the substrate surface (Volmer-Weber growth). The individual crystallites continue to grow until they impinge upon one another. Subsequently, the impinged crystallites coalesce and, furthermore, the grains coarsen during the thickening of the film. A classic structure-zone model for metal films has been developed by Thornton [97]. There are two main parameters which control the process of microstructure evolution, the ratio of growth temperature T to melting temperature T_m of the thin film material and the system energy. In the zone I regime ($T/T_m<0.3$), a fine-grained structure evolves as a result of shadowing effects. In zone II ($0.3< T/T_m<0.5$), the structure is characterised by coarse grains which appear by surface-diffusion controlled growth. Finally, in zone III ($T/T_m>0.5$), lattice and grain boundary diffusion dominates the growth process which produces large grains

with low defect density and grooved grain boundaries. Electroplating is a room-temperature deposition. The melting temperature of Cu metal is about 1356K. Hence, an as-deposited electroplated Cu film is supposed to have a zone I microstructure of $T/T_m \approx 0.23$.

Fine-grained film can undergo further grain coarsening upon post-deposition treatment, for example, room temperature storage or thermal annealing. The driving force of grain growth is the minimisation of total film energy. Various mechanisms of energy release can alter the microstructure in thin films, such as grain boundary energy, surface energy, interface energy, strain energy and stack fault energy. Normal grain growth is the grain growth with monomodal grain size distribution, which happens usually in bulk materials. For bulk materials, grain growth occurs at the expense of fine grains via the motion of grain boundaries, which is mainly driven by the reduction of grain boundary energy. In thin films, due to the high surface/film-thickness ratio, film surface and interfaces also play a crucial role in grain growth. Furthermore, mismatch strain between film and substrate develops during and after film deposition, which leads to higher strain energy in thin films. Thus, grain growth and crystallographic texture development in thin films are driven by the reduction of grain boundary energy, surface and interface energy, and strain energy. Normal grain growth is not expected in thin films. Instead, abnormal grain growth, or so-called secondary grain growth, is predicted. During abnormal grain growth, a few grains grow into a matrix of small stagnant grains. This is often manifested by a bimodal grain size distribution which follows with a monomodal distribution of very large grains towards the end of this process. For films deposited at room temperature, grain growth and texture development are often retarded due to the lack of thermal activation, which results in a meta-stable structure with very fine grains. At elevated temperatures, the additional thermal energy serves to activate a thermal kinetic process that encourages further microstructural evolution. The rate of grain growth and texture development is determined by the annealing temperature.

When grain size is comparable to film thickness, grain boundaries intersect the film surface and form grooves which suppress further grain growth. Thus, grain growth in thin films stagnates if the forces that act on grain boundaries establish equilibrium conditions. Apart from the forces generated by grain boundary energy, surface and interface energy – the grooving force due to the pinning at grain grooves – is also one of the main physical origins restraining the grain boundary motion [98-103]. A grain boundary intersecting the surface is trapped to its surface groove because it would increase grain length upon moving out of the groove. This is only feasible for large grains as they have a small in-plane and out-of-plane curvature. Small grains with a large intersecting angle between grain boundaries and surface can escape from grooves. If the film contains a high density of impurities, precipitates or second-phase particles, the solute atoms exert a drag force to impede grain growth when they segregate at mobile grain

boundaries. When the driving force for grain growth is counterbalanced by restraining forces, the condition required for stable grain structure is fulfilled. It has been reported that various conditions that result in grain stagnation can arise, depending on the magnitude of the force terms discussed above. Usually microstructural evolution of thin films terminates if the median grain size is several times the film thickness. At the end, a columnar grain structure with grain boundaries traversing the whole film thickness is formed.

In electroplating, the microstructure of thin films is also affected by the chemical additions in the plating electrolyte. These organic components are known as carriers, brighteners or levellers. The structure of electroplated Cu films using the commercial deposition process consists of very fine grains and is very unstable. An interesting example of abnormal grain growth in 1μm thick electroplated Cu films has been reported by Harper [104]. Original grains of 0.05–0.1μm in size grew to several micrometres within 9 hours at room temperature. Meanwhile, a reduction of sheet resistivity and compressive stress in the films were observed. The films often have a high incidence of twins. It was suggested that the minimisation of boundary energy coupled with elimination of boundary pinning sites may be the cause of microstructural evolution at room temperature [105-107].

4 Experimental methods and developments

This chapter describes the standard techniques and apparatus employed to characterise and mechanically test thin films. Though various test techniques have been specifically designed for this purpose, the development of a novel apparatus for measuring the film stress in this work has enhanced the accuracy of data acquisition and extended previous measurement capabilities. This chapter also describes the procedure for sample preparation and the methods used to characterise the microstructure of film. Typical experimental procedures and data analyses are demonstrated for Cu thin films.

4.1 Sample preparation

All investigated Cu films were prepared by electroplating deposition on 8-inch (approximately 200mm) blanket wafers. Prior to electroplating, a 100nm thick thermal oxide was deposited as an isolation layer by chemical vapour deposition (CVD) on the wafers. Subsequently, a 50nm thick Ti film was deposited as an adhesion layer and diffusion barrier, followed by a 150nm thick Cu sputter deposited seedlayer. The barrier and seedlayer were deposited in the same sputter tool without breaking the vacuum. The plating process was performed with a commercial fountain plating system. The electrolyte solution was mainly composed of Cu_2SO_4, H_2SO_4, HCl, and two organic additives: an accelerator and a suppressor with levelling components. An AC-DC current combination was applied. The whole electroplating process consecutively undergoes a pre-wet in methane sulphonic acid (MSA), Cu electroplating and a water rinse followed by a spin-dry process. The plating rate was kept constant for all Cu thicknesses in order to avoid the impact of deposition speed on film properties. Finally, a wide-split plan of electroplated Cu thickness was applied from 1.5–20µm.

4.2 Stress measurement

In order to gain a fundamental understanding of the deformation mechanisms in thin films and to develop adequate models to describe them, it is necessary to have an extensive and accurate measurement setup to detect their mechanical and thermo-mechanical response. This part of the chapter will be dedicated mainly to the development of a novel stress measurement apparatus. The accuracy and repeatability of the stress measurement will be examined and evaluated.

4.2.1   Global stress measurement

Due to the elastic mismatch between the film and the substrate, a biaxial stress evolves in the film after deposition, which in turn induces a change in the wafer curvature (wafer bow). Since the substrate is much thicker than the film and deforms elastically, the film stress can be calculated from the substrate curvature using Stoney's equation. The film stress at room temperature was measured as a function of time by an Eichhorn and Hausmann capacitance probe setup [108]. The geometry gauges are based on two heavy plates mounted parallel to each other. Embedded in the plate are a set of capacitive distance sensors. All wafer geometry characteristics are based on distance measurements performed by multiple capacitive sensors. The wafer surface was positioned at the air gap between the two plates. As a result, wafer curvature can be acquired mathematically by the topography of the wafer.

4.2.2   Development of wafer curvature system for local stress measurement

Thermally induced stress in thin films is one of the major critical factors that can lead to cracks, voids, delamination, or other failures in semiconductor devices [65, 66, 109]. The stress evolution during temperature cycling characterises film properties, such as elastic modulus, coefficient of thermal expansion (CTE) and temperature-dependent yield stress. Moreover, plastic deformation mechanisms such as dislocation glide/climb and diffusion can be investigated by stress measurement during temperature cycling. Creep behaviour of thin films can also be studied by recording stress relaxation at stabilised temperatures. Therefore, the fundamental understanding of thin films in terms of thermally induced stress and rate-dependent stress changes is of great importance when attempting to enhance the reliability and stability of semiconductor devices.

There is a variety of methods to determine the stress in thin films. X-ray diffraction is one of the most informative ways [65, 110-114], as it permits the local measurement of all the components of stress in the film. However, it is limited to crystalline films due to its diffraction-based technique. With the grid reflection method [115, 116], for example, with a Moiré pattern, stress measurements can be extended to non-crystalline films such as passivation glasses or amorphous oxides. However, this full-field measurement requires a large surface area in order to capture a decent pattern and consequently the local stress in the thin film is difficult to assess. The wafer curvature technique is one of the most common methods. However, traditional single laser beam scanning cannot detect the wafer curvature directly. Instead, it measures the tilt and calculates the differential bow height from point to point. For small deformations, the bow height is related to the curvature through the follow equation:

$$\frac{1}{R} \approx \frac{2B}{x^2}$$
(4.1)

where R is the radii of curvature, B is the measured bow height, and x is the scan step size. The measurement accuracy is highly dependent on the scan length and the number of measurement points. Usually, only the global average stress in the film can be assessed. Furthermore, this technique is also dependent on and thus limited by the time span of the laser scanning. In the case of a fast temperature ramping rate, for example, $\geq 0.5°C/s$, the scanning is much too time consuming to acquire enough data and therefore the accuracy is questionable. By measuring the curvature change of a wafer substrate before and after film deposition, the stress involved in the film can be calculated by using Stoney's equation, if the film is much thinner than the substrate.

The apparatus developed for this work can directly provide curvature data without the need to measure bow height. For stress measurements during rapid thermal processing (RTP) curvature data can be acquired within 30ms or even less. Thus, the study of the time-dependent material properties of metallic thin films in the plastic deformation regime shall particularly benefit from this apparatus. Additionally, the scanning mode of the multiple laser beams allows a global study of the wafer curvature along the diameter of the wafer at each stabilised temperature. Eventually, the wafer bow data can be obtained from the extrapolation of the curvature data. The RTP chamber is capable of creating a thermal environment from -65°C up to 650°C, which extends the temperature range of most of the other tests [117-119] which are limited to a temperature range between room temperature and 500°C. As a result, the mechanical behaviour of thin films can be studied at high temperatures and, also, under cryo-conditions. Furthermore, an in-situ formic acid treatment is also available for surface cleaning, which prevents the impact of unwanted oxidations and contaminations on the investigated thin films.

4.2.2.1 Apparatus construction

The schematic diagram of the apparatus is shown in Figure 4.1. The apparatus is comprised of two main parts: a laser optics unit and an RTP chamber. The laser unit generates a multiple laser beam array which can either be scanned along the diameter of a wafer or used in a single position mode measuring a 1x1cm² area at the centre of the wafer. The RTP chamber provides a thermal environment which is necessary for the investigation of thermal stress in thin films. The whole apparatus is fully controlled by the operational computer and software in the RTP heating module.
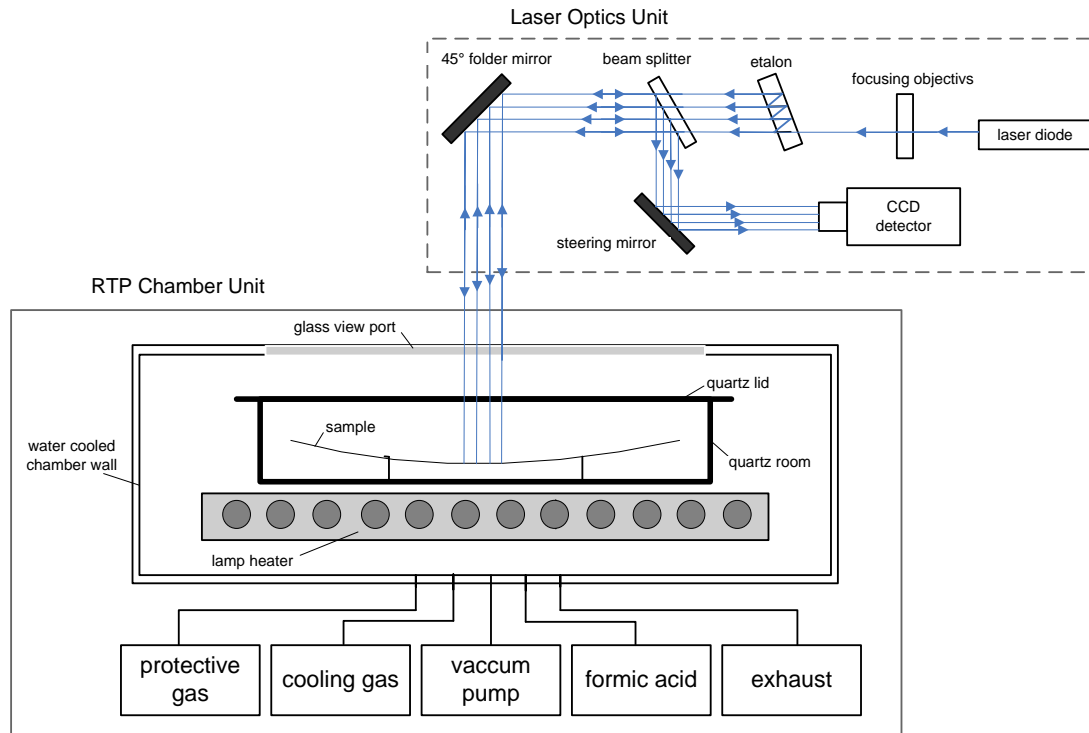
Figure 4.1: Scheme of the apparatus for film stress measurements with multiple laser beams integrated with an RTP chamber. The paths of the multiple laser beams for the wafer curvature detection are indicated.

A. Multiple laser optics

The laser beam array is created using a fibre-coupled laser diode (approximately 25mW output, 660nm wavelength) and a pair of etalon optics. The first etalon generates a linear array in the horizontal direction and the second etalon produces a two-dimensional array from the linear array. A beam splitter and a 45° folder mirror send the array of parallel laser beams through a view port into the RTP chamber at normal incidence. The beams reflect off the wafer and back to the folder mirror, the beam splitter and a servo-controlled steering mirror. The servo mirror keeps the array centred onto a CCD camera. The wafer curvature is detected by the position of the multiple laser spots on the CCD detector. Since the data acquisition rate is rapid (approximately 0.07 second per data point), multiple measurements can be acquired so that the signal can be averaged to improve the accuracy. In general, by averaging N points the noise is reduced by a factor of $\sqrt{N}$. So, averaging 25 points, for instance, reduces the error on the average value of the beam spacing by a factor of 5. The laser beam array provides two advantages:

(i)   Wafer curvature can be measured instantly at any position of the wafer diameter, which guarantees the data accuracy for high ramp rates, for example, 60°C/min;

(ii)   Vibrational noise can be effectively reduced by the subtraction of individual spot positions in the multi-beam array [120, 121].

B. RTP heating module

The RTP chamber equipped with multi-laser optics, as mentioned above, hosts the measurement of wafer curvature. It has a front-mounted slide door sealed by an O-ring. A 10mm x 200mm slit flange viewport is provided on the top of the chamber to facilitate laser scanning and irradiation. The RTP chamber is an integrated system with a water-cooled aluminium main chamber, vacuum-compatible quartz-lined sample compartment and a 3-point 200mm quartz sample mount with an integrated thermocouple (type K) in contact with the sample surface. To maintain the chamber wall at relatively low temperatures, the chamber is surrounded by a highly polished and highly reflective water-cooled aluminium jacket. A diaphragm pump is used to provide a base pressure of approximately 10mbar for the chamber. Heating is performed with a sealed 12x12 crossed quartz lamp array, which can heat non-transparent samples up to 650°C in a vacuum or gas environment of N_2 or forming gas (5% or 10% H_2 in N_2). The RTP chamber is also equipped with a liquid nitrogen heat exchanger, providing cold N_2 gas for active cooling. Consequently, it is capable of cooling from high temperatures down to -65°C with a relatively high cooling rate (approximately 30°C/min). Moreover, the system is equipped with a formic acid module which provides effective surface cleaning for wafer samples prior to the measurements being taken.

4.2.2.2 Apparatus performance

It is vital to evaluate the performance of the apparatus in order to verify the accuracy of the acquisition of the local stress. There are three main issues to consider with respect to the performance, the resolution and the repeatability of the laser measurement and the temperature uniformity provided by the chamber, which will be discussed in detail in this chapter. Additionally the principal of measuring the curvature and the temperature of a wafer will be presented as well, as they are the basics and associated with the performance of the apparatus.

A. The principle of obtaining the wafer curvature

Stress in a thin film is related to the curvature of the substrate according to Stoney's equation. Thus, the key for accurate stress measurement relies on the precise measurement of the curvature. During measurements, the sample is illuminated by an array of parallel laser beams. The spacing of the reflected beams from the sample surface is determined by a CCD camera. The equation of curvature in relation to the spacing of the beams can be derived as follows. Assume a wafer with convex curvature with bending that occurs around the centre "o", symmetric with two parallel incident beams as shown in Figure 4.2 [122]. The true beam spacing is given by d_i, α

is the angle of incidence, R is the radius of the sample and φ is the angle of the normal to the surface at the reflection point of the laser beams.

The distance between point "A" and "B" in Figure 4.2 is given by

$$AB = \frac{d_i}{\cos\alpha} \tag{4.2}$$

and the angle φ is given by the following relation:

$$\sin\varphi = \frac{AB}{2R} = \frac{d_i}{2R\cos\alpha} \tag{4.3}$$

Note that simple reflection requires that the angle between the two reflected beams is 4φ.
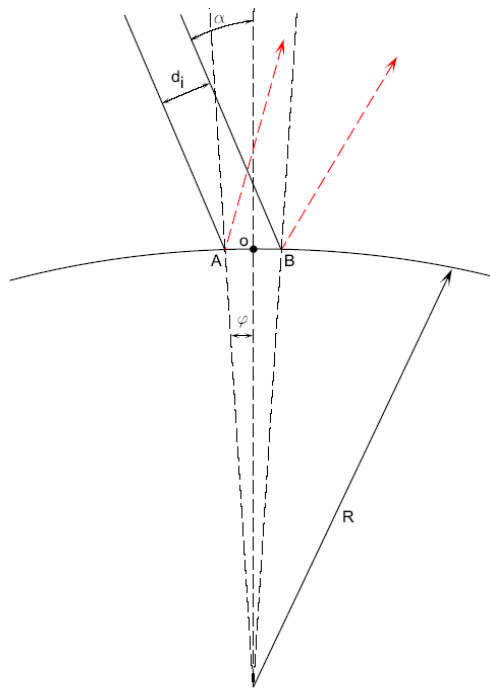
Figure 4.2: Two parallel laser beams strike on and reflect off a curved surface [122].

For complete generality, it is assumed that the substrate has an initial radius of curvature R_i. This is the case in which the initial curvature of the wafer is used as a reference for all the subsequent curvature measurements. This initial curvature will cause the parallel laser beams to deflect with an angular deviation $4\varphi_i$ and the resulting change in beam spacing at the detector will be given by

$$\Delta d_i = L\,tan(4\varphi_i) = L\,tan\left(4\,sin^{-1}\left(\frac{d_i}{2R_i\,\cos\alpha}\right)\right) \tag{4.4}$$

where L is the distance from the sample to the detector. As shown in Figure 4.3, the reference spacing D_0 is now $d_i + \Delta d_i$. Any subsequent changes in curvature will be in addition to the initial substrate curvature and the total change in beam separation at the detector will be given by

$$\Delta d_i + \Delta d_f = L\,tan\left(4\varphi_f\right) = L\,tan\left(4\,sin^{-1}\left(\frac{d_i}{2R_f\,cos\,\alpha}\right)\right) \tag{4.5}$$

Δd_f can be found by subtracting equation (4.5) from (4.4). For approximation we can evaluate the product $\dfrac{d_i}{2R\,cos\,\alpha}$ for the case of a maximum beam spacing of 8mm and a small radius of curvature, such as 4m. In this case, $\dfrac{d_i}{2R\,cos\,\alpha}$ is about 0.001. Even for α about 60 degrees, the approximation still holds for $sin\,x \approx x$ and $tan\,4x \approx 4x$ with the deviation of 2ppm and 5ppm. Therefore we can write from (4.5)

$$\Delta d_f = \frac{2Ld_i}{cos\,\alpha}\left(\frac{1}{R_f} - \frac{1}{R_i}\right) \tag{4.6}$$

Finally the equation (4.7) is derived which relates the change in laser-spot spacing with the change in curvature of the sample.

$$\frac{\Delta d_f}{d_i} = \frac{2L}{cos\,\alpha}\left(\frac{1}{R_f} - \frac{1}{R_i}\right) \tag{4.7}$$
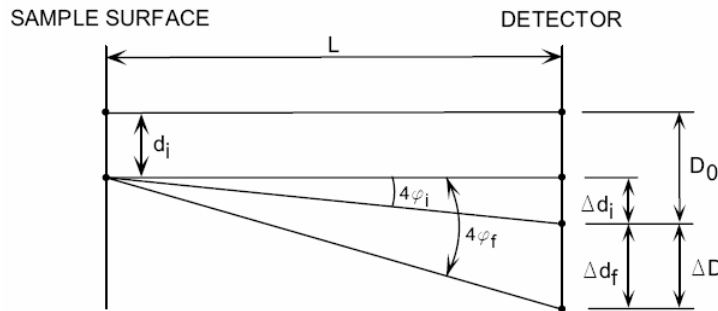
Figure 4.3: Reflected laser beams from sample surface are detected by a CCD camera [122].

B. Measurement and resolution of beam spacing

The CCD detector used in the optics head is an 8-bit analog detector manufactured by Hitachi, model KP-M1AN. The detector uses a 2/3-inch format CCD with 768x474 active pixels with a pixel pitch of 11.64(H) x 13.5(V) μm. The output of the camera is the standard EIA video format with 30 frames per second. The detector has a built-in electronic shutter that has been set to 1/250 sec to minimise the smear of the laser spots from sample vibration. The analog signal is digitised to the resolution of 640x484 pixels using a PCI bus analog frame grabber, model PXR800 from CyberOptics Semiconductor.

The number of spots and the spacing between spots in the laser array can be configured by the rotation of the etalon optics. This system is configured with a 4x3 laser array which works well

with the 4/3 aspect ratio of the 640x484 digitised image. The full width half maximum of a single laser beam within the array is typically around 13 pixels, or approximately 180μm.

The resolution of the system depends on how accurately the position of each laser spot can be determined. To determine the position a centroid calculation is used which is similar to a "centre of mass" calculation but which uses intensity instead of mass. This provides a floating-point position for each laser spot and is reproducible to 0.01 pixel if the system is isolated from vibration and the temperature is stabilised. Of course, in most measurement applications there are instabilities, such as the sample vibration caused by vacuum pumps and gas flow, as well as temperature non-uniformities that all affect the beam positions and thus reduce the reproducibility of the individual beam centroids. The advantage of the multiple beam array technique is that it does not depend on the absolute position of a single beam. In optical techniques that use a single beam rastered across the surface, the measured position of the beam changes due to vibration of the sample and this noise can significantly decrease the resolution of the curvature measurement. By using multiple parallel beam illumination, all the beams strike the surface at the same time. The differential beam spacing (that is, the difference in the positions of adjacent beams that is used to calculate the curvature) is much less sensitive to the sample vibration than the absolute position of the beam. For example, the data in Figure 4.4 shows a case in which two individual beams oscillate in position due to a vibration of the sample. The change in position of each individual beam centroid is quite large and oscillates at a constant frequency. The standard deviation of 100 data points of single laser beam is approximately 0.07. When the two individual beam positions are subtracted the oscillation is effectively removed and the variability in the measurement is greatly reduced. The standard deviation of 100 data points of two parallel laser beams is reduced to approximately 0.009, which is almost 8 times better than if could be provided by a single laser beam. The methods used in other instruments, including single beam scanning and Shack-Hartmann sensors [123], rely on measuring single beam positions. Although the Shack-Hartmann technique creates a multiple-spot array by focusing local wavefronts to individual spots, the curvature calculation is based on the change in position of each individual spot. The technique is still very susceptible to vibration.

a)

Spot 1

b)

Spot 2

c)

Spot 2 Position - Spot 1 Position
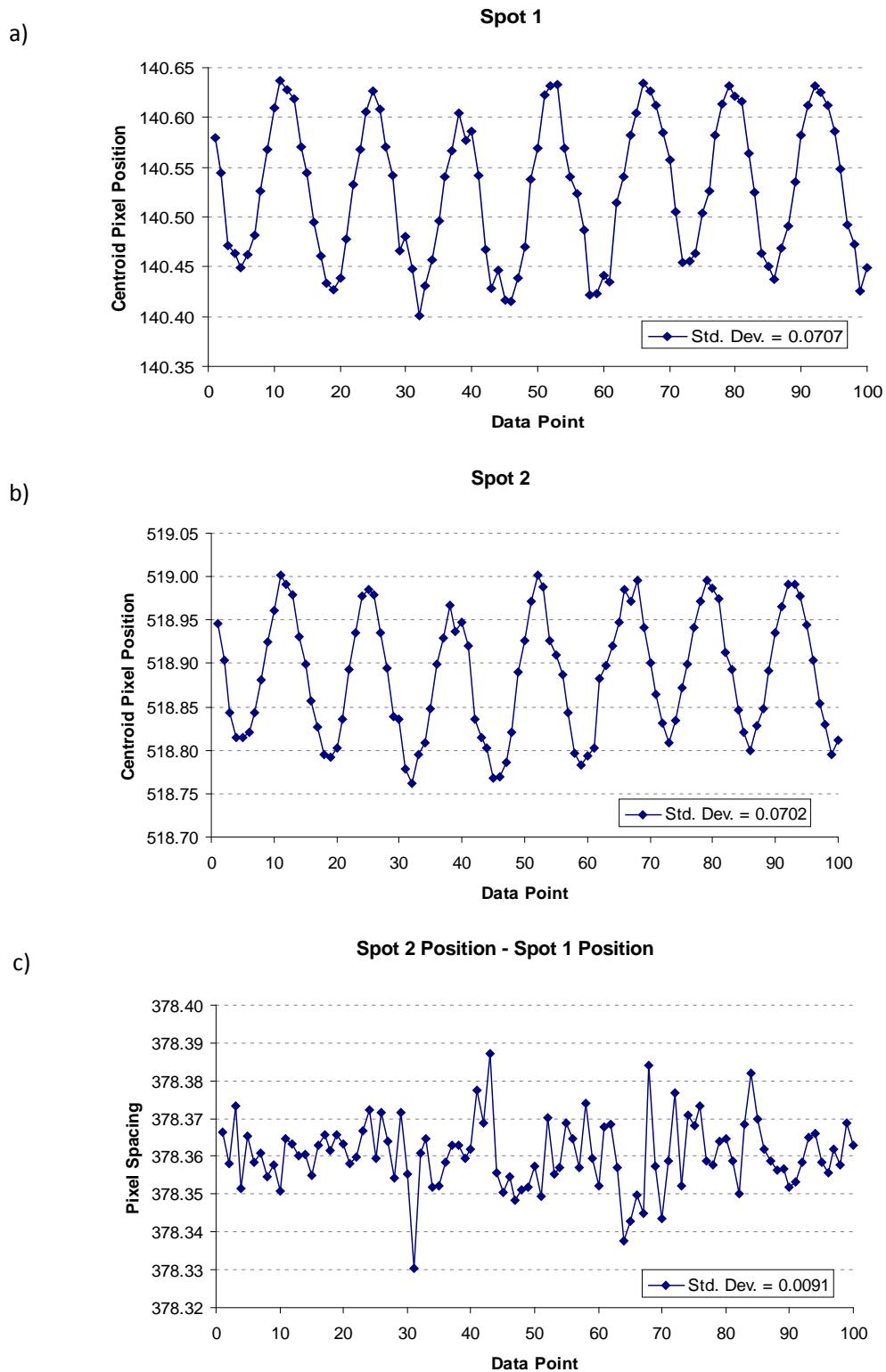
Figure 4.4: The reduction in vibrational noise by detecting the spacing change between parallel laser beams instead of the position change of single laser beam. a, b) The position of two individual single laser beams; c) The spacing between those two individual single laser beam which is the difference of the absolute positions of two single beams.

C. Repeatability of single position and scanning measurements on 200mm wafers

The repeatability of single-point measurements was tested at room temperature with an approximately 723µm thick bare silicon wafer of about 200mm in diameter, polished on both sides. The curvature variation measured at wafer centre over a 60-second period is shown in Figure 4.5. The corresponding theoretical stress changes for a 723µm thick Si wafer deposited with a hypothetical film of 20µm thickness is also presented. The plot reveals a background noise of ± 0.25MPa.
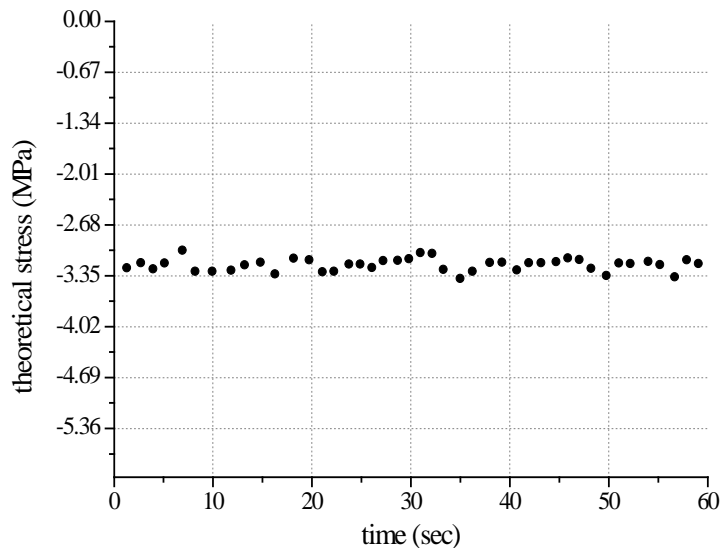
Figure 4.5: Repeatability of the irradiation of multiple laser beams at room temperature, tested with an 8-inch blank Si wafer (approximately 723µm). The theoretical stress is calculated according to the mentioned silicon wafer deposited with a hypothetical film with 20µm thickness.

The repeatability of the laser array scanning was then tested using a step size of 5mm by repeating the scan 10 times along the wafer diameter. The two-dimensional wafer profile, according to a horizontal reference plane, is displayed in Figure 4.6 to verify the signal repeatability of the scanning mode. The graph indicates that the ten wafer height curves overlap each other and can barely be distinguished. The maximum deviation is in the order of ± 0.10µm.

D. Temperature measurement

The measurement accuracy during a thermal cycle is not only determined by the curvature measurement but also by the accuracy of the temperature measurement with a thermocouple in contact with the wafer surface. The calibration of the temperature measurement was performed in the temperature range between -65°C and 650°C with two wafers instrumented with thermocouples, a blank Si wafer and an equivalent Si wafer deposited with a 20µm Cu film. The

blank Si wafer was approximately 200mm in diameter with a thickness of about 723μm, polished on both sides. Near the centre of the wafers, the system thermocouple (type K) was placed with slight pressure contact to the surface. Another thermocouple was also bonded by a laser-welding technique near the system thermocouple. Due to the better contact between the bonded thermocouple and wafer surface, it is believed that the bonded thermocouple provides a more accurate measure of the sample temperature than the system thermocouple. The wafer is placed on the support pins in the quartz chamber in such a way that both bonded and system thermocouples are on the top side of the wafer, facing away from the heater lamps.
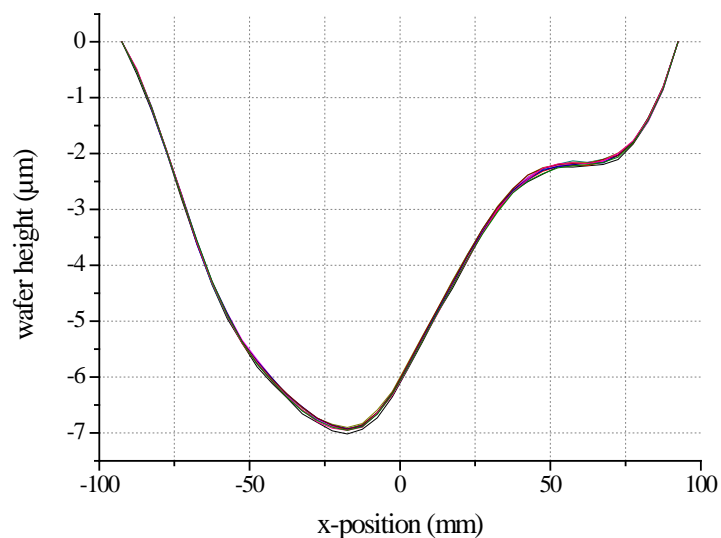
Figure 4.6. Repeatability of the multiple laser beam scanning at room temperature, tested with an 8 inch blank silicon wafer (approximately 723μm) for ten times. The wafer height according to a horizontal reference (y=0) is calculated based on the measured curvature data.

The results of the temperature measurement shown in Figure 4.7 are quite different between the bare Si wafer and Cu film-coated wafer. For the bare silicon wafer (see Figure 4.7a), the measured temperature from the system thermocouple is always higher than the actual wafer temperature which is determined by the bonded thermocouple during the entire cycle. The maximum temperature deviation occurs at about 100°C during heating. Subsequently, the deviation reduces with increasing temperature. During cooling, the temperature deviation stays nearly constant until about 100°C, at which point the temperature deviation becomes smaller due to the significantly slower cooling rate. In comparison, the deviation between measured and actual wafer temperature is considerably reduced for the Cu film coated wafer for the entire cycle (see Figure 4.7b). Only when heated above 250°C, the measured temperature is a bit lower than the actual one.

As the temperature of the silicon wafer increases, the band gap decreases and the wafer increasingly absorbs infrared radiation from the lamp heater [124, 125]. Consequently the thermocouple wires behind the silicon wafer absorb less infrared radiation and more accurately track the true wafer temperature. This leads to the observation that the measured temperature is remarkably higher than the actual wafer temperature for the bare Si wafer at low temperatures and during rapid temperature ramping. On the other hand, if a Cu film is deposited on the Si wafer, the infrared radiation is effectively blocked from the thermocouple wires and most of the infrared is absorbed by the Cu film. Therefore, in practical terms, the temperature deviation can be reduced by the Cu film. This substantiates the finding that temperature calibrations based on a bare Si wafer for thermal stress measurements of metallic films could be
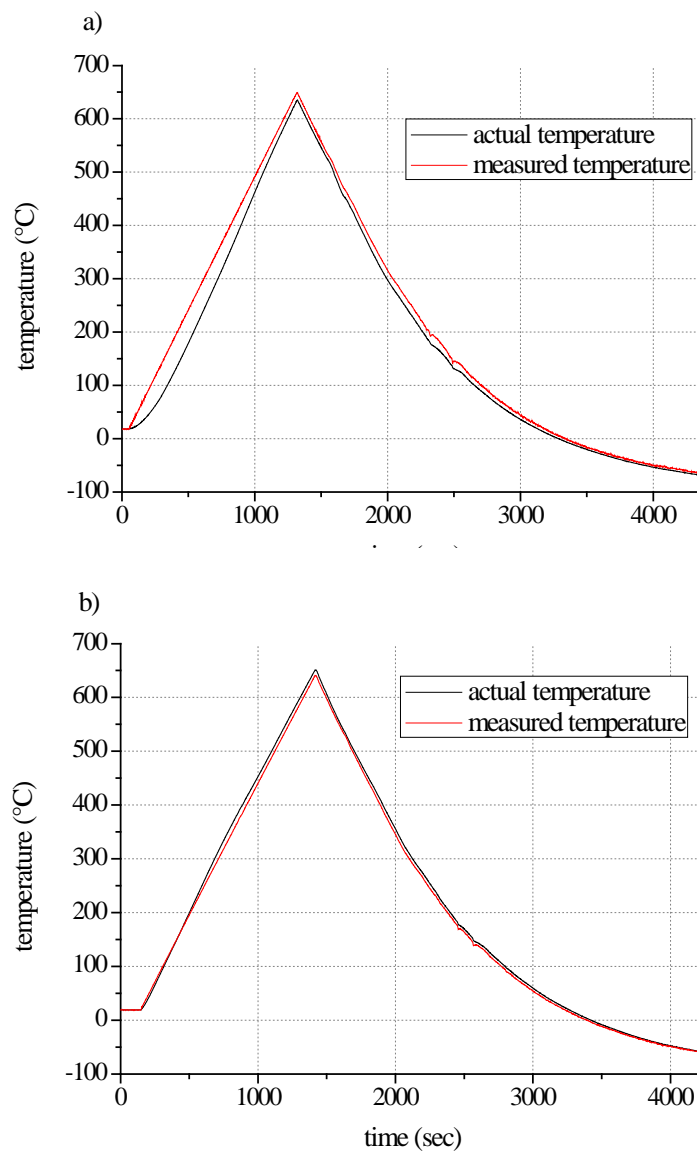
Figure 4.7: The actual temperature in comparison with the measured temperature during a thermal cycle from room temperature up to 650°C with a ramp rate of 30°C/min, then down to -65°C. a) Blank Si wafer; b) Si wafer deposited with a 20µm thick Cu film.

E. Temperature uniformity of RTP chamber

The temperature uniformity on a sample wafer is of great importance, especially when the ramping rate is high, because the temperature non-uniformity will lead to an unwanted thermally-induced wafer curvature. Therefore, the same type of blank Si wafer as mentioned above was equipped with seven temperature sensors (see Figure 4.8a), which are bonded at the centre (position 1), at approximately 75mm away from the centre (position 2, 3) and at approximately 100mm away from the centre (position 4–7) respectively, and these are used to measure the temperatures at different locations on the wafer surface. The sensor bonding method is the same as mentioned before.
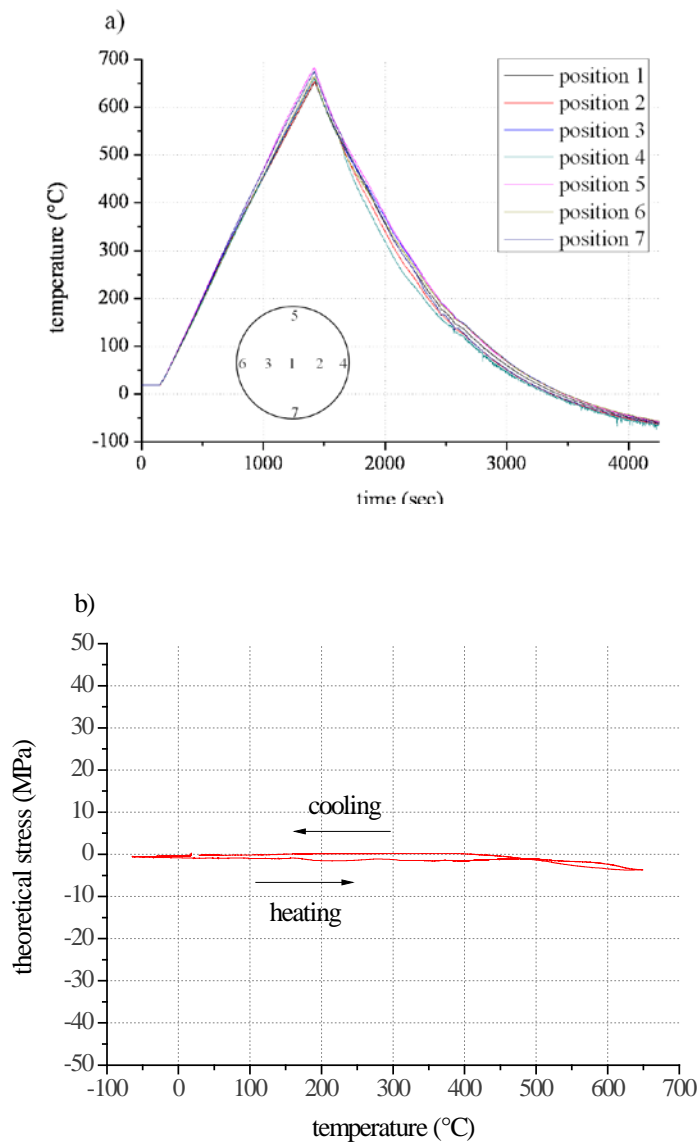
Figure 4.8: Thermal uniformity on a blank Si wafer with a thickness of 723μm during a thermal cycle with a ramp rate of 30°C/min. a) Thermal profiles of seven temperature sensors at different positions of the sample surface. b) Evolution of the theoretical stress during the thermal cycle.

The temperature profiles of each temperature sensor during a thermal cycle (-65°C to 650°C) are plotted in Figure 4.8a, which indicates temperature uniformity is scathed above 500°C during heating and below 500°C during cooling. This observation corresponds well to the calculated theoretical stress based on the wafer curvature recorded during the thermal cycle, which is shown in Figure 4.8b. The theoretical stress refers to the biaxial stress of a hypothetical film with the 20μm thickness deposited on a 723μm thick Si wafer. The relatively good temperature uniformity that occurs until approximately 500°C leads to a plateau of the theoretical stress. Explicitly, no distinct curvature is generated by the thermal non-uniformity at this phase. However, the theoretical stress starts to change above 500°C, which is in agreement with the disparate tendency of the temperature profiles of seven sensors. In order to keep a high cooling rate, the cold N_2 gas purges into the chamber below 500°C with a massive flow. Understandably, the theoretical stress curve during active cooling diverges from the one during heating because of the disturbed temperature uniformity. Below 100°C, the stress curve converges during heating because of the improved temperature uniformity caused by a relatively slower cooling rate.

There are two facts of which one must be aware. First of all, the significant change of theoretical stress above 500°C may not only originate from the reduced temperature uniformity, but also be induced by the thermal gradient from the lamp-heated side of the sample to the unheated side [121]. Unfortunately, due to the fact that the temperature difference between two wafer sides is unknown, it is difficult to estimate the magnitude of the effect from the thermal gradient. Secondly, a Si wafer coated with a Cu film should achieve better thermal uniformity due to higher heat conductivity.

4.2.2.3 Test results on copper samples

Electroplated Cu film becomes easily oxidised in the ambient atmosphere. Depending on the exposure time and temperature, the thickness of the native oxide layer on Cu films can be up to several tenths of a nanometre [126, 127]. The cleaning treatment to remove the native oxide influences the thermo-mechanical behaviour of the Cu film, especially at high temperatures, because the oxide layer may act as a passivation layer for the Cu film. The stress hysteresis of a 20μm thick Cu film with and without formic acid cleaning is shown in Figure 4.9. The measurement noise below approximately 500°C during cooling is induced by the large volume of cold N_2 gas flow. The disparate tendency of two stress hysteresis curves is caused by the removal of native oxide on the Cu film with the application of a formic acid treatment at 200°C for 10 minutes. A significant difference in the film stress evolution is observed between the sample treated with an in-situ formic acid cleaning at 200°C and the one that has no cleaning treatment. Meanwhile, it is observed in Figure 4.10 that more grain grooves, boundaries and

twins can be seen on the surface of the Cu film after formic acid treatment. It is believed that in-situ acid treatment helps to remove the native oxide, thus the diffusion path via grain boundaries to the free surface is not blocked anymore. Therefore, a reduced compressive stress is expected at high temperature ranges as a strong stress relaxation mechanism such as diffusion is effectively activated, as shown in Figure 4.9.
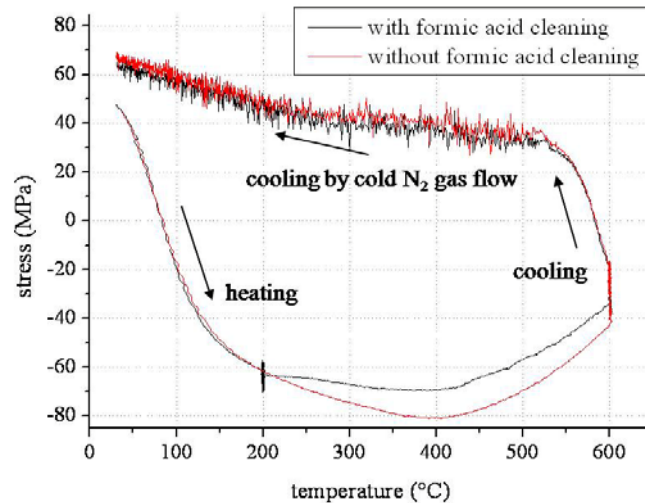
Figure 4.9: Stress hysteresis of 20µm thick Cu film during a thermal cycle between room temperature and 600°C with a ramp rate of 30°C/min.
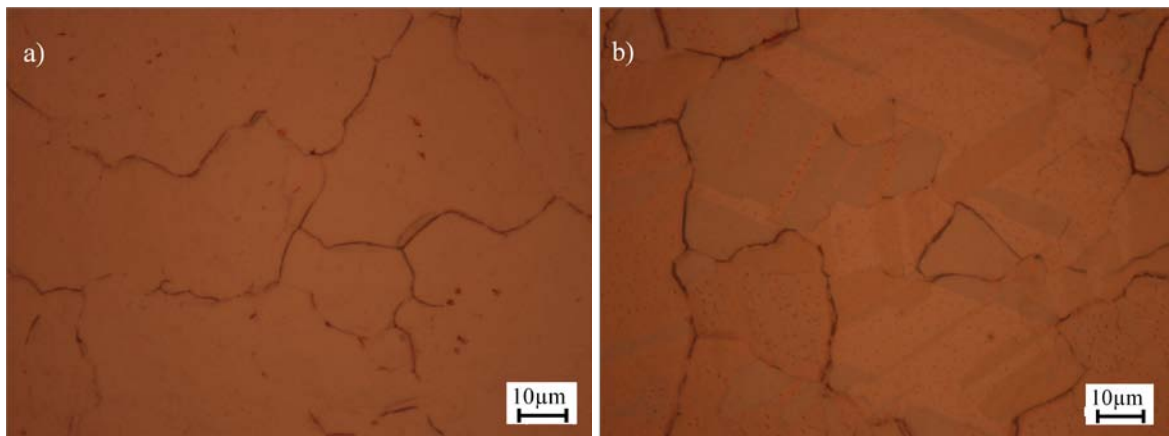
Figure 4.10: Optical microscopic images of the surface of 20µm thick Cu films. a) without formic acid treatment; b) with formic acid treatment at 200°C for 10min.

4.3   Characterisations

The other standard characterisation methods which are used in this work will be reviewed in this part of the chapter, includeing brief descriptions of how to analyse the electrical property, microstructure, grain size, and surface of thin films.

4.3.1   Sheet resistance measurement

Electrical resistance of a film, which normally refers to sheet resistance R_s, was measured with a 4-point probe [128]. The sheet resistance is defined as

$$R_s = \frac{\rho}{t_f} \tag{4.8}$$

where ρ is the specific resistivity of the film and t_f is the thickness of the film. A 4-point probe consists of 4 equidistant metal pins which are placed on the film. Current I flowing through the two outer pins produces a voltage drop V between the two inner pins. If the film diameter is larger compared to the dimension of the 4-point probe, the sheet resistance is obtained as [97]

$$R_s = \frac{\pi}{ln2}\frac{V}{I} \cong 4.53\frac{V}{I} \tag{4.9}$$

A commercial instrument (Omnimap) was used for sheet-resistance measurement. The applied current was 200mA. The samples were 8-inch Cu-plated wafers. The measurements were performed at 49 points evenly distributed over the wafer surface for each sample. At the end, the average value and standard deviation of sheet resistance can be obtained for each sample.

4.3.2   Microscopic techniques

For the characterization of the microstructure and texture of Cu films, two different microscopic techniques were used in this study, which will be presented in this chapter.

A.   Focused ion beam (FIB) microscope

The FIB technique is usually used for such tasks as site-specific cross-sectioning for interfacial microstructure studies, preferential removal of certain metals or oxides, semiconductor device editing or modifications, site-specific TEM sample preparation, and grain imaging.

In this study, a FIB system (Micrion 9500, 30kev) was used. It uses a Ga+ ion beam to raster over the surface of a sample. The generated secondary electrons are collected to form an image of the

surface of the sample. The number of secondary electrons reaching the detector depends on the channelling probability of the gallium ions in the grains, which results in a strong grain orientation contrast. Grains with an open crystallographic orientation with respect to the incident ion beam appear darker in the image. As a result, grain morphology can be readily imaged without resorting to chemical etching. The grain boundary contrast can also be enhanced through careful selection of imaging parameters.

The ion beam allows the milling of small holes in the sample at well localised sites, so that cross-sectional images of any layered structure can be obtained. Ions can cut away (mill) material from a defined area with dimensions typically in square microns. Milling is achieved by accelerating concentrated gallium ions to a specific site, which etches off any exposed material, leaving a very clean hole or surface. In this study, cross-sectional images were also made by sputter-etching a hole into the film with 9pA ion beam where the tilting angle of specimens is 45°.

In this study, FIB is also used to prepare samples for transmission electron microscope (TEM). The TEM requires very thin samples, typically of about 100 nanometres. Other techniques, such as ion milling or electro-polishing can be used to prepare such thin samples. However, the nanometre-scale resolution of the FIB allows the exact thin region to be chosen. This is vital, for example, in integrated circuit failure analysis. If a particular transistor out of several million on a chip is bad, the only tool capable of preparing an electron microscope sample of that single transistor is the FIB.

B. Electron backscatter diffraction (EBSD)

EBSD is a microstructural technique used to examine the crystallographic orientation of materials, which can be used to elucidate texture or preferred orientation of any crystalline or polycrystalline materials. It is mainly applied to crystal orientation mapping, phase identification, and grain boundary studies. Generally EBSD is conducted using a Scanning Electron Microscope (SEM) equipped with a phosphor screen, compact lens and low light CCD camera. All samples were investigated using a ''XL30''-SEM from FEI (oil-free system), and the ''Channel 5'' equipment and software from HKL (Oxford Instruments).

4.3.3 Quantitative microstructural analysis

Copper grain size and grain size distribution were determined with a computer program for quantitative microstructure analysis (analySIS, Soft Imaging System GmbH) using digitised FIB images. For grain size analysis, a series of FIB images with the respective tilt angles of 0°C and 45°C were taken of both a surface and cross-section area, respectively. Afterwards, the linear

intercept method was adopted to acquire the value of the grain size and grain size distribution. In this approach, a test pattern of lines of known length is randomly laid over a plane section, and the individual intercept lengths across features of interest are measured. The data is ranked, and then grouped into an arbitrarily determined number of size bins of set size increment.

4.3.4 Surface analysis

Surface roughness reflects the microstructure of the film in terms of grain size. The surface roughness measurement was done with a digital holography microscope (DHM 1000 family, from Lyncée Tec). Two inherent beams with slightly different propagation directions interfere with each other and then form a hologram. The subsequent reconstruction of intensity and phase with the use of Koala software gives the topography (3D) of the sample.

5 Experimental results

The stress evolution of electroplated Cu films in the thickness range of 1.5μm to 20μm measured by the wafer curvature technique is presented in this chapter. The first part shows the stress evolution at room temperature along with the change in microstructure and sheet resistance. The second part shows the stress evolution at elevated temperatures, development of microstructure, grain size, and surface roughness as a function of different annealing temperatures.

5.1 Self-annealing of electroplated Cu films at room temperature

Recrystallisation of electroplated Cu films at room temperature, which is termed self-annealing, is a very distinct phenomenon [104, 107, 129-131]. Microstructure evolution occurs during a transient period of hours following deposition and includes an increase in grain size, change in film stress and decrease in sheet resistance. The self-annealing process impacts upon subsequent processing steps which may require expensive post-deposition treatments and cause reliability impairment. A fundamental understanding of the self-annealing phenomenon is of great scientific and technological importance in order to ensure the stability of electrodeposited Cu metallisation.

So far, most research efforts have been devoted to electroplated Cu films with thicknesses ranging from several hundred nanometres up to about 2μm [129, 130, 132-141], but was recently extended to studies on 70μm thick electroplated Cu films [142, 143]. In these studies, grain growth was observed during room-temperature annealing, accompanied by a continuous relaxation of film stress and sheet resistance [129, 136, 140, 141]. The grain growth is believed to be either induced by the initial high dislocation density triggering recrystallisation or by surface segregation of impurities releasing the pinned grain boundaries [134-136, 144]. If the stress is initially compressive [136, 145], grain growth and annealing of defects will cause stress reduction. However, for films which are initially under tensile stress after deposition [129, 133, 140, 141], grain growth would increase the tensile stress and therefore cannot explain a stress decrease. In such cases other mechanisms must be active, as discussed in this chapter.

In the present study I focused my attention on the onset of stress relaxation for the film thickness range 1.5μm to 20μm which, to the best of our knowledge, has not yet been investigated. In this thickness regime, the grain size should span from approximately 50nm directly after deposition to the dimensions which are finally comparable to the film thickness after the grain growth. For this change in grain size a strong size effect in plasticity should exist,

which might shed new insights into the self-annealing phenomenon of electroplated Cu films. In addition, the investigated thickness range of the electroplated Cu films covers the relevant thickness as used in power devices with their high demand on current capacity and heat dissipation [146].

5.1.1 Stress evolution

In order to determine the film stress evolution of electroplated Cu films at room temperature, the wafer curvature was monitored using a capacitance method, starting from 30 minutes after film deposition to about 100 hours. The stress curves of electroplated Cu films with different thicknesses are presented as a function of time.
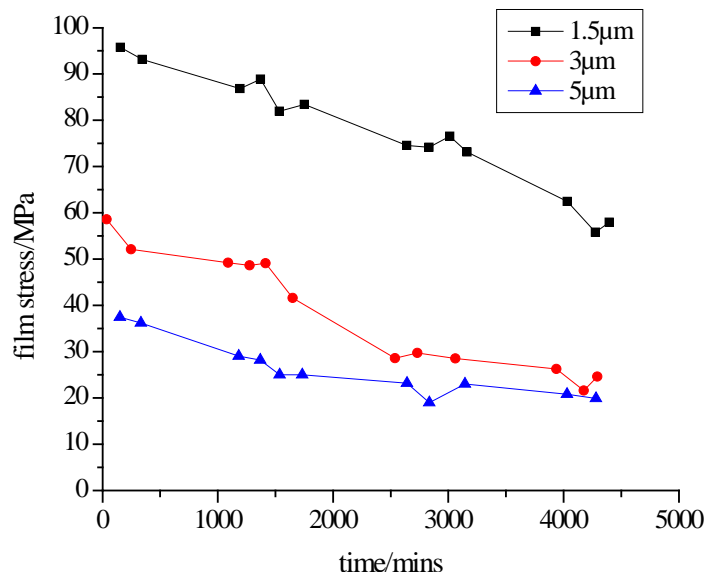
Figure 5.1: Film stress of 1.5μm thick Cu film decreases constantly during room-temperature annealing, while the film stress of the 3 and 5μm thick Cu films decreases within ~50hr and subsequently saturates after ~70hr, where the measurement was terminated.

The evolution of the film stress for1.5–5μm Cu films is summarised in Figure 5.1. The average film stress was determined by the wafer curvature measurement based on the capacitance method. Each stress measurement was repeated 5 times and the average value is plotted. The error bar of film stress is determined by the deviation percentage of each measurement value to the average value. Initially, all films exhibit a tensile stress. The initial stress differs largely from ~37MPa to ~95MPa, depending on the film thickness. The thinner film shows a higher initial stress. As time elapses, stress continuously decreases in all the films. At the end of this experiment, the stress value of 3μm and 5μm thick Cu films is almost equal with respect to the residual stress, while the film stress of 1.5μm thick Cu films still has relatively much higher residual stress value after a measurement time of about 73 hours. The total reduction of the film

stress of each film during measurement is also film thickness-dependent. The thinnest film (1.5μm) shows the maximum stress relaxation, while the 5μm thick Cu film shows a relatively flat tendency of stress relaxation.
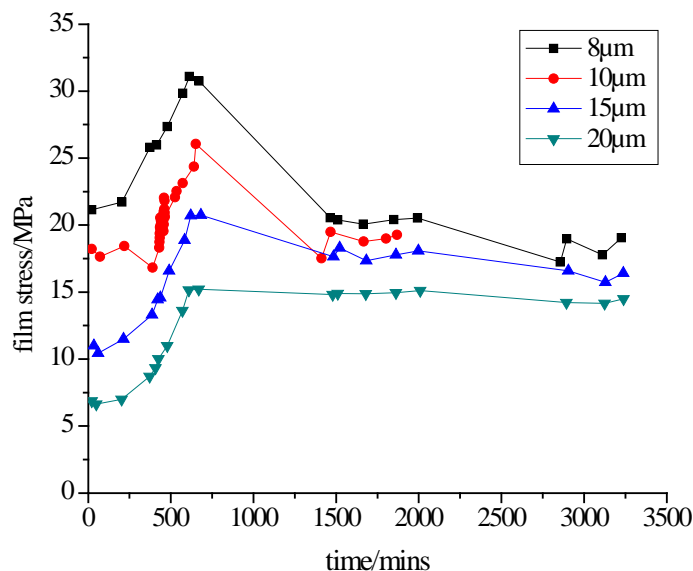
Figure 5.2: Film stress of 8–20μm thick Cu film increases until about 12 hours after deposition and then decreases or stagnates.

The evolution of the film stress for 8–20μm thick Cu films is summarised in Figure 5.2. Surprisingly, their tendency of film stress evolution is quite different compared with thinner films. Initially, all films exhibit a tensile stress. The initial stress differs from ~7MPa to ~22MPa depending on the film thickness. The thinner film shows a higher initial stress. After some time has elapsed, the stress in all the films first shows an increase and subsequently decreases considerably or stagnates, depending on the film thickness. The peak value of stress for all the Cu films occurs at ~700min after measurement starts. After ~1500min, the stress value of 8–15μm thick films begin to stagnate, while for the 20μm thick Cu film the stress stagnates as soon as it reaches the peak value and no remarkable decrease of the stress is observed. At the end of this experiment, the film stress of all Cu films has an almost equal residual stress value. Nevertheless, the final residual stress still shows an inverse relation to film thickness.

The above results clearly show an influence of the film thickness on the stress evolution. This becomes even more evident when comparing the stress-time evolution of all the films in the total designed thickness range from 1.5 to 20μm (Figure 5.3). All films are under tensile stress. Thin Cu films (1.5–5μm) have relatively high initial stress (>~35MPa) compared to thick Cu films (8-20μm, <~21MPa). The evolution of the film stress with time shows a disparate tendency between these two groups:

i)   ''thin'' films with the thickness of 5µm and below;

ii)   ''thick'' films with the thickness of 8µm to 20µm.
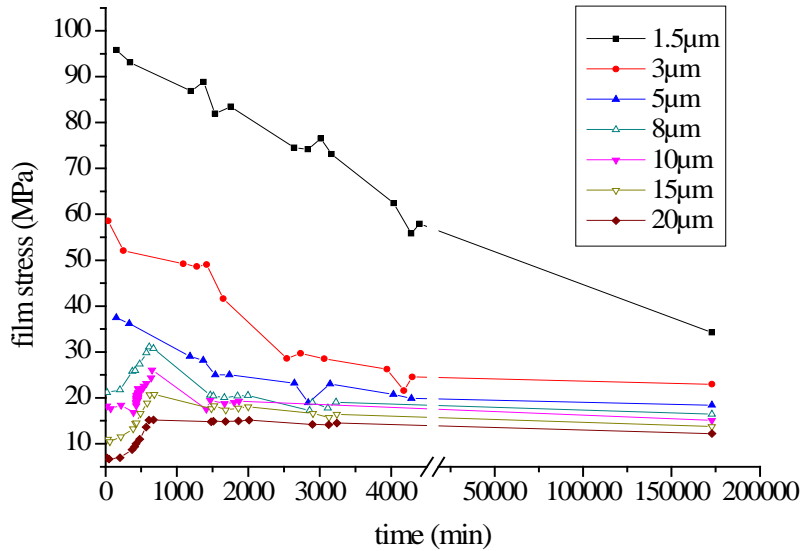
Figure 5.3: The film stress evolution of electroplated Cu films (1.5–20µm).

The tensile stress of thin films continues to decrease with time, while for thick Cu films the stress first increases and subsequently, after ~700min, begins to decrease or stagnate, depending on the maximum stress value. It is also worth noting that within the first ~200min, 8–20µm thick Cu films exhibit an incubation period, where the stress remains rather constant, while this is not observed for thin Cu films. The film stress has been re-measured after ~4 months to detect the saturation. Finally, the tensile stress values of all Cu films stagnate at a certain stress value, which is determined by the film thickness (grain size). Thicker films reveal a lower final residual stress than thinner films. Interestingly, the initial film stress also shows an inverse relationship to film thickness.

The initial and final residual stress was extracted for each film thickness and is plotted as a function of the inversed film thickness in Figure 5.4. This indicates clearly the linear dependence of initial and final residual stress on the inverse film thickness.
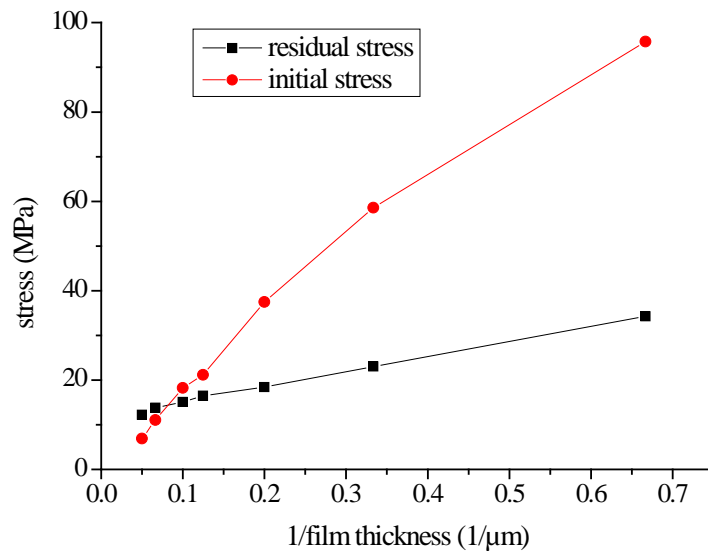
Figure 5.4: The initial stress and final residual stress vs. the inverse film thickness. A quasi-linear dependence is observed for both stresses.
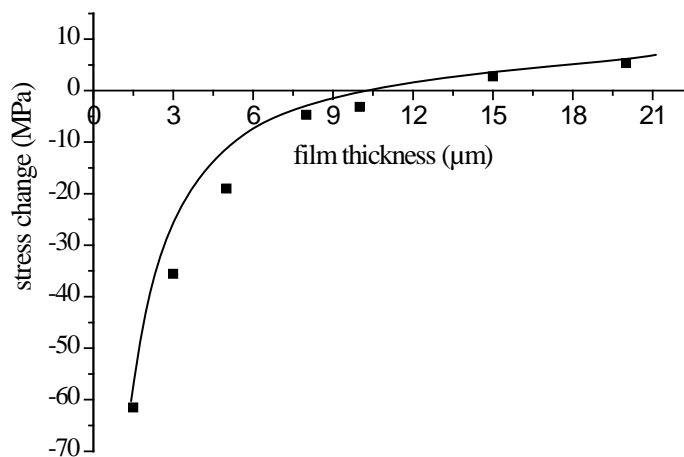
Figure 5.5: Stress change is plotted vs. film thickness, which shows an exponential tendency.

Depending on the film thickness, the stress change which is defined as the value of final residual stress deducted from initial stress differs. In order to show it more clearly, the stress change is plotted as a function of film thickness in Figure 5.5. The amount of stress change decreases exponentially according to the increasing film thickness. The significant stress change occurs only in thinner films (1.5–5μm). For thicker films (8–15μm), the amount of stress change fluctuates near zero, though we observed that the stress evolution shows a stress peak. For 20μm thick Cu film, the amount of stress change is slightly raised, though it nearly enters into the saturation phase.

5.1.2 Sheet resistance evolution

For the sheet resistance change with time, three regions are observed as presented in Figure 5.6.

I) Within the first ~500min, all Cu films, irrespective of their thickness, exhibit a period of weakly decreasing sheet resistance, which in the literature is often referred to as an incubation period [135, 136, 147]. A small drop (<1%) of the sheet resistance for all Cu films can be observed.

II) A noticeable decrease of sheet resistance occurs, which is termed the transient region. The transient time depends on the film thickness. For the 1.5μm thick Cu film, no stabilisation is achieved within 4500min.;

III) The sheet resistance has been measured again after 4 months, indicating a stagnation of the normalised sheet resistance.
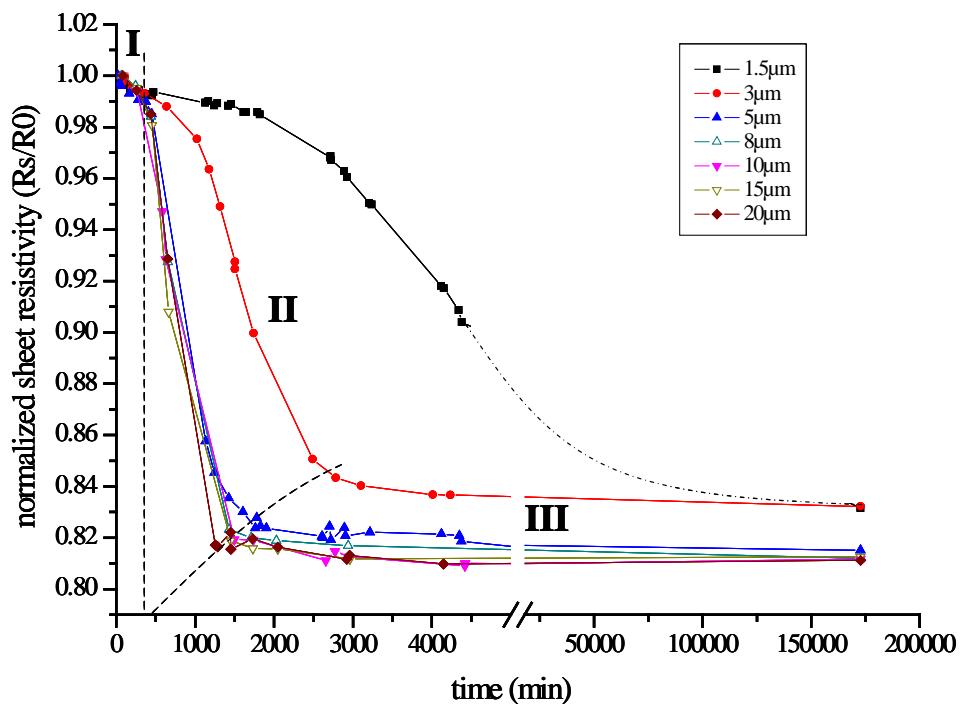
Figure 5.6: Sheet resistance evolution of electroplated Cu films (1.5–20μm). The dash-pointed line for the 1.5μm thick Cu film connects the data points of ~4500min and ~4 months. I) incubation phase; II) transient phase; III) stagnation phase.

This general behaviour leads to converging of normalised sheet resistance vs. time curves for film thicknesses of 5μm and larger, which results in a decay of ~20%. In contrast to that, region I and II are smoother for the 1.5μm and 3μm thick film compared to 5μm and thicker films.
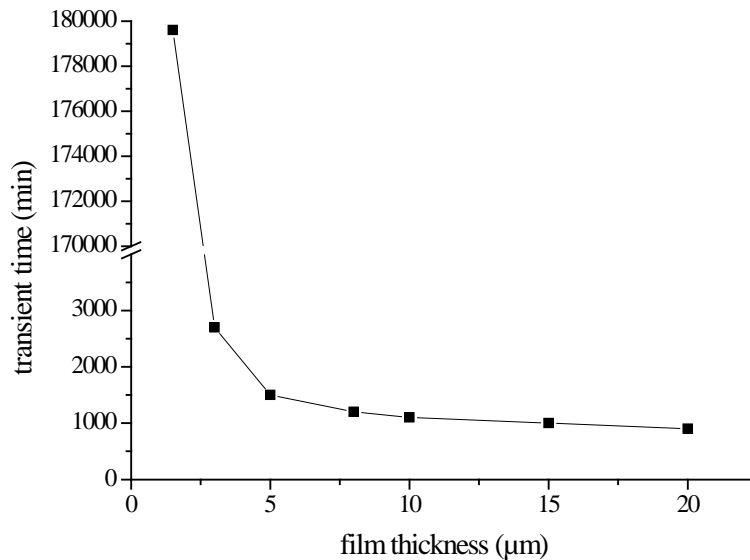
Figure 5.7: Transient time is plotted vs. film thickness. Transient time is defined as the time period of the sheet resistivity decrease as shown in the region II in Figure 5.6..
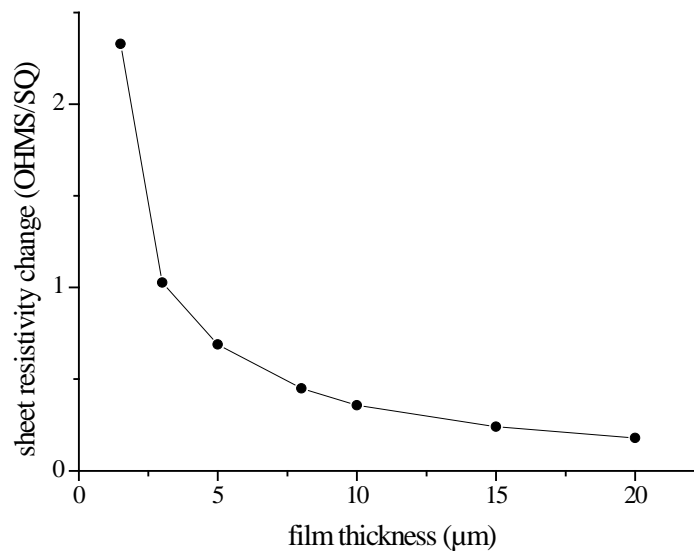
Figure 5.8: Sheet resistance change is plotted vs. film thickness.

The transient phase represents the kinetics of the self-annealing of Cu films. Therefore, it is meaningful to plot the transient time as a function of film thickness explicitly, as done in Figure

5.7. The transient time is defined as the time period of sheet resistivity decrease which is illustrated in the region II for the various films shown in Figure 5.6. For the Cu films below a film thickness of 5μm, the transient time strongly depends on film thickness. The transient time dramatically increases in relation to the decrease in film thickness. As one can see in Figure 5.7, the 1.5μm thick Cu film needs a significantly longer transient time before the sheet resistance reaches saturation. For Cu films above a film thickness of 5μm, the transient time is fairly similar.

The overall change of the sheet resistance is also plotted as a function of film thickness in Figure 5.8. The sheet resistance change is film thickness-dependent, too. The sheet resistance change decreases with increasing film thickness and reaches stagnation above the film thickness of 8μm.

5.1.3   Microstructure characterisation

In order to correlate microstructure changes with the evolution of the sheet resistance and film stress, FIB images have been taken and are shown in Figure 5.9. The first FIB image taken 2 hours after deposition reveals a fine globular grain structure with an average grain size of 105nm. A cross-section has been cut in the film which is imaged at a tilt angle of 45° in order to resolve the surface and cross-section. Note that the coarse grains which have formed at the intersection of the film surface and cross-section are due to the FIB ion bombardment, which provides local energy for grain growth. These grains were neglected when calculating the mean grain size. After 20 hours, a significant change in grain size has occurred. The grains which frequently contain twins now have a bimodal grain size distribution with average grain sizes of either ~190nm or ~1000nm. Note that at the Cu/substrate interface, a ~300nm thick region of fine grains (~105nm in size) still exists. After 44 hours, all fine grains have been consumed by large grains. Some of the grains (columnar grains) extend through the complete thickness but contain twins. The coexistence of columnar grains and twins again leads to a bimodal grain size distribution of ~220nm and ~1300nm, exceeding the bimodal grain sizes after 20 hours.
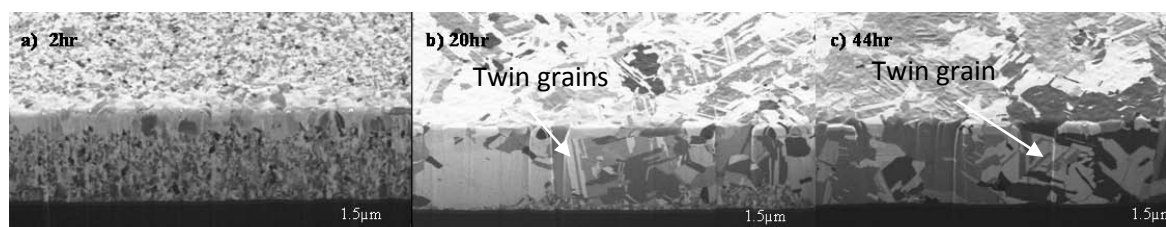
Figure 5.9: Microstructure evolution of a 3μm thick Cu film, imaged with FIB using secondary electrons.
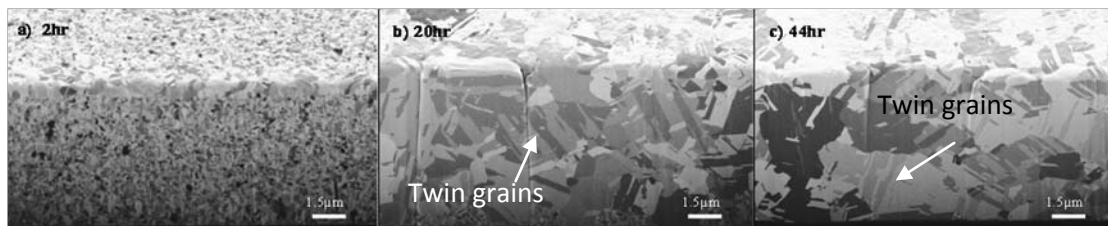
Figure 5.10: Microstructure evolution of an 8µm thick Cu film.
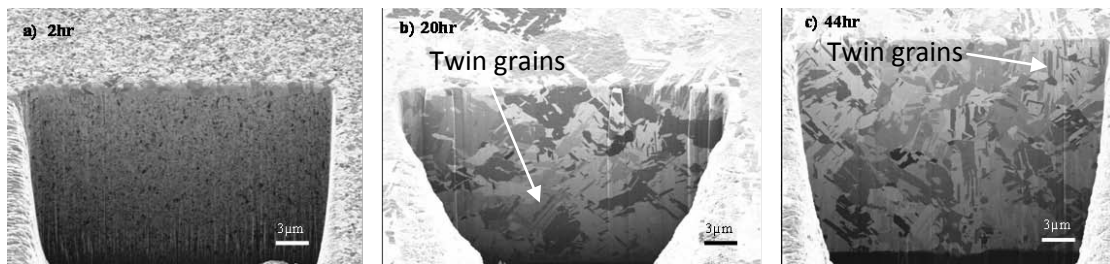
Figure 5.11: Microstructure evolution of a 20µm thick Cu film.

FIB images of the 8µm (Figure 5.10) and 20µm thick Cu films indicate, as in the case of the 3µm thick film (Figure 5.9), that coarse grains form at the surface and then proceed towards the film/substrate interface, with large grains growing at the expense of smaller grains. The grains with the long and narrow strip shape embedded in the large grains are called twins. Twin grains are oriented in a definite, symmetrical way such as a mirror image of the parent crystal. In Figure 5.9-5.11, annealing twins are very noticeable. The energy of annealing twin boundaries is about 5% of the average grain boundary energy [148]. Most FCC metals such as copper form annealing twins.

In Figure 5.12, grain size distribution for 3µm electroplated Cu films is plotted. The data is deduced from the FIB images in Figure 5.9 with the linear intercept method which is well known and widely used to determine grain size in a microstructure by measuring the number of grains per unit length intersected by a number of randomly placed straight lines. The grain size is then equivalent to the mean lineal intercept length. Before grain growth begins, most grains are fine grains which are smaller than 200nm. As soon as grain growth begins, a bimodal grain size distribution is observed which is clearly shown from the grain counts of 20hr and 44hr images. There are small grains (<500nm) as well as large grains (>500nm) coexisting in the Cu film. Based on the linear intercept method, the average grain size at each stage for different Cu films can be obtained and plotted, as in Figure 5.13.
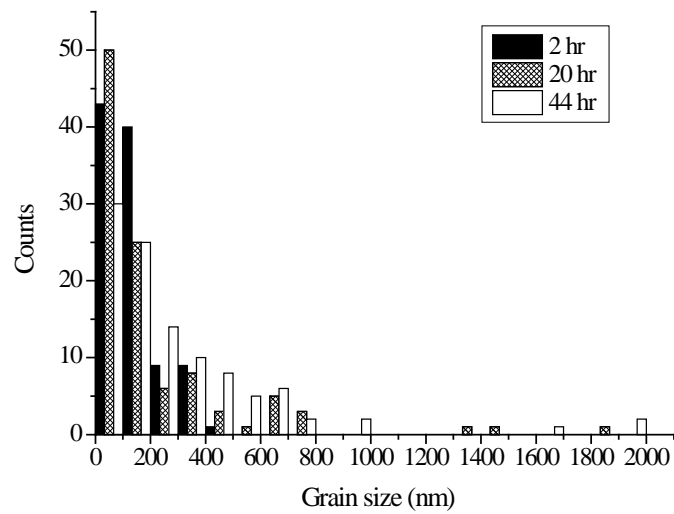
Figure 5.12: Grain size distribution of a 3μm electroplated Cu film during grain growth.
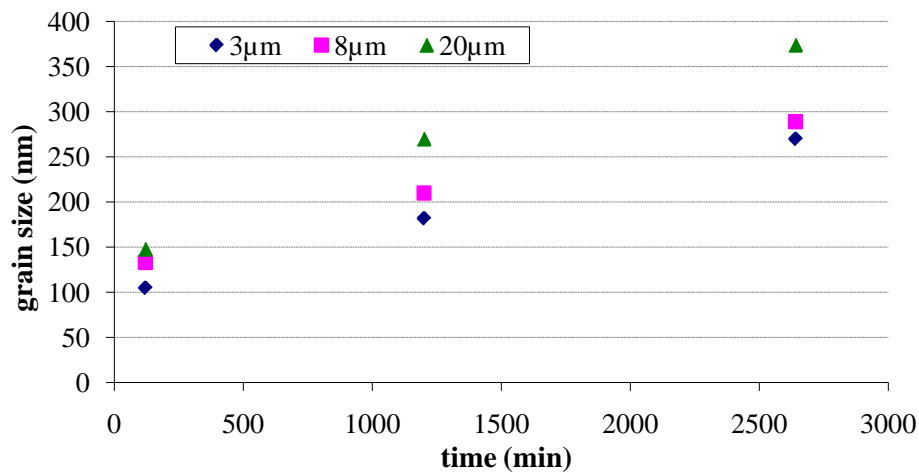
Figure 5.13: Average grain size of 3, 8 and 20μm electroplated Cu films at 2hr, 20hr and 44hr after deposition.

5.2   Thermo-mechanical response of electroplated Cu films at elevated temperatures

Thermo-mechanical properties of materials are known to be highly influenced by microstructure, in particular by the grain size. Earlier studies usually examined electroplated Cu films that were thinner than 2μm [140, 149-154]. Our study therefore aims to extend this knowledge to thicker films up to 20μm. In this thickness regime, where microstructure differs according to various annealing temperatures, different deformation mechanisms are expected and need to be investigated [65, 143].

This study was conducted with electroplated Cu films with the thickness of 1.5–20µm. The electroplating deposition was applied at room temperature and none of the films had any thermal treatment after deposition, but were simply stored at room temperature for more than 2 months. The stress data is acquired by using Stoney's equation based on the measured wafer curvature data. The curvature data is captured at the centre of the wafer within an approximate 1cm x 1cm area, simultaneously during temperature cycles. The multiple laser technique is applied. The concrete measurement approach has been discussed in Chapter 3.3.2. In this way, this real-time measurement ensures that the obtained stress value corresponds to the real temperature. A precise comparison of the stress evolution of all these films with different annealing temperatures will shed new light on the deformation mechanisms and size effects in thin films.

The chapter will be divided into three sections. In the first part, the stress-temperature curves are presented. The second part will be dedicated to the microstructure analysis of all films using the FIB technique. Finally, surface roughness will be described in order to provide a greater insight.

5.2.1 Stress hysteresis during thermal annealing

In this section, stress-temperature curves of electroplated Cu films with different thicknesses at different maximum annealing temperatures will be presented.

In Figure 5.14, stress hysteresis of 20µm thick Cu films is shown. Each annealing cycle with a specific maximum annealing temperature was carried out with a 20µm thick Cu film which was stored for more than 2 months at room temperature after film deposition. The temperature ramp rate of all annealing cycles is 30°C/min. At the onset of the experiment, all films exhibit a tensile initial stress. The stress decreases linearly with a slope of 2.0MPa/K upon heating. In this segment, thermal strain is accommodated predominantly by elastic deformation. The apparent non-linearity of the curve which starts to depart from that of the thermo-elastic line at about 100°C indicates plastic yielding. It finally reaches a maximum compressive stress of 115MPa at about 150°C. Similarly, the thermo-elastic segment is observed at the beginning of cooling. However, the length of the thermo-elastic line decreases by increasing the maximum annealing temperature. During cooling, plastic deformation happens in the tensile stress region.
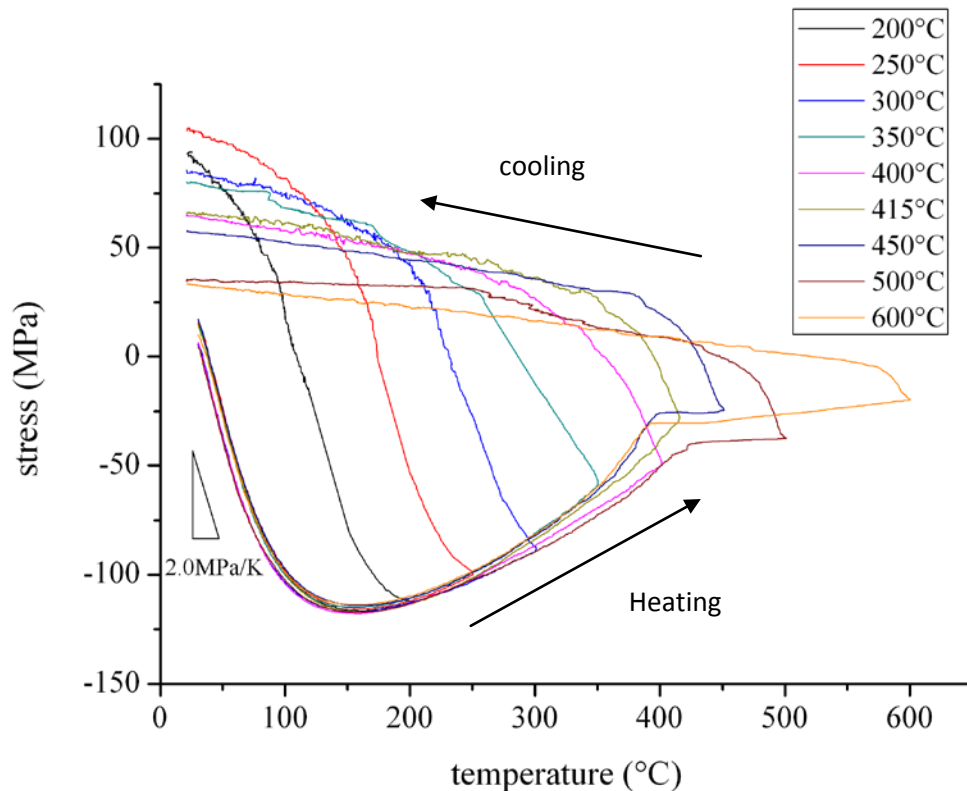
Figure 5.14: Stress hysteresis curves of 20µm Cu films with various maximum annealing temperatures.

The curves of 20µm thick Cu films in Figure 5.14 exhibit several characteristic features:

   i.   during heating from 150°C to 425°C, a significant stress decrease of about 85MPa is observed;

   ii.   the discontinuity of the curves (inflexion point) occurs around 425°C;

   iii. the stress reaches a plateau of about -30MPa after the inflexion temperature point;

   iv.   the residual stress differs according to the different maximum annealing temperature.

For 1.5µm thick electroplated Cu films, the same annealing experiments have been carried out and the results are shown in Figure 5.15. A thermo-elastic segment is also observed at the beginning of the heating regime. The film stress decreases linearly with a slope of 2.5MPa/K, which is slightly larger than that of 20µm thick Cu films. The onset of plastic yielding occurs at approximately 100°C and the maximum compressive stress reaches 200MPa at 175°C. With further heating, a continuous and large stress decrease of 150MPa is also noticeable. There is no stress plateau observed at a high temperature regime. The inflexion temperature point occurs at approximately 270°C, much lower than that of 20µm Cu films. Again, large residual stress

variations among the different maximum annealing temperatures are observed at room temperature after each thermal annealing cycle.
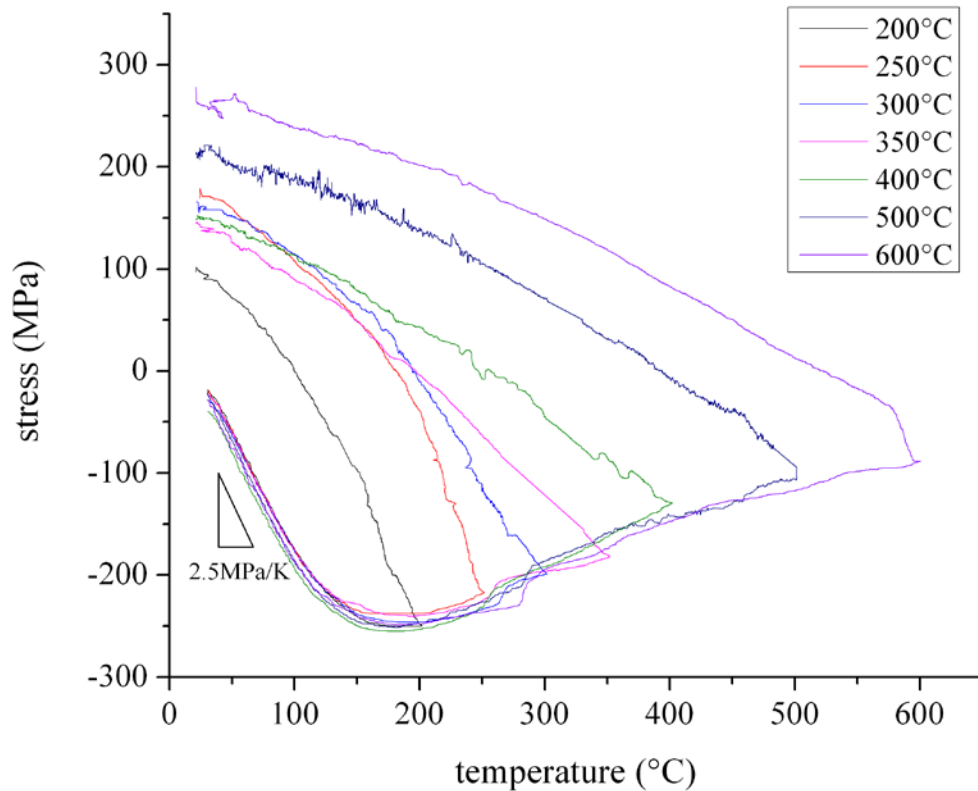
Figure 5.15: Stress hysteresis curves of 1.5μm Cu films with various maximum annealing temperatures.

When comparing stress-temperature curves for different Cu film thicknesses samples in Figures 5.14–5.20, a strong film-thickness effect is observed on the strength of the films as well as on the shape of the stress-temperature curves. The initial stress at the onset of heating increases in relation to a decrease in film thickness. However, this size effect is not observed for the stress upon yielding and the stress at 600°C. Upon heating, stress curves exhibit a plateau above 450°C and 400°C in Cu films with the thickness of 15μm and 20μm, respectively. In contrast, there is no stress plateau observed in the thinner Cu films. Apparently, the discontinuity of the stress curves (inflexion point) occurs at approximately 270°C and 340°C in 1.5μm and 3μm Cu films, respectively. Similarly, the inflexion point appears at approximately 450°C and 400°C in 15μm and 20μm Cu films before the stress curves enter into the plateau region. Surprisingly, for other Cu films (5μm–10μm), there is no inflexion point observed during the heating period.
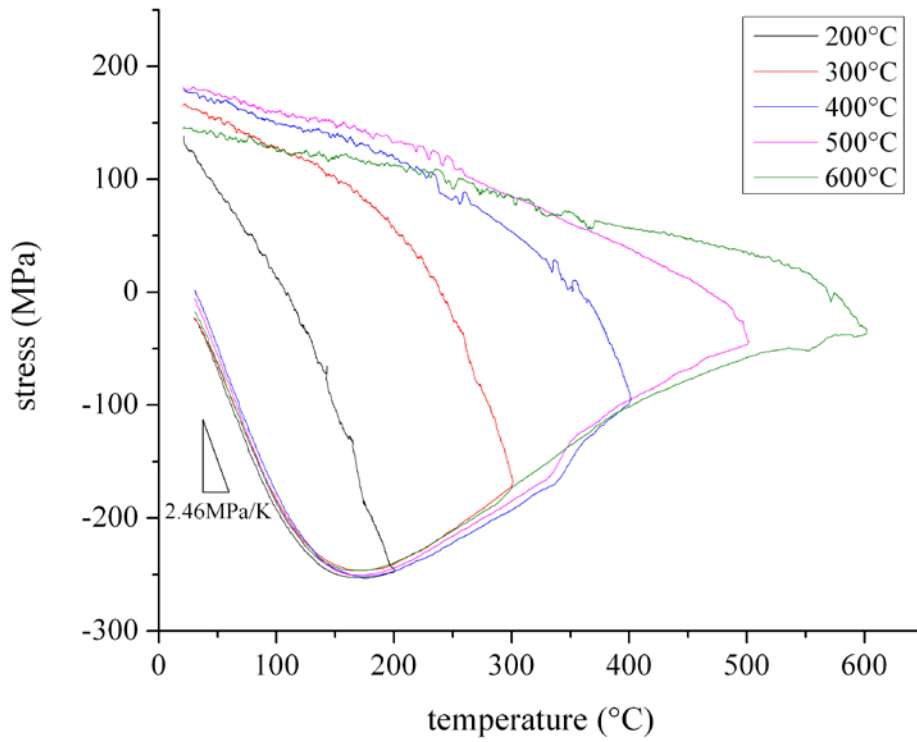
Figure 5.16: Stress hysteresis curves of 3µm Cu films with various maximum annealing temperatures.
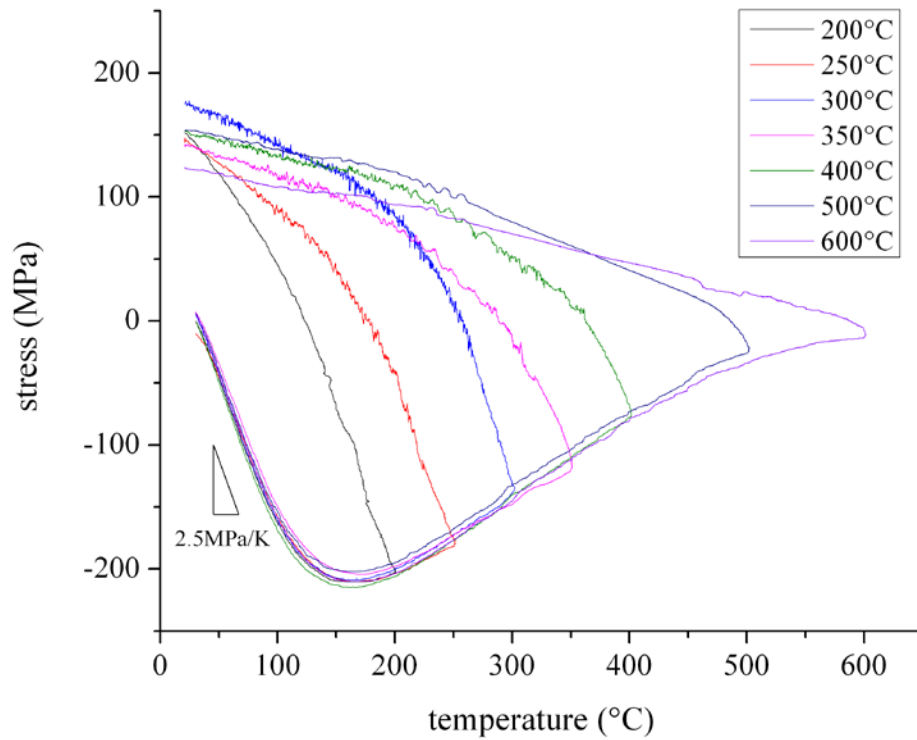
Figure 5.17: Stress hysteresis curves of 5µm Cu films with various maximum annealing temperatures.
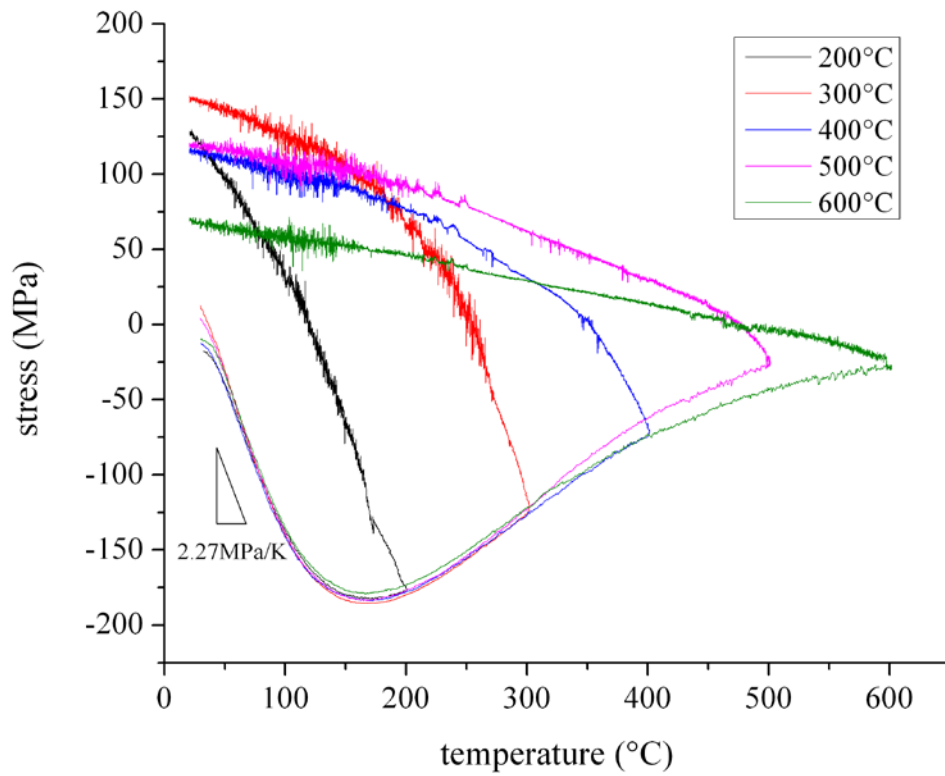
Figure 5.18: Stress hysteresis curves of 8µm Cu films with various maximum annealing temperatures.
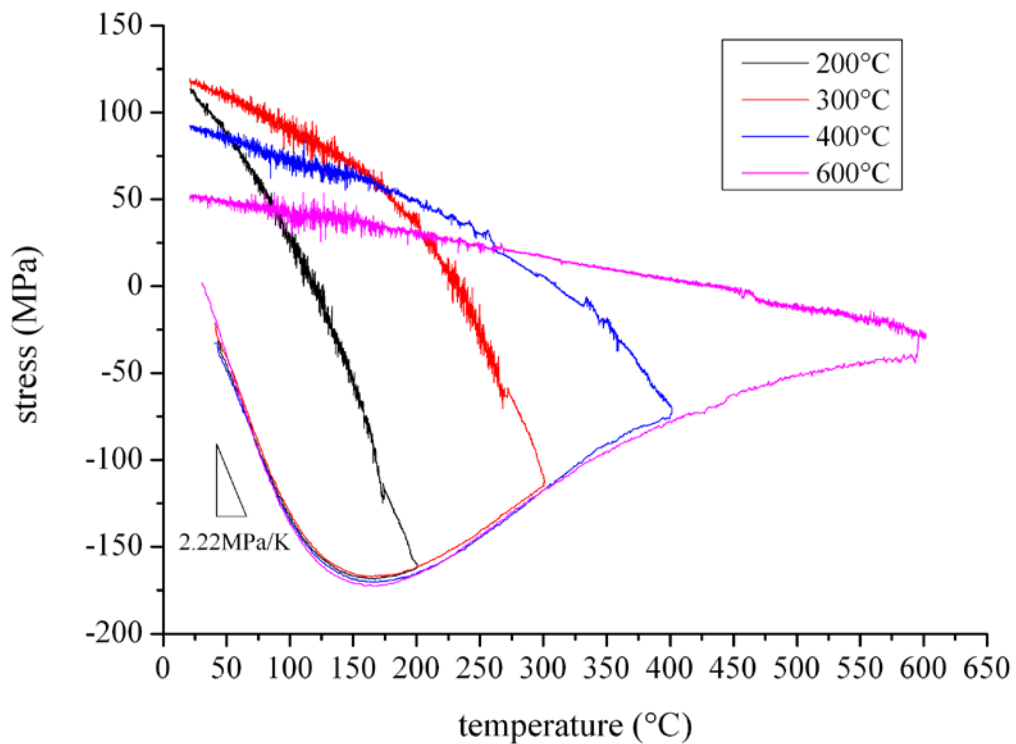
Figure 5.19: Stress hysteresis curves of 10µm Cu films with various maximum annealing temperatures.
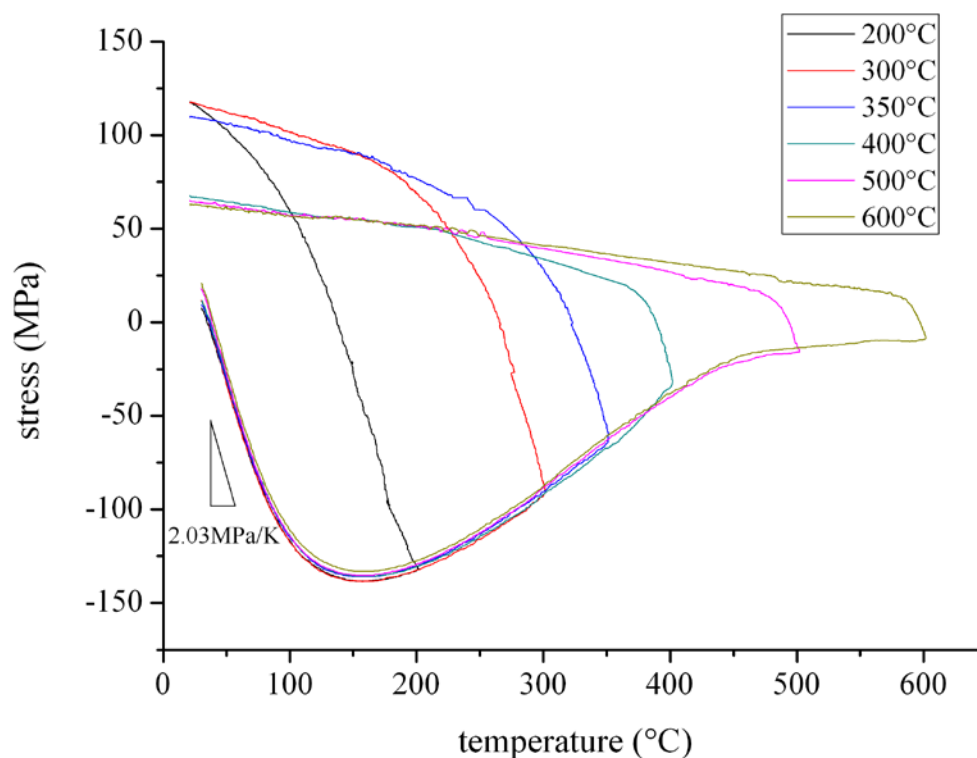
Figure 5.20: Stress hysteresis curves of 15μm Cu films with various maximum annealing temperatures.

5.2.2   Microstructural evolution

The grain structure of Cu films was characterised using the FIB technique. In the FIB micrographs, grains are identified by different grey scales due to the different crystallographic orientation towards the primary ion beam of the FIB.

The grain structures of a cross-section of 20μm thick electroplated Cu films with different maximum annealing temperatures are shown in Figure 5.21. As is evident from these FIB images, there is a significant grain growth from 25°C to 600°C. In Figure 5.21(a), the whole film is occupied by coarse grains in which twins are embedded. In Figure 5.21(f)–Figure 5.21(h), it is interesting to note that 2–3 grains align along the film in a vertical direction. Until 500°C, large columnar grains penetrate through the whole film thickness with few twins embedded, as shown in Figure 5.21(i).
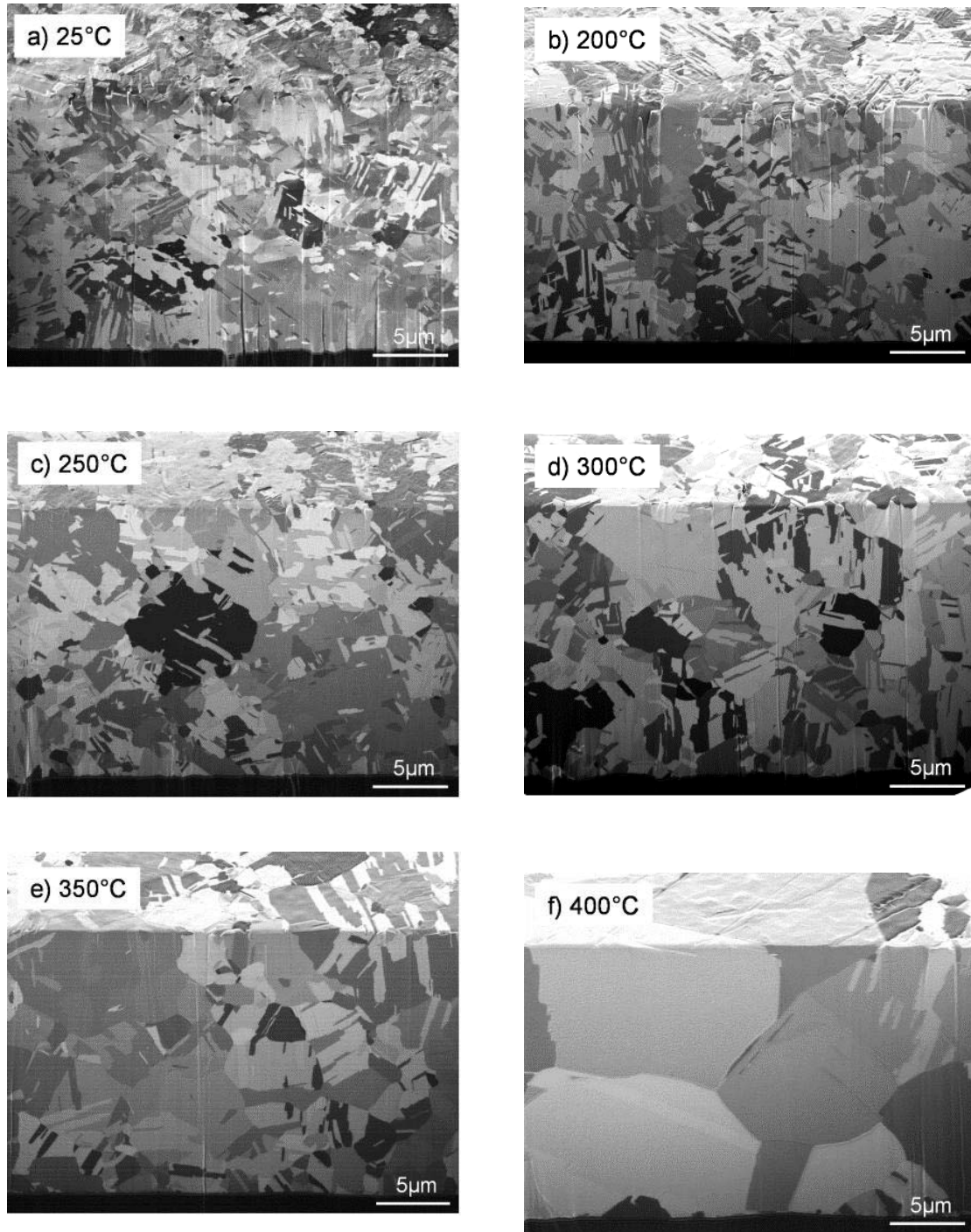
Figure 5.21: FIB micrographs showing the grain structure of the cross-section of 20μm electroplated Cu films at room temperature (a) and after annealing cycles up to 200°C–400°C (b–f). The tilt angle of the sample is 45°. The silicon substrate appears black.
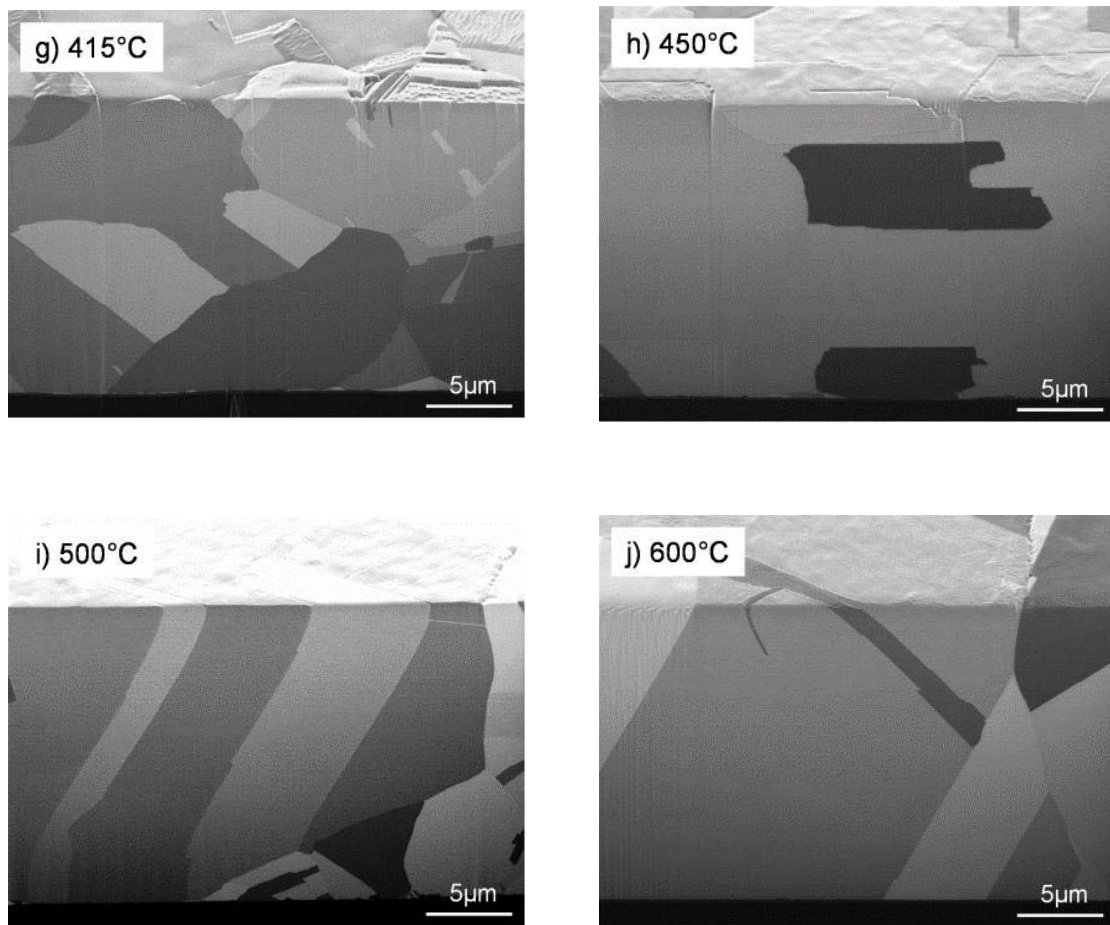
Figure 5.21: FIB micrographs showing the grain structure of the cross-section of 20μm electroplated Cu films after annealing cycles up to 415°C–600°C (g–j). The tilt angle of the sample is 45°. The silicon substrate appears black.

The topography of the films was also studied using the FIB technique. The FIB images in Figure 5.22 show the grain structure at the surface of 20μm electroplated Cu films annealed at different temperatures. In Figure 5.22(a), the Cu film shows a very high incidence of twinning. Grain growth is visible from 200°C up to 600°C. Twins exist during the whole temperature range. Grooves are also visible at some grain boundaries. Annealing hillocks are not observed.
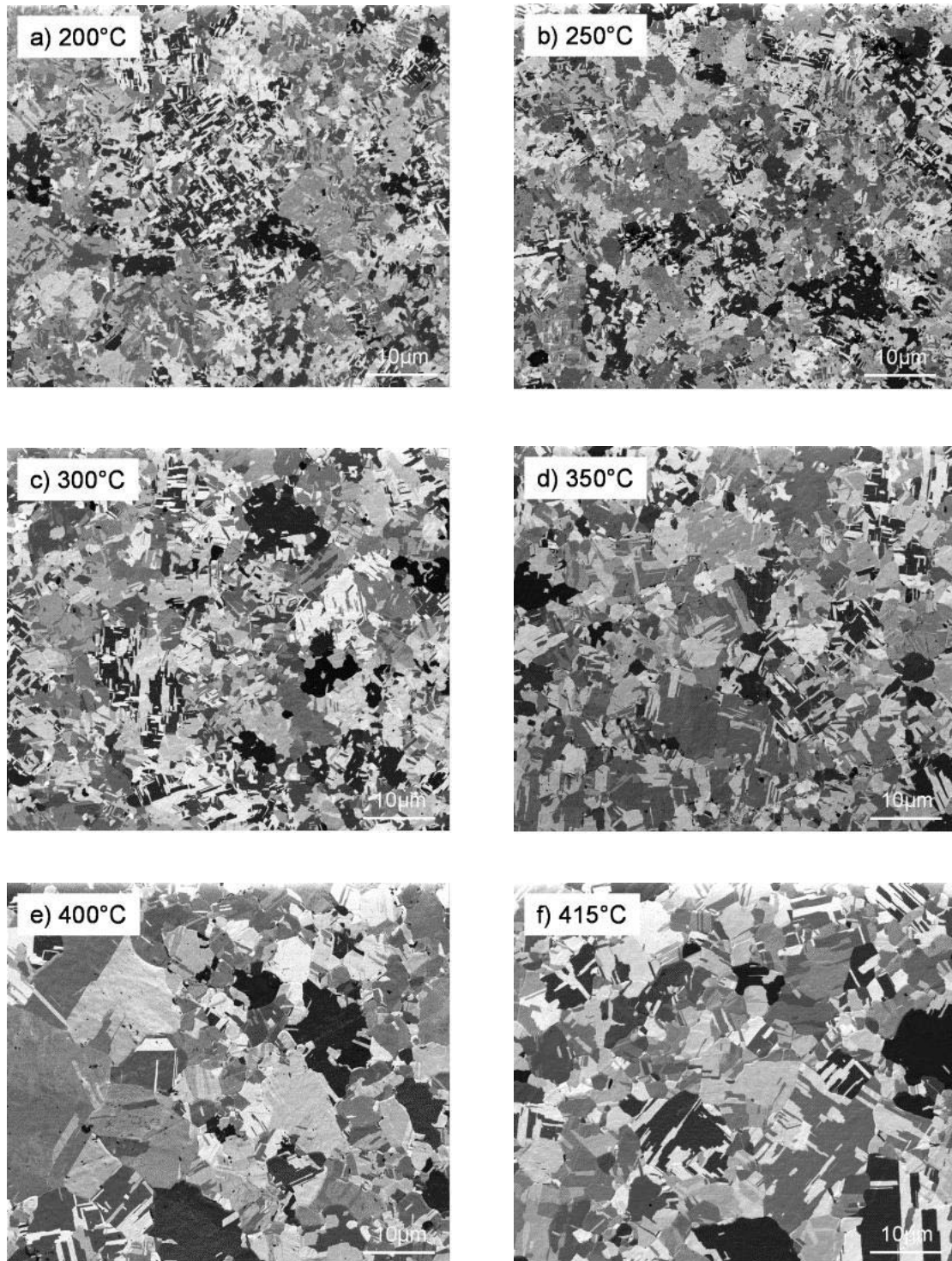
Figure 5.22: FIB micrographs showing the grain structure of the surface of 20µm electroplated Cu films after annealing cycles up to 200°C–415°C (a–f). The sample tilt is 0°.
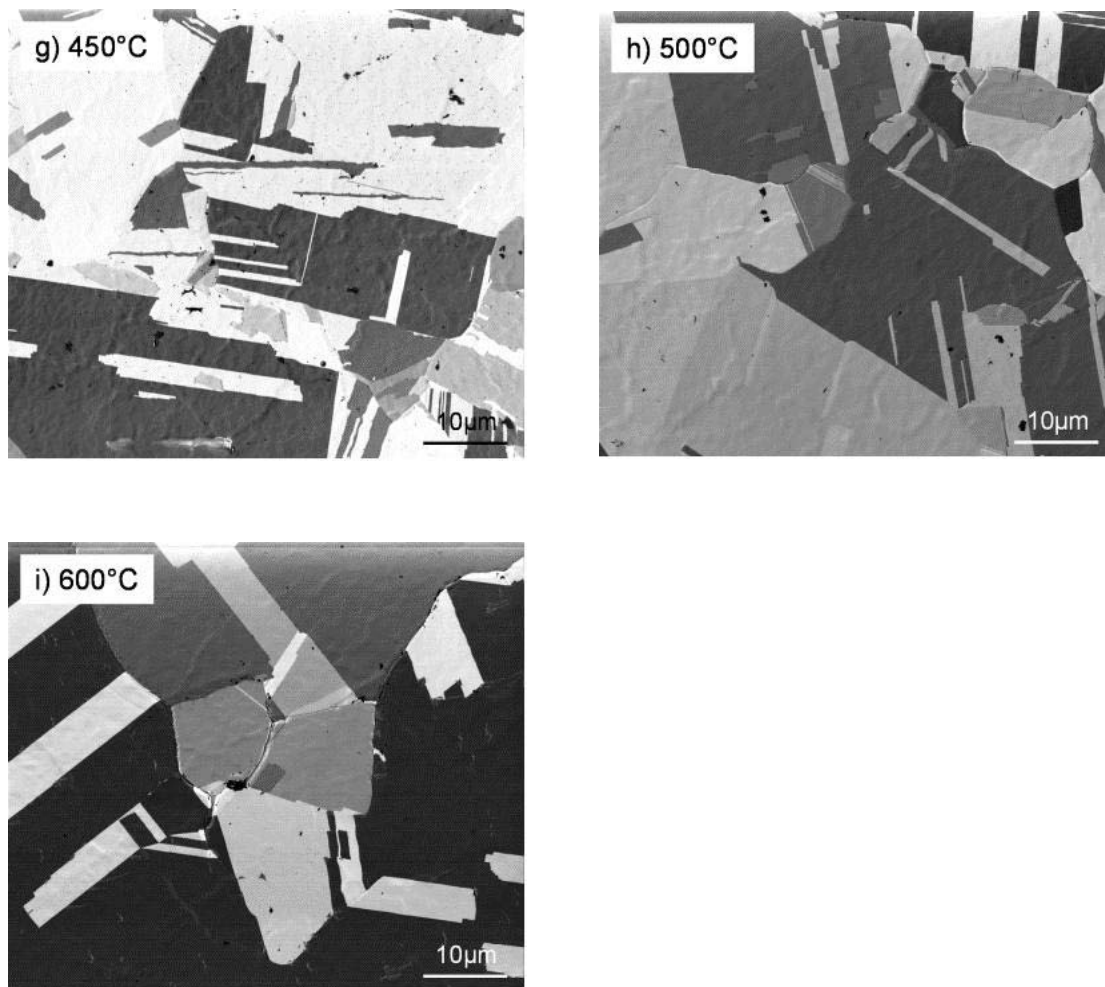
Figure 5.22: FIB micrographs showing the grain structure of the surface of 20µm electroplated Cu films after annealing cycles up to 450°C–600°C (g–i). The sample tilt is 0°.

Similarly, microstructure characterisation of 1.5 and 5µm thick Cu films has been done by FIB technique. The surface and cross-section images can be found in Figure 5.23-5.26. Significant grain growth with increasing annealing temperatures is also observed in both of these films. Interestingly, columnar grains have already penetrated through the whole thickness of 1.5µm Cu films at a low annealing temperature of 200°C. In contrast to that, 5µm thick Cu films have columnar grains dominant in the film until annealed at 500°C. In both films with the annealing temperature above 500°C, a dense oxide, which appears dark at some grain boundaries (mostly at grain grooves), as well as a few faceted protrusions can be seen in these FIB images. It appears that the thinner film has the more severe oxidation at high temperatures as the oxidation region is larger and more obvious.
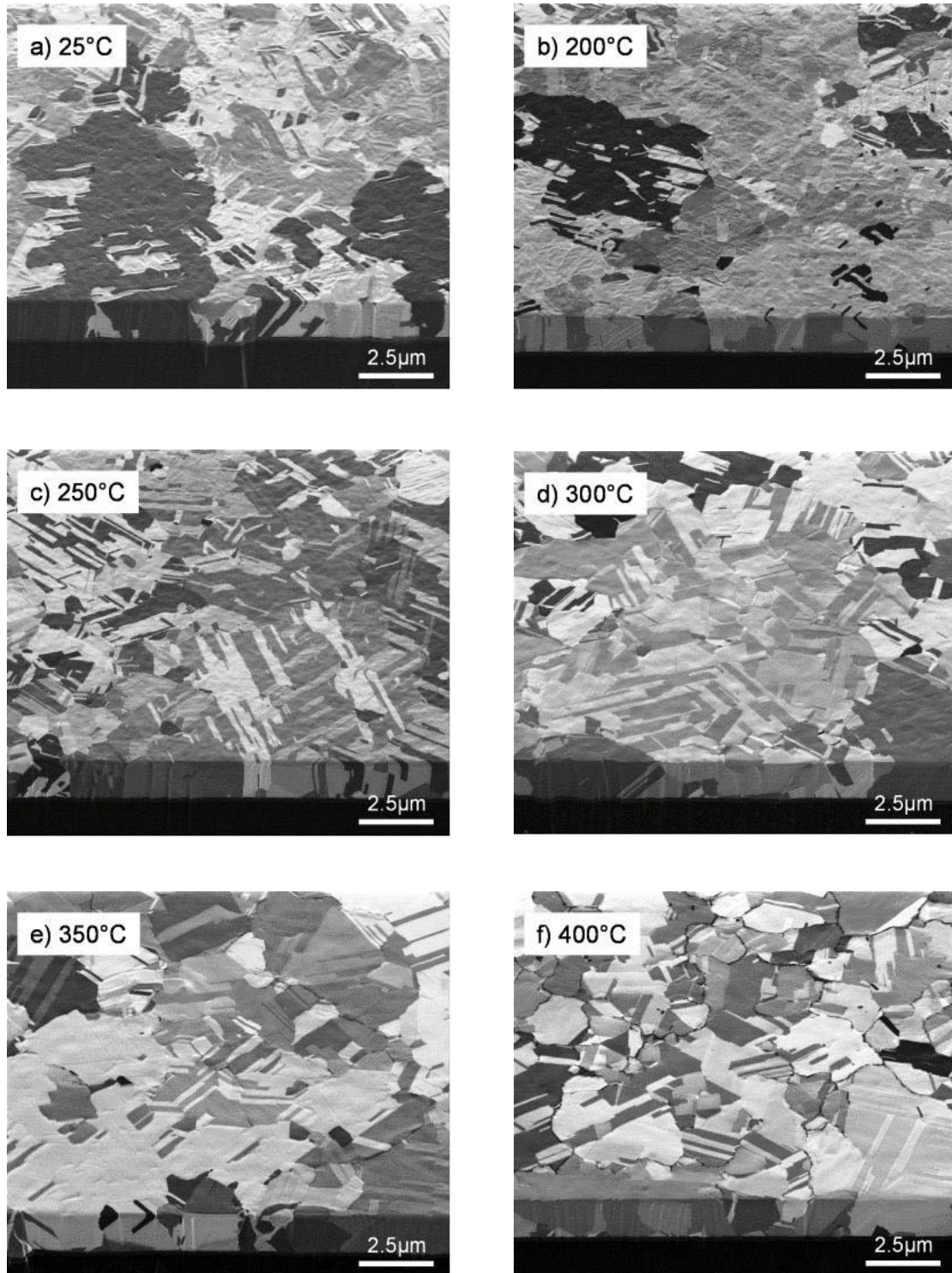
Figure 5.23: FIB micrographs showing the grain structure of the cross-section of 1.5µm electroplated Cu films after deposition at room temperature (a) and after annealing cycles up to 200°C–400°C (b–f). The tilt angle of the sample is 45°. The silicon substrate appears black.
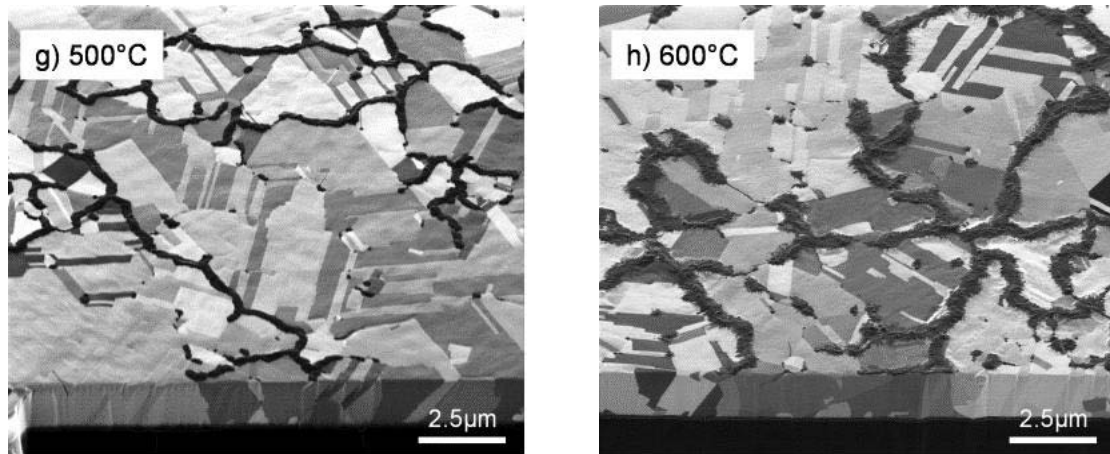
Figure 5.23: FIB micrographs showing the grain structure of the cross-section of 1.5μm electroplated Cu films after annealing cycles up to 500°C (g) and 600°C (h). The tilt angle of the sample is 45°. The silicon substrate appears black.
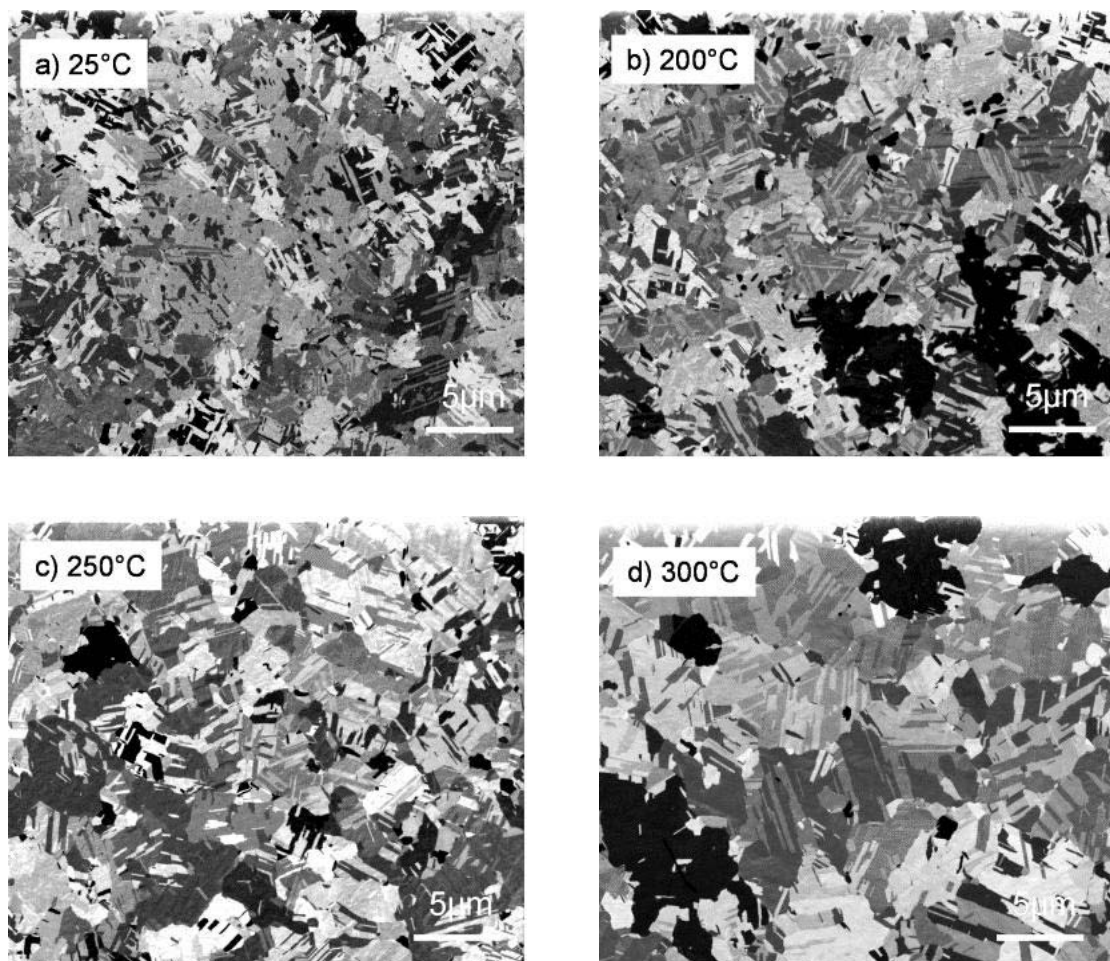
Figure 5.24: FIB micrographs showing the grain structure of the surface of 1.5μm electroplated Cu films after deposition at room temperature (a) and after annealing cycles up to 200°C–300°C (b–d). The sample tilt is 0°.
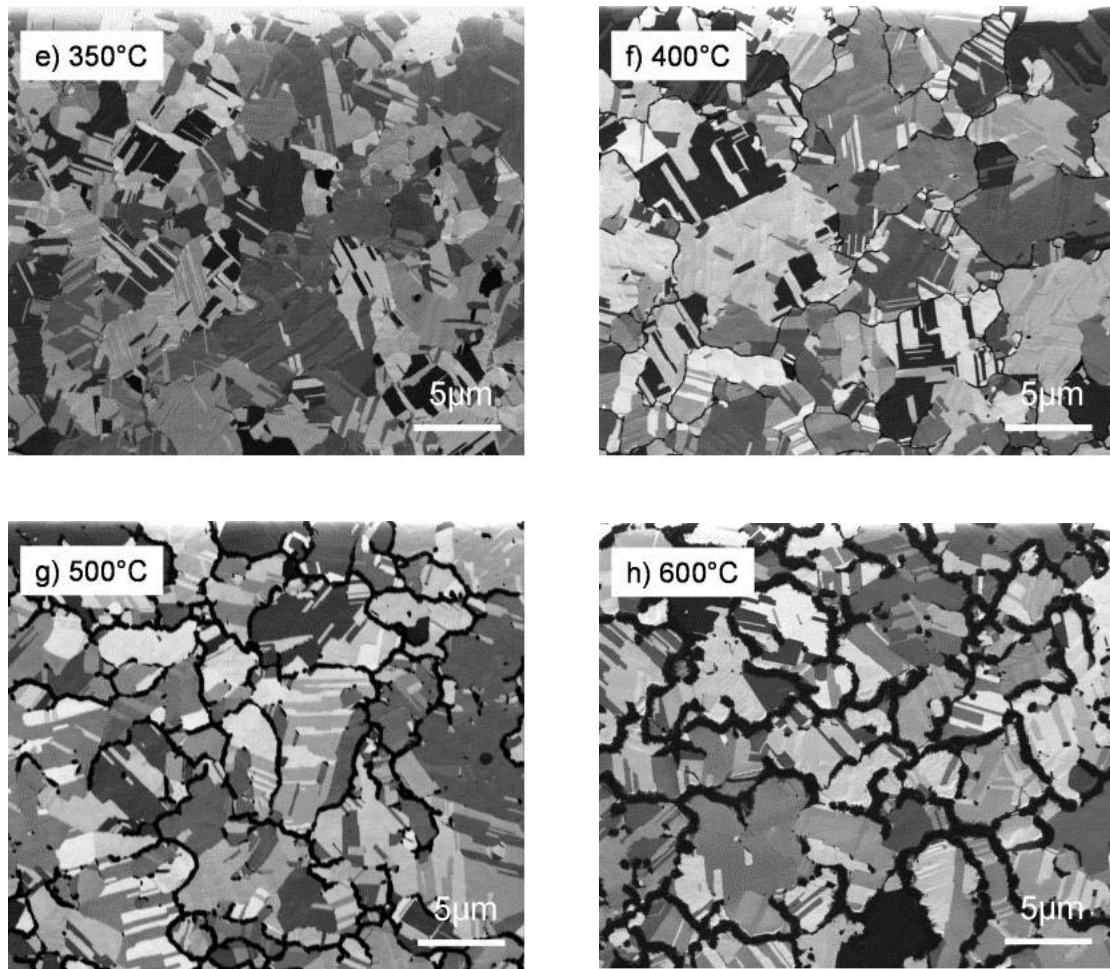
Figure 5.24: FIB micrographs showing the grain structure of the surface of 1.5μm electroplated Cu films after annealing cycles up to 350°C–600°C (e–h). The sample tilt is 0°.
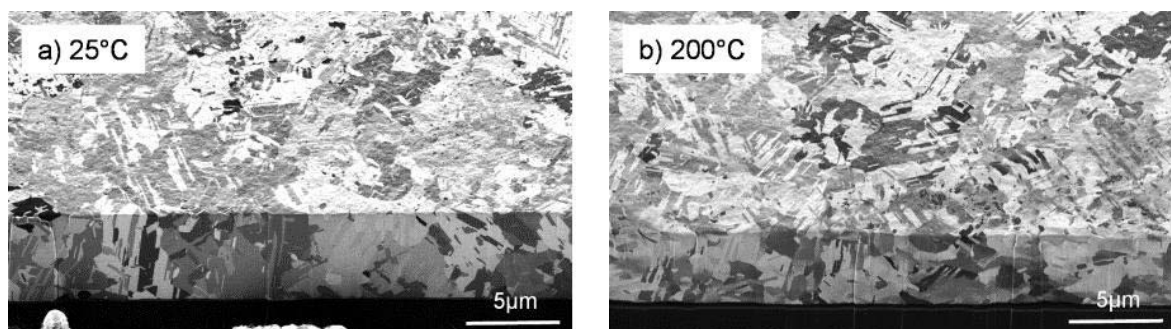
Figure 5.25: FIB micrographs showing the grain structure of the cross-section of 5μm electroplated Cu films after deposition at room temperature (a) and after annealing cycle up to 200°C (b). The tilt angle of the sample is 45°.
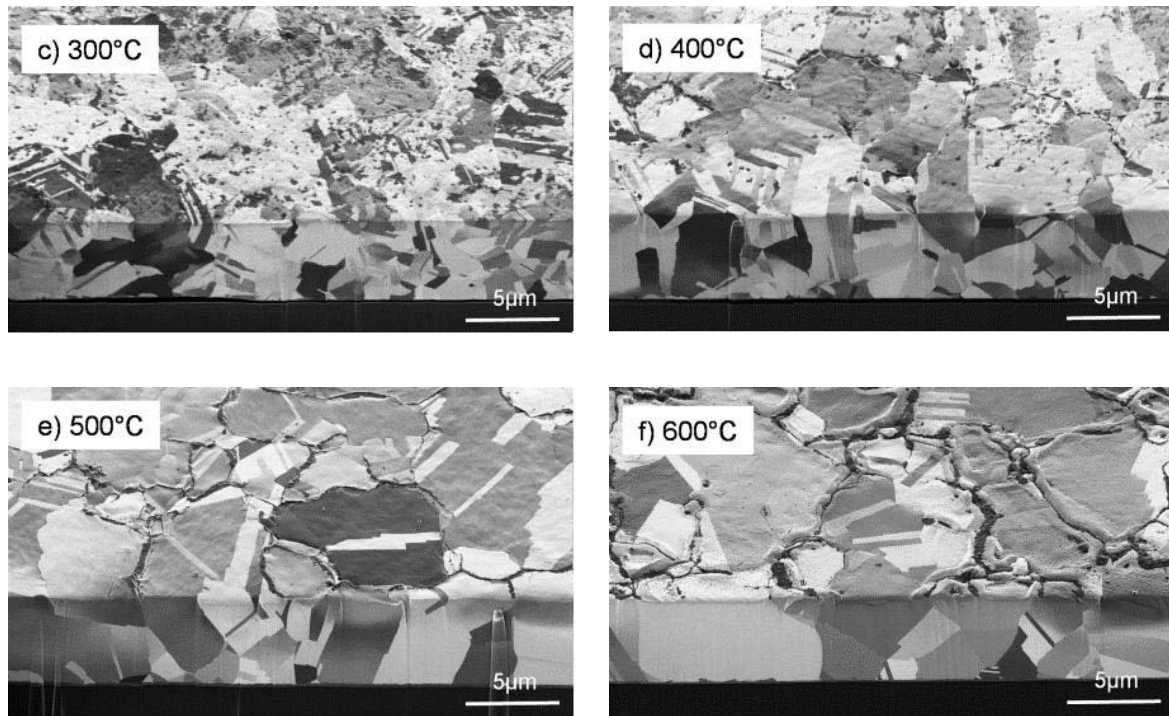
Figure 5.25: FIB micrographs showing the grain structure of the cross-section of 5µm electroplated Cu films after annealing cycles up to 300°C–600°C (c–f). The tilt angle of the sample is 45°.
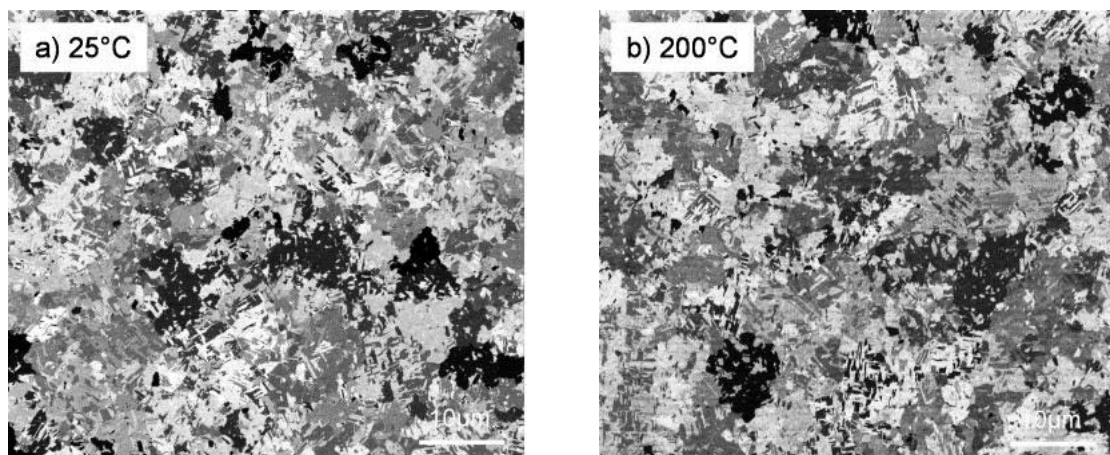
Figure 5.26: FIB micrographs showing the grain structure of the surface of 5µm electroplated Cu films after deposition at room temperature (a) and after annealing cycle up to 200°C (b). The sample tilt is 0°.
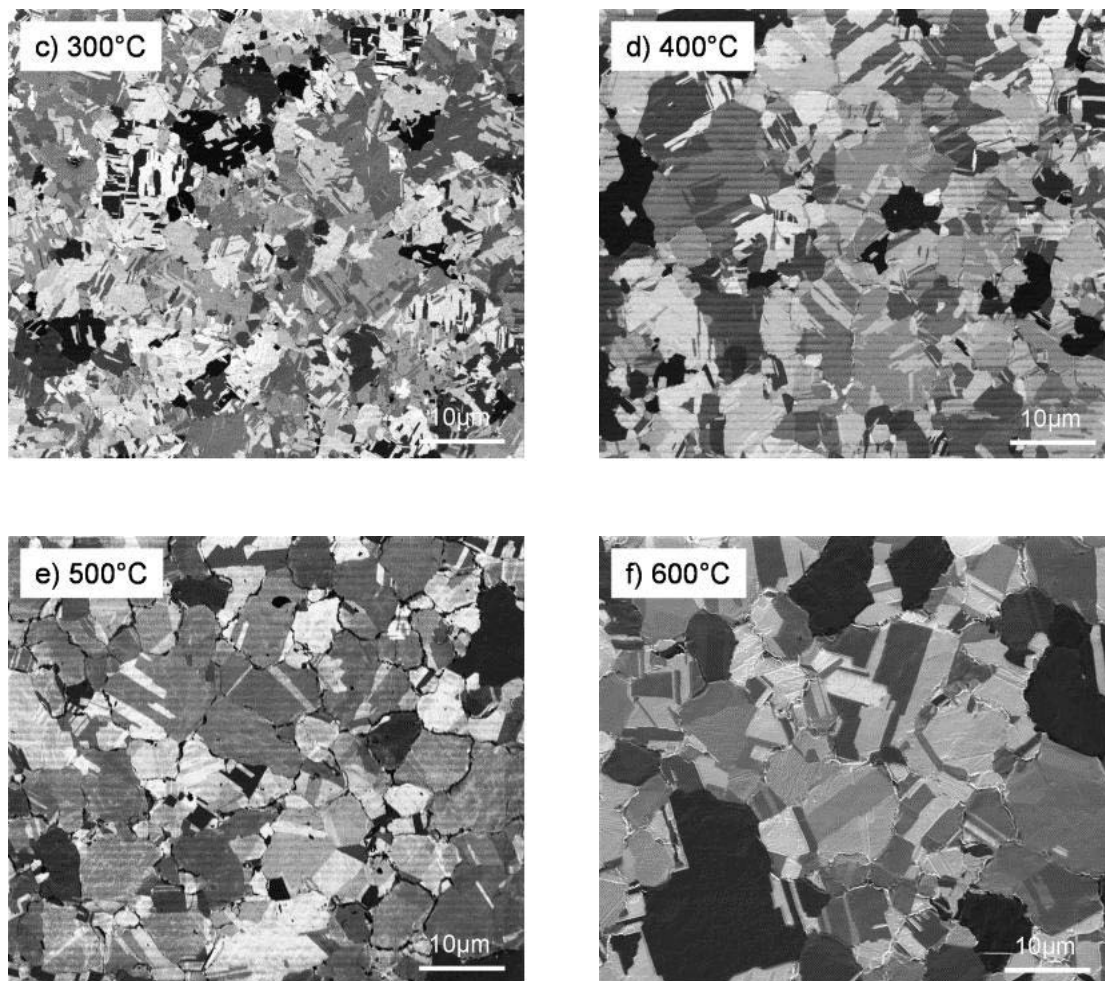
Figure 5.26: FIB micrographs showing the grain structure of the surface of 5µm electroplated Cu films after annealing cycles up to 300°C–600°C (c–f). The sample tilt is 0°.

Based on the FIB images of the film surface in Figure 5.22, 5.24 and 5.26, the average grain size of the 1.5, 5 and 20µm Cu films at each annealing temperature can be calculated with the linear intercept method. Twins are counted as grains. The average grain size of 1.5, 5 and 20µm Cu films is summarised in Table 5-1 to Table 5-3 and plotted in Figure 5.27. The initial grain sizes in these films at room temperature are quite similar, which is about 400nm. Increase in temperature increases the average grain size. Below 400°C, the grain sizes among these three Cu films are quite similar. Starting from 400°C, the divergence of grain size development appears. The average grain size increases much faster in 20µm thick Cu films than in 1.5µm thick Cu films. At 600°C, 20µm thick Cu films end up with an average grain size of about 13µm, while 1.5µm thick Cu films have a final grain size of about 1.4µm. It must be noted that the actual grain size at each temperature should differ from the ones measured in the FIB images, because the FIB is done after each annealing cycle. Therefore, the measured grain size is larger than the actual grain size due to the longer tempering time in the chamber.

Table 5-1: Grain size in 1.5μm Cu films

Temperature (°C)	25	200	250	300	350	400	500	600
Average grain size (μm)	0.44	0.44	0.50	0.66	0.66	0.78	0.97	1.4
Number of accounted grains	468	579	774	595	546	502	405	583

Table 5-2: Grain size in 5μm Cu films

Temperature (°C)	25	200	300	400	600
Average grain size (μm)	0.57	0.58	0.8	1.6	2.9
Number of accounted grains	473	460	338	493	228

Table 5-3: Grain size in 20μm Cu films

Temperature (°C)	200	250	300	350	400	415	450	500	600
Average grain size (μm)	0.39	0.48	0.53	0.64	1.3	1.1	4.8	7.1	12.7
Number of accounted grains	124	185	147	122	95	111	126	211	119
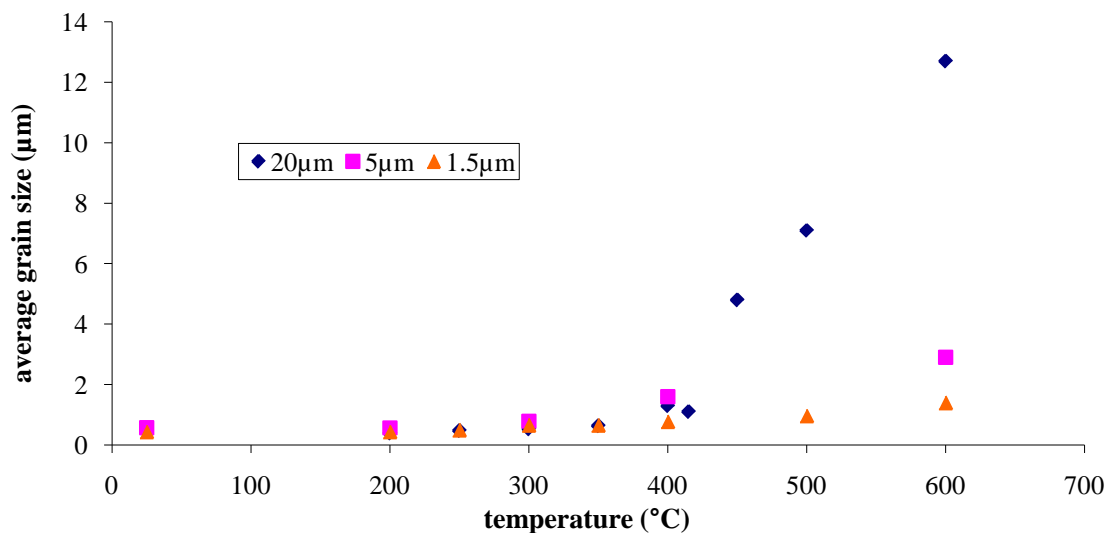
Figure 5.27: Average grain size of electroplated Cu films with the thicknesses of 1.5, 5, and 20μm after annealing cycles.

5.2.3   Surface roughness evolution

Typically, surface roughness represents the topography of a surface. It is usually quantified by the vertical deviations of a real surface from its ideal flat form. If these deviations are small, the surface is smooth, and vice versa. Since surface roughness reflects film microstructure, it is therefore closely related to the grain size of a film. Literally, grain size increases alongside the increasing surface roughness. In our measurement, a 0.5mm x 0.5mm area on the Cu film surface is selected for an analysis of roughness using a digital holography microscope. Each data point presented is the average value of 15 individual measurements taken over the same selected area. Finally, the surface roughness of 5, 15 and 20µm thick electroplated Cu films under different annealing temperatures is determined. There are many different roughness parameters in use [36]. Here, the maximum height of the surface (St) is used to represent surface roughness, as shown in Figure 5.28. The other common parameters of surface roughness, the average of absolute values (Sa) and the root mean squared values (Sq), are plotted in Figure 5.29 and Figure 5.30.
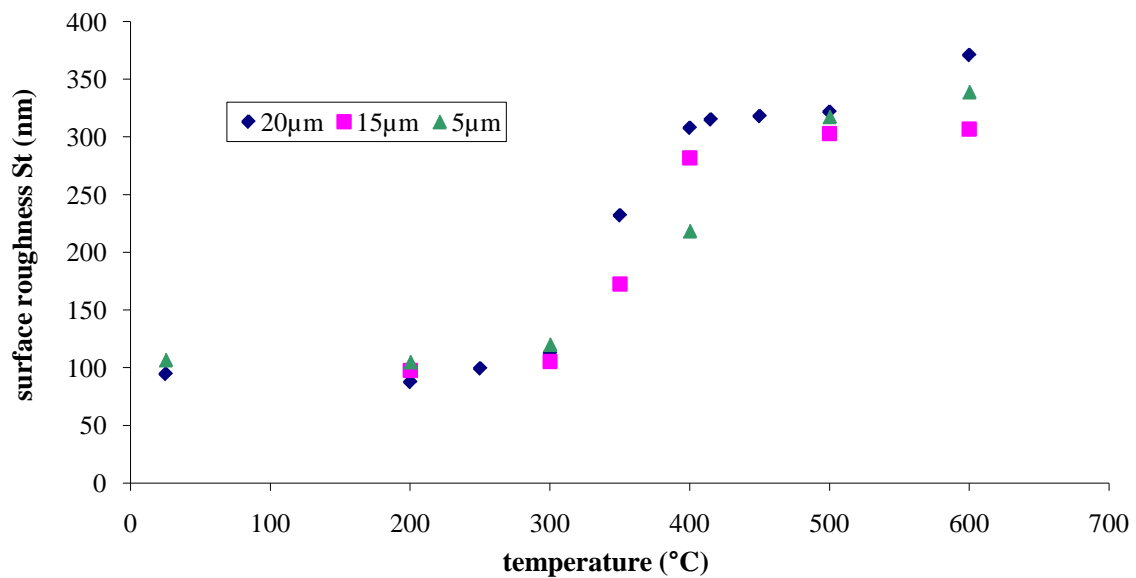
Figure 5.28: Surface roughness St of 5, 15, and 20µm thick electroplated Cu films with different annealing temperatures.
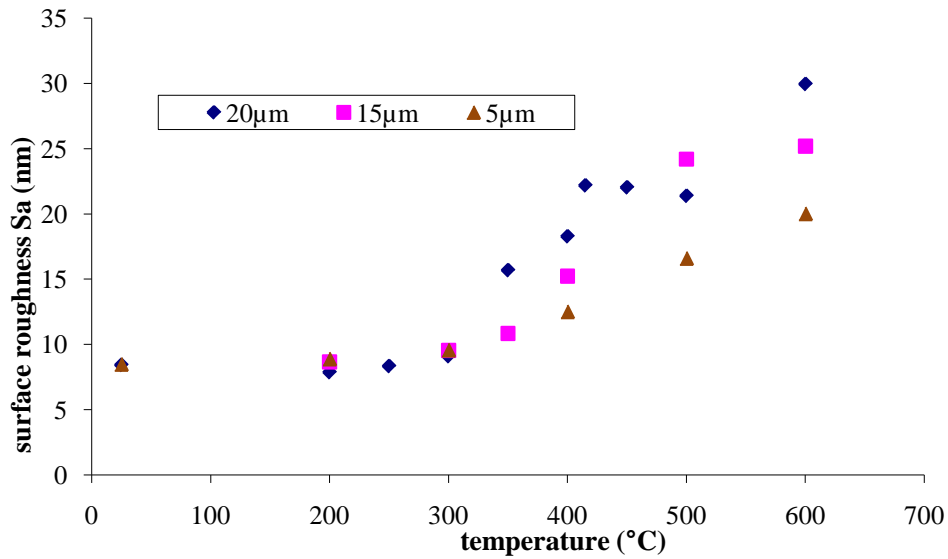
Figure 5.29: Surface roughness Sa of 5, 15, and 20μm thick electroplated Cu films with different annealing temperatures.
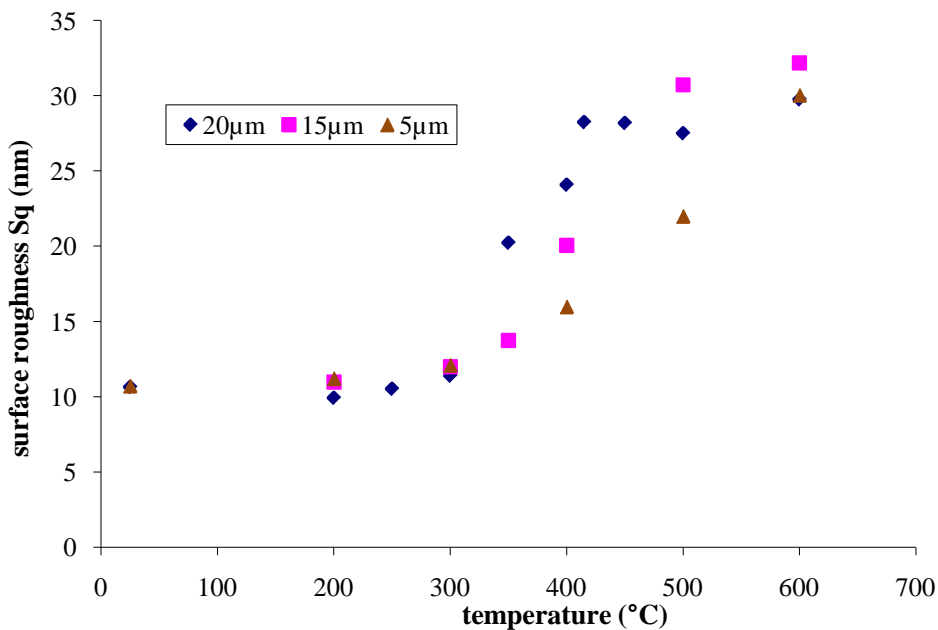
Figure 5.30: Surface roughness Sq of 5, 15, and 20μm thick electroplated Cu films with different annealing temperatures.

In the above figures, it is observed that the surface roughness remains constant and almost equal for all the films until 300°C. Afterwards, surface roughness increases dramatically up to 400°C. Towards the end, surface roughness slightly shows a plateau. The whole tendency of surface roughness development is consistent with the evolution of the grain size in Figure 5.27.

6 Discussion

The dominant mechanisms which are responsible for the stress evolution of electroplated Cu films at room temperature are discussed in this chapter. Furthermore, in order to verify the proposed competing mechanisms, existing models have been implemented and improved for the simulation. The analytical modelling results agree well to experimental data. In the second part of this chapter, the mechanical properties of Cu films at elevated temperatures have been analysed and the possible mechanisms which may drive this stress evolution are described.

6.1 Stress evolution of electroplated Cu films at room temperature

Two different film thickness regimes are identified from the stress-time curves in Figure 5.3. Therefore, both regimes will be discussed and possible mechanisms for the different behaviours will be proposed.

The continuous decrease of stress in thin Cu films (1.5μm–5μm) in Figure cannot be directly explained by grain growth. It is speculated that dislocation plasticity causes stress reduction, as outlined below. As the initial stress is relatively high for thin Cu films, dislocation glide can be activated immediately after deposition and becomes increasingly easier due to grain growth. Stress decrease terminates when the flow stress of the final microstructure, which is film-thickness dependent, has been reached. The stress evolution of thick Cu films (8μm–20μm) is more complex, as shown in Figure 5.2. As the initial stress is relatively low and the grain size is small, dislocation glide cannot be activated immediately after deposition. This correlates well with FIB images (Figure 5.11), which implies that there are no distinct microstructure changes during the first 120 minutes after deposition. Then grain growth starts causing a stress increase after about 200 minutes' incubation phase for the 8μm–20μm thick electroplated Cu films. Grain growth leads to an annihilation of excess volume by reducing the amount of grain boundaries and this induces film shrinkage. This gives rise to tensile stress if the film remains bonded to the substrate. As shown in Figure 5.9–5.11, grain growth clearly occurs during self-annealing. The coarsening starts with the growth of a few grains which consume the surrounding fine-grained matrix until the large grains meet and the fine-grained matrix is completely consumed. Along with grain growth, the tensile film stress increases until it becomes high enough to activate plasticity yielding. As a consequence, both grain growth and plasticity superimpose during stress evolution. The global stress decreases when the effect of dislocation plasticity becomes more prominent than that of grain growth. This is the case for 8μm and 10μm thick Cu films. For 15

and 20μm thick films the peak stresses are so low that dislocation glide and grain growth counterbalance each other. One should be aware that grain growth also happens for the 1.5–5μm Cu films. However, no stress increase is observed during room-temperature annealing since the initial stress is so high that relaxation by dislocation plasticity is more prominent than the stress increase induced by grain growth.
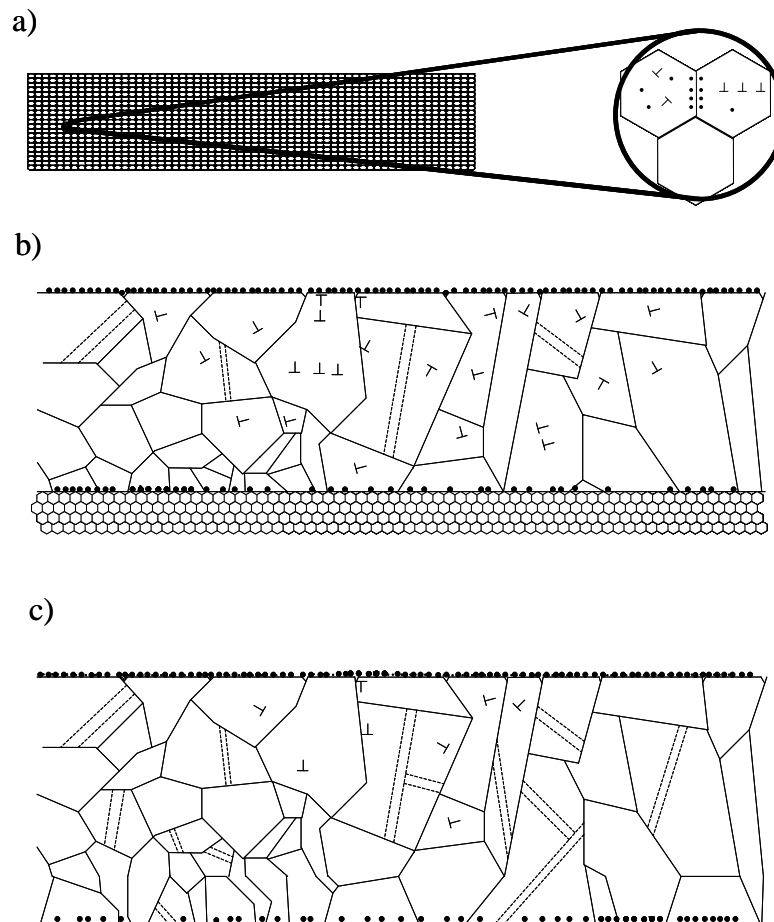
Figure 6.1: Illustration of the microstructure evolution. Dashed lines indicate twins. a) Only fine grains exist in the film after deposition, coupled with a high density of impurities and dislocations. Impurities pin at the grain boundaries; b) Impurities segregate to the film surface and/or film/substrate interface, thus releasing the grain boundaries. Grain growth starts and finally reaches the film/substrate interface region. Meanwhile, dislocation glide can be activated; c) Grain growth terminates. Dislocation density is reduced because dislocations glide across the grains and are incorporated into the grain boundaries.

Figure 6.1 illustrates these processes. The as-deposited films are defect rich as a result of the low deposition temperature process and Cl, S and C impurities [135] coming from the electrolyte bath. The incubation time may be caused by the segregation of impurities via the grain boundaries to the film surface and/or film/substrate interface as sketched in Figure 6.1a and Figure 6.1b. Then, Ostwald ripening [104, 147] can set in, with grain growth starting at grains where grain boundaries are released first by surface and interface segregation of impurities

(Figure 6.1a–Figure 6.1c). It implies that the stress itself is not the only driving force for self-annealing. Otherwise the thicker film would not anneal so rapidly. The driving force for room-temperature grain growth originates from the minimisation of the total energy of the system. In the existing literature, a large variety of energies, such as strain energy, grain boundary energy, surface/interface energy, dislocation energy and stacking faults energy are assumed to be involved in this process [104, 132, 134, 140, 144, 147]. For example, Harper [104] presented a model which is based on grain boundary energy in the fine-grained as-deposited films providing the underlying energy density which drives abnormal grain growth. Weihnacht [132] calculated the energy gain per unit volume due to the annihilation of lattice defects such as grain boundaries, dislocations, and vacancies in Cu metal and identified the ground boundary energy as the decisive driving force of self-annealing. Lee [144] also demonstrated that electroplating produces a large amount of intrinsic stress induced by the formation of dislocation loops and increases the total energy stored in Cu films. Detavernier [147] suggested that apart from the grain boundary energy, other possible effects related to the surface energy, strain energy, and especially dislocation energy also contribute to the driving mechanism of self-annealing The existence of a high density of defects, mostly impurities, dislocations and grain boundaries introduced by room-temperature electroplating, are considered to be the main sources for large amounts of energy stored in the as-deposited fine grains of electroplated Cu films [132, 140, 144].

It is believed that, due to the shorter total deposition time, a higher defect density for thinner films evolves, leading to the higher initial stress when compared to thicker films where some of the defects are already annihilated during the longer deposition time. This could explain why the initial stress decreases with increasing film thickness, i.e. the deposition time. Moreover, the "zipping" process which refers to the coalescence of grain boundaries could also be responsible for the film thickness dependence of the initial stress. It can be speculated that the grain size increases slightly with deposition thickness, leading to lower initial film stresses by grain boundary "stretching" for thicker films. However, due to the resolution limit of FIB imaging (~50nm in our case), possible grain size difference for different film thicknesses could not be resolved. The grain size evolution starts with a small fraction of grains which grow with time, while other grains start to grow at a later stage, leading to a bimodal grain size distribution.

The sheet resistance is determined by electron scattering at defects in the film such as impurities, dislocations and grain boundaries. The annihilation of defects reduces the sheet resistance. Similar to stress evolution, different regimes are observed and can be explained by the same mechanisms. During the first ~400min, the sheet resistance decreases slightly (<1%), because impurity scattering is reduced by diffusion and coalescence of impurities at grain boundaries (see Figure 6.1a). Segregation of impurities to the surface and interface unpins the

grain boundaries leading to grain growth (see Figure 6.1b), which correlates well to the regime II in Figure 5.6 that shows a dramatic decrease of normalised sheet resistance caused by the loss of electron scattering sources (i.e. grain boundaries). During this transient regime a size effect is observed. The transient time depends on the film thickness and increases in time for thinner films. This becomes especially obvious for the 1.5μm and 3μm thick Cu films, while for the 5–20μm thick Cu films the transient time is rather constant. Comparing the evolution of sheet resistance in Figure 5.6 with film stress evolution in Figure 5.3 and the microstructure investigations in Figure 5.9–5.11, it can be concluded that regime II depends on grain growth (annihilation of grain boundaries) and dislocation plasticity (decreasing dislocation density due to the stress evolution and stress relaxation). It is well known that electroplated Cu films can initially have a high dislocation density (10^{12}–10^{13}cm^{-2}) [147], which will decrease with their annihilation at grain boundaries during yielding and grain growth. Finally, the sheet resistance stagnates in regime III where grain growth and stress relaxation have terminated. This demonstrates that grain growth and dislocation glide not only affect the stress evolution during room-temperature annealing but are also reflected in the sheet resistance evolution.

6.2   Modelling of stress evolution at room temperature

To date, most of the research regarding the self-annealing of electroplated Cu films has been devoted to the analysis of mechanisms and kinetics [130, 132-134, 137, 138, 142-144]. Very few publications can be found which present modelling results regarding the self-annealing effect. For example, Stagl [155] developed a phenomenological model to predict the self-annealing kinetics for electroplated Cu thin films with respect to sheet resistivity evolution. It was assumed that recrystallization plays a key role in microstructure evolution. The model can be used to describe the recrystallization fraction of Cu films with a thickness of 0.75-2μm and predict how long it will take to reach recrystallization saturation. However this model does not give any further insights in terms of mechanical aspects of Cu films due to self-annealing. Alternatively, Harper [104] and Lee [156] proposed a model based on Chaudhari's theory which explains the stress evolution due to grain growth, assuming a grain boundary density less than that of a perfect lattice and calculating the strain accumulated in the film by estimating the change in volume associated with the loss of grain boundaries. Using this model, the tensile stress increase can be calculated for electroplated Cu films with a thickness of 1μm, and the results correlate well with experimental observations to a certain extent, which exhibit a continuous increase of biaxial stress in tension and no stress relaxation during self-annealing. However, it was observed in my study that the stress evolution not only shows an increase in tensile direction but also in stress relaxation. Therefore, the proposed grain growth model [104, 156] alone is no longer

sufficient to accurately calculate stress evolution. The stress prediction model needs to be extended, by incorporating a dislocation plasticity model which additionally induces a stress relaxation mechanism. In addition, it is also necessary to incorporate a grain growth rate model in order to directly trace stress evolution over time. The purpose of the following work is to develop a comprehensive numerical model which combines the mechanisms of stress increase and decrease of electroplated Cu films with the stress development rate, paving the way to predict complex stress evolution in a time domain at room temperature.

6.2.1 Tensile stress increase due to the loss of grain boundary volume

The evolution of biaxial stress in the film is associated with microstructure development in the self-annealing. The loss of grain boundary volume during grain growth induces shrinkage of the film volume. If the film remains constrained to the substrate, it causes an increase in tensile stress. Grains can grow against the development of tensile stress during self-annealing because the reduction of grain boundary energy is large enough to overcome the increase in strain energy during grain growth. Harper [104] observed stress evolution of 1μm Cu film, initially starting from -45MPa (compressive stress) and stagnating at near zero, which shows stress increase of 45MPa in tensile direction. Similarly, Lee [144, 156] also investigated the stress evolution of 1μm Cu films but developed this further with respect to electroplating of various current densities. It was found that the initial stress after deposition is ~-40MPa and the overall stress increase in tensile direction ranges from 40-120MPa, depending on the current density of the electroplating. Both Harper and Lee used Chaudhari's theory to model the tensile tress increase of electroplated Cu films during self-annealing.

Chaudhari presented a model which explains the stress development due to grain growth [157]. It calculates the strain in the film by estimating the change in volume associated with the coalescence of grain boundaries. Usually atoms in a crystal lattice are more intensely packed than in grain boundaries. Therefore, the atomic density of a film is increased by the absence of grain boundaries. The shrinkage or densification of the film by elimination of the grain boundaries generates stress in the film. In other words, grain growth is a process of atomic rearrangement which leads to the development of biaxial stress in a film. This stress always develops in the tensile direction. The density of a region containing a grain boundary is usually lower than that of a region containing no boundary. Assuming a grain boundary parameter α ($0 < \alpha < 1$), the boundary region has the same density as the grain if $\alpha = 0$, and a monolayer of atoms is missing in the boundary if $\alpha = 1$. Hereby the grain boundary parameter α can be

defined as $\alpha = \dfrac{w-a}{a}$ in terms of the grain boundary width w and the atomic diameter a. When grain growth begins, two boundaries coalesce to generate a single boundary. Thus, the elastic distortion in the film due to grain growth can be given by $2w - (w+a) = w - a = \alpha a$.

Considering a thin film that has an average grain size L_0 in the as-deposited condition, and assuming the grains grow to final grain size L, the total elastic strain associated with grain growth is:

$$\Delta\varepsilon_{gg} = \frac{\alpha a}{2}\left(\frac{1}{L_0} - \frac{1}{L}\right) \tag{6.1}$$

Then the total change of biaxial stress associated with grain growth is given by

$$\Delta\sigma_{gg} = \frac{E}{1-v}\Delta\varepsilon_{gg} = \frac{E}{(1-v)}\frac{\alpha a}{2}\left(\frac{1}{L_0} - \frac{1}{L}\right) \tag{6.2}$$

where $\Delta\sigma_{gg}$ is the stress increase induced by grain growth, E is the elastic modulus of the film, v is the Poisson's ratio of the film, and a is the bulk atom layer spacing (0.36148nm) [157].

If it is assumed that original and final grain size are 135 and 370nm, respectively, the total stress increase calculated is about 25MPa which is plotted in Figure 6.2. It must be pointed out that the value of the grain boundary parameter α can vary with the deposition conditions, such as electrolyte composition or current density [156]. Moreover, grain growth and coalescence of grain boundaries are not homogeneous over the film, as seen in Figure 5.9–5.11. Based on the actual local values over the film, it is very difficult to set the global α value accurately. In our model, it is assumed that α is the average over transformed and untransformed grains and is estimated as 0.12 based on the best fitting, which is very close to the value of 0.15 found by Cabral [154]. In comparison, Lee [156] and Jiang [158] used 0.55 and 0.68 respectively as the values of the grain boundary parameter.
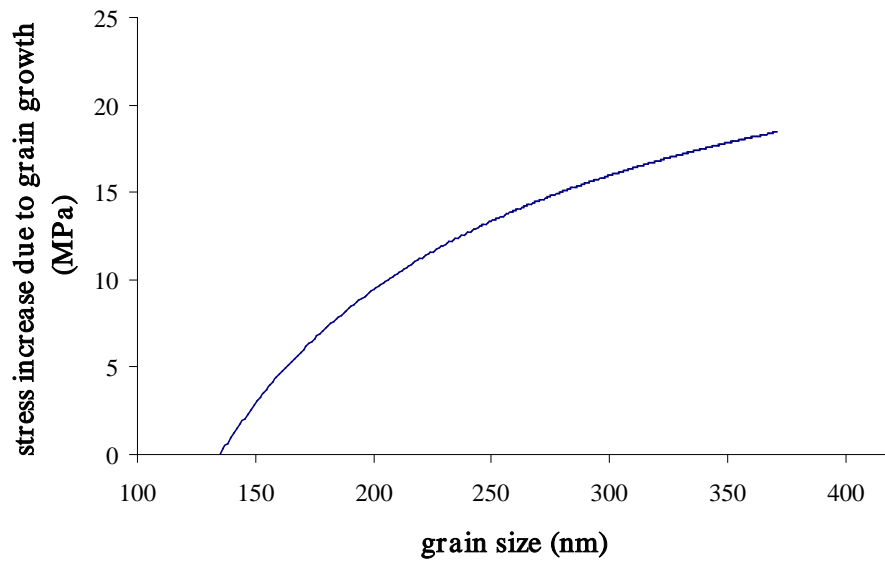
Figure 6.2: Stress increase due to grain growth, calculated by Chaudhari's model. Original grain size is 135nm. (E=121GPa, v=0.33)

6.2.2 Grain growth rate

As Chaudhari's model describes stress evolution as a function of the grain size, it also needs an intermediate model which introduces the grain size development as a function of time elapsed so that the stress evolution can be correlated with time. Doerner and Nix (1988) have successfully developed such a grain growth model to describe the rate of grain size development [64].

There are two major contributions to the total energy E_{total} of a film during grain growth. One is the grain boundary energy E_{gb}, and another is the elastic strain energy W_{el}. Therefore, E_{total} can be written as follows:

$$E_{total} = E_{gb} + W_{el} \tag{6.3}$$

As grain growth proceeds, the grain boundary energy reduces due to the decrease in grain boundary area, whereas elastic strain increases because of accumulated stress and strain in the film.

The grain boundary energy is given by [64, 157]:

$$E_{gb} = \frac{\beta}{L}\gamma \tag{6.4}$$

where γ is the grain boundary energy per unit area, L is the average grain size, and β is the geometrical factor determined by the shape of the grains. β has a value of 2 if grains have a square cross-section, a value of 3 for grains with a circular cross-section and amounts to $4/\sqrt{3}$ for grains with a hexagonal cross-section [64, 157, 159].

The strain energy, which is associated with stress, is given by [64]

$$W_{el} = \frac{1}{2}\sigma_{xx}\varepsilon_{xx} + \frac{1}{2}\sigma_{yy}\varepsilon_{yy} \tag{6.5}$$

Using Hooke's law, this becomes

$$W_{el} = \left(\frac{E}{1-v}\right)\varepsilon^2 = \left(\frac{E}{1-v}\right)\frac{(\alpha a)^2}{4}\left(\frac{1}{L_0} - \frac{1}{L}\right)^2 \tag{6.6}$$

Therefore,

$$E_{total} = \frac{\beta}{L}\gamma + \left(\frac{E}{1-v}\right)\frac{(\alpha a)^2}{4}\left(\frac{1}{L_0} - \frac{1}{L}\right)^2 \tag{6.7}$$

An infinitesimal amount of grain growth dL produces an energy change given by

$$dE = -\frac{\beta\gamma}{L^2}dL - \left(\frac{E}{1-v}\right)\frac{(\alpha a)^2}{2L^2}\left(\frac{1}{L} - \frac{1}{L_0}\right)dL \tag{6.8}$$

This energy variation is equal to that generated by the migration of grain boundaries in response to a driving pressure difference ΔP.

$$dE = -\Delta P\frac{\beta}{L}\frac{dL}{2} \tag{6.9}$$

Combining (5.8) and (5.9) results in,

$$\Delta P = \frac{2\gamma}{L} + \left(\frac{E}{1-v}\right)\frac{(\alpha a)^2}{\beta L}\left(\frac{1}{L} - \frac{1}{L_0}\right) \tag{6.10}$$

According to Shewmon (1969) [160] and Smith (1980) [161], the rate of grain growth as a velocity is given by

$$\frac{dL}{dt} = \frac{D^*\Omega}{kT\delta}\Delta P \tag{6.11}$$

where D^* is the diffusivity given by $D_0\,exp(-E_a\,/\,kT)$, D_0 is the pre-exponential factor for grain boundary diffusion, E_a is the activation energy of grain boundary diffusion, Ω is the atomic

volume, δ is the average jump distance in the grain boundary, k is the Boltzmann constant, and T is the absolute temperature.

Finally, the kinetics of grain growth can be derived by combining (6.10) and (6.11).

$$\frac{dL}{dt} = \frac{D^* \Omega}{kT\delta} \frac{2\gamma}{L} \left(1 - \left(\frac{E}{1-v} \right) \frac{(\alpha a)^2}{2\beta\gamma} \left(\frac{1}{L_0} - \frac{1}{L} \right) \right) \tag{6.12}$$

Equation (6.12) can be solved by using the commercial software Mathematica. In our case, equation (6.12) is a nonlinear ordinary differential equation which can be numerically solved by Mathematica using the command NDSolve, as included in Appendix I. The default method for NDSolve is explicit Runge-Kutta with adaptive step control. As mentioned, grain size can be determined by using a linear intercept method. Based on the FIB images of 3μm and 8μm thick Cu films which were taken at 2hrs, 20hrs and 44hrs, the grain sizes are extracted and plotted as the dots in Figure 6.3. It exhibits that both films undergo a continuous increase in grain size during the whole measurement period. Meanwhile, the simulated curves of 3μm and 8μm thick Cu films are also plotted in Figure 6.3 by the equation (6.12). The grain sizes of 105nn and 135nm obtained from FIB images of 3μm and 8μm thick Cu films are applied as original grain size L_0 in the simulation. As a consequence, the simulated curves converge with the experimental data very well. The following material properties are used in the simulation [54, 104, 157, 162]: $E_a = 1.46 \times 10^{-19}$ J, $D_0 = 3.04 \times 10^{-5}$ m²/s, $\Omega = 1.182 \times 10^{-29}$ m³, $\gamma = 0.625$ J/m2, $\delta = 0.40486$nm, $\beta = 2$.
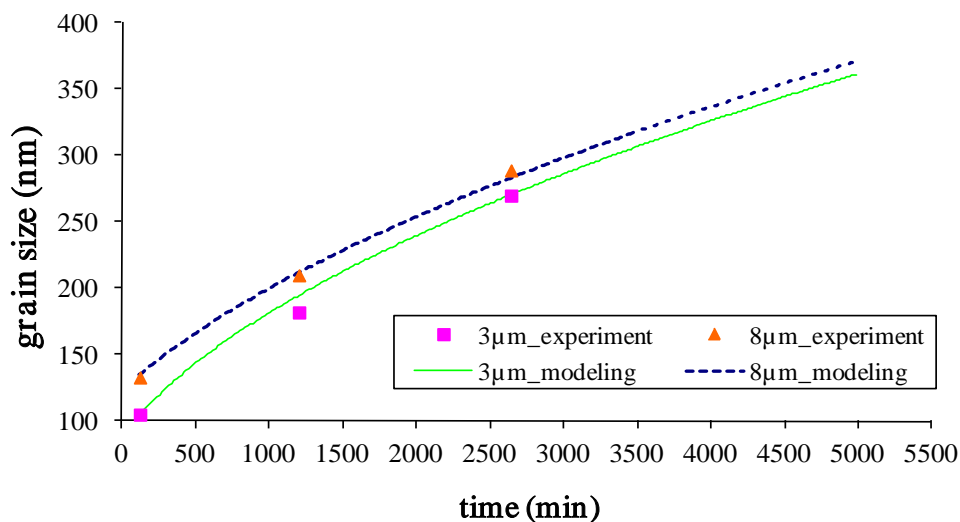
Figure 6.3: Grain size development of 3μm and 8μm thick electroplated Cu films at room temperature.
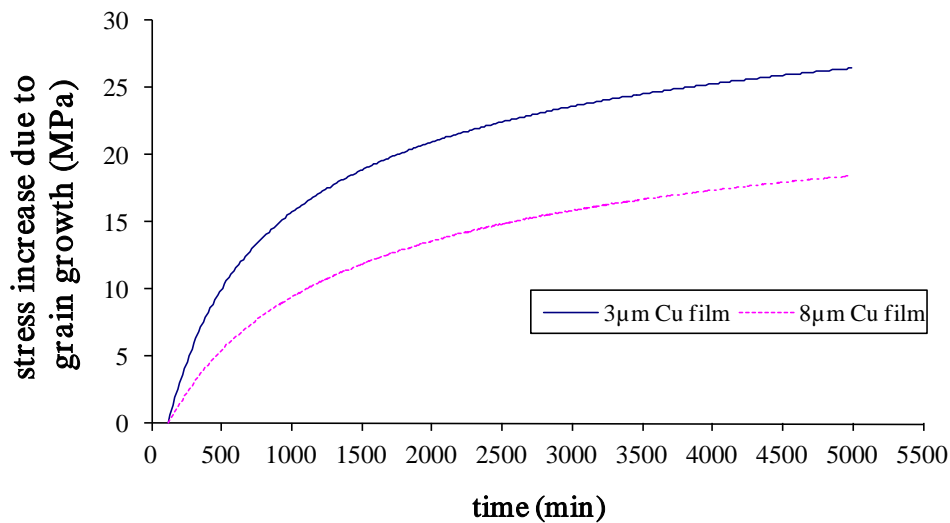
Figure 6.4: Stress increase of 3μm and 8μm electroplated Cu films as a function of time induced by grain boundary loss due to grain growth.

In the experimental investigation of the microstructure evolution of electroplated Cu films, Vas'ko [145] reported that (111) orientated grains can increase their size from 0.1μm after electrodeposition to about 0.25μm after 10 days and to approximately 0.5μm after 25 days. For (200) orientated grains, the size increase is much faster, growing from 0.05μm to about 0.75μm after 10 days and to approximately 2μm after 25 days. Furthermore, Lee [144] found that electroplating conditions play an important role in grain size development. Below the direct current (DC) plating density 20mA/cm², grain size is highly influenced by the current density. The original grain size can increase from 0.1μm to a minimum of 0.2μm and a maximum of 1.4μm within 10 days. Irrespective of current density, when it is above 20mA/cm², the grain size increases from 0.1μm to 1μm in 1 day and to 1.4μm in 10 days. Both grain growth studies above have been done only experimentally and there are no further modeling study about the rate of grain growth. In literatures, there are many two dimensional or three dimensional grain growth models based on the statistical mean field theory, which focus on an interaction between the topological problem of space filling and the surface tension equilibrium [163, 164]. In this case, the Monte Carlo simulation is usually applied to the study of the kinetics of grain growth[165]. However, for the modeling of self-annealing phenomenon the rate equation of grain growth in one dimension is required. Some models proposed by Hillert and Thompson [94, 166] consider the nuclei rate as well as the surface energy and grain boundary energy as the driving force of the mass transport from smaller grains to larger ones especially in the situation of normal grain growth. Differently, self-annealing is an abnormal grain growth or so called secondary grain growth [94]. As discussed in Section 6.1, strain energy in addition to grain boundary/surface

energy must be taken into account. Thus, the rate equation of grain growth proposed by Nix [64] is most suitable model to be implemented for the self-annealing study. To my best knowledge, no other studies of grain size prediction have used theoretical models for the study of the self-annealing of electroplated Cu film except the modelling results which are reported in this thesis.

By the incorporation of the grain growth rate model (6.12) into the grain growth model (6.2), we obtain the direct relationship between the stress increase due to grain growth and time. Thus, stress increase as a function of time can be plotted as in Figure 6.4. The modelled stress curves display for both films the stagnation after ~1500min, though the grain size still continuously dramatically increases, as shown in Figure 6.3. This indicates that the grain growth from fine grains to moderate grains plays the major role in the stress increase. Later on, the grain growth from moderate grains to coarse grains only plays a minor role in stress increase. As a result, it shows clearly that stress increase due to grain growth is film thickness/grain size-dependent. 3μm thick Cu films have a stress increase of ~27MPa compared to ~18MPa in 8μm thick films. This is due to the fact that original grain size is smaller in thinner films. As the amount of stress increase is mainly determined by fine grains, a smaller original grain size will result in a larger stress increase.

6.2.3   Grain boundary strengthening due to dislocation plasticity

The initial stress of electroplated Cu films observed by experiments after deposition can be positive or negative, which refers to tensile or compressive stress, respectively. It is reasonable to assume that initial stress is determined by the deposition method, current density, substrate condition and electrolyte composition. Thus, initial stress after deposition can vary between tensile and compressive stress. It was observed by Harper and Lee [104, 156] that for 1μm Cu film, only compressive stress is initiated and stress continuously increases. In contrast, it was found from Brongersma, Lagrange and Teh's study [140, 141] that, for 0.5-3μm Cu films, the initial stress was tensile, and stress evolution exhibits a continuous decrease. In the study by Harper and Lee, the mechanisms which are responsible for stress decrease can be shielded by the effect of grain growth. This explains why there are neither experimental observations nor numerical models of stress decrease. It appears that, if stress relaxation is considered, stress evolution cannot be solely linked to microstructural change and the grain growth model alone, which means that the model presented in section 6.2.1 is no longer sufficient to explain stress decrease. As proposed by Lagrange [140] stress relaxation might be intimately correlated with chemical desorption (organic additives) from the film. Similarly, Teh [141] also demonstrated that impurity redistribution could play an important role in stress relaxation of Cu films. To

summarise, based on previous research, the stress decrease observed in the self-annealing of Cu films can be induced by defect release/redistribution mechanisms. Unfortunately, no numerical models have been proposed by any researchers to interpret the stress decrease in the self-annealing phenomenon until now. This chapter will contribute to addressing this omission by introducing dislocation plasticity theory as one of the defect release/redistribution mechanisms, and implementing the Hall-Petch law into grain size related stress calculations in order to describe and model stress relaxation numerically.

At room temperature, grain boundaries as well as dislocations act as obstacles to dislocation motion. Impeding the dislocation motion will hinder the onset of plasticity and hence increase the yield strength of the film. The dislocation pile-up which determines the stress concentration in grains, relates to the grain diameter and dislocation density. If the grain size is large and dislocation density is high, a greater stress concentration is developed in the grains, and thus the applied stress needed to activate plastic flow in the grains is relatively low, and vice versa. The Hall-Petch law well represents the grain boundary barrier to dislocation motion as a function of grain size [7, 9, 54, 104]. According to the modified Hall-Petch equation the stress decrease due to dislocation motion can be calculated:

$$\Delta\sigma_{gb} = \sigma_L - \sigma_{L_0} = K\left(\frac{1}{\sqrt{L}} - \frac{1}{\sqrt{L_0}}\right)$$ (6.13)

where $\Delta\sigma_{gb}$ is the stress change due to dislocation glide, σ_L and σ_{L_0} are the flow stress of the film in the case of the grain size of L and L_0, respectively, and K is the Hall-Petch coefficient.

If the grain growth rate model (6.12) is incorporated into the Hall-Petch equation (6.13), the direct relationship between stress decrease by dislocation glide and time is obtained, as shown in Figure 6.5. As discussed, in thick Cu films (8–20μm) dislocation plasticity can only be activated if a certain value of the threshold stress is reached. Therefore, according to the experimental data in Figure 5.3, it is assumed that dislocation plasticity in 8μm thick Cu films is activated when grain growth reaches the grain size of ~190nm after 820min. Similar to the stress increase by grain growth, the stress decrease due to dislocation plasticity is film thickness/grain size-dependent as well. It indicates that thicker films end up with less stress relaxation, which explains why stress decrease becomes less prominent with the increase in film thickness. The stress decrease tendency is even not visible in 20μm thick Cu film, because dislocation plasticity is so marginal that it is easily compensated by grain growth.
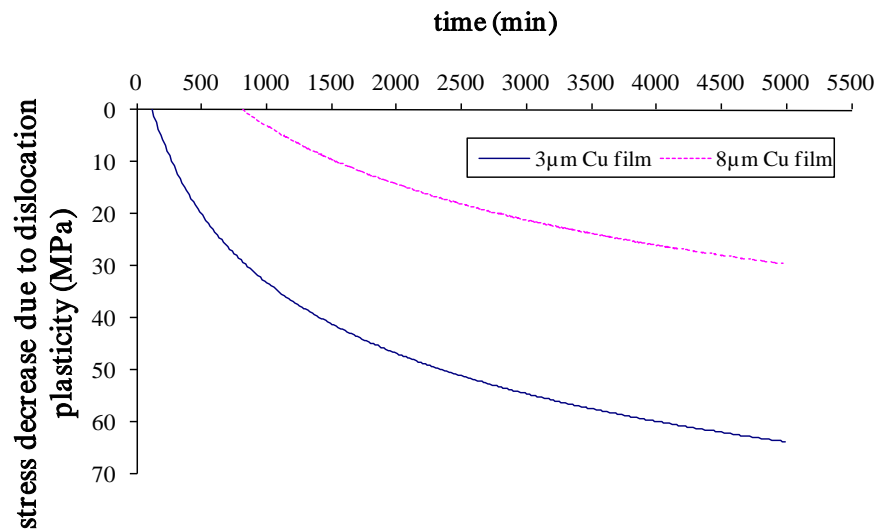
Figure 6.5: Stress decrease of 3μm and 8μm electroplated Cu films induced by grain boundary strengthened dislocation plasticity. Note that for thick Cu films, e.g. 8μm, dislocation motion doesn't start immediately after deposition, but only at 820min after deposition.

The Hall-Petch coefficient K reflects the resistance of grain boundaries to dislocation motion. Typically, a lower value of K refers to less resistance of dislocation motion, and vice versa. In Figure 6.5, the modelled curves are calculated with the K value of 0.0448 MN/m$^{3/2}$, which is ~40% of the well-known Hall-Petch constant 0.112 MN/m$^{3/2}$ for face-centred cubic (FCC) copper [54]. During the abnormal grain growth, subgrains with low angle grain boundaries (<15°) may be strongly involved in the coarse-grained structure, which weakens the blocking of dislocations compared to high-angle grain boundaries (>15°C) [167-169]. Consequently, the Hall-Petch coefficient related to subgrains is typically 1/2 to 1/5 of the well-known value [54]. In order to capture the process of subgrain coarsening, in-situ electron backscatter diffraction (EBSD) or transmission electron microscopy (TEM) during grain growth would be required.

6.2.4 Stress evolution model with competing mechanisms

As aforementioned, the individual mechanism of grain growth or dislocation plasticity does not enable us to interpret the complex stress evolution of electroplated Cu films. Instead, a competing model combining the above two mechanisms, as shown in (6.14), needs to be applied in combination with grain growth rate model (6.12).

$$\sigma = \sigma_0 + \Delta\sigma_{gg} + \Delta\sigma_{gb} \tag{6.14}$$

where σ is the film stress, σ_0 is the as-deposited stress, $\Delta\sigma_{gg}$ and $\Delta\sigma_{gb}$ is the stress change due to grain growth and dislocation glide, respectively.

Figure 6.6 shows the results of two representative numerical calculations in comparison with the corresponding experimental data labelled as dots. The as-deposited stress σ_0 is 60MPa and 23MPa for 3µm and 8µm thick Cu films, respectively. In Figure 6.6, both calculated curves are qualitatively similar to the measured stress plots. As dislocation glide is prominent in the Cu films (1.5–5µm), continuous decrease of stress, which is fully represented by the calculated curve of 3µm thick Cu films, can be obtained by the described model with competing mechanisms. Meanwhile, the curve of 8µm thick Cu films represents well thicker films (8–20µm), which conforms to grain growth and successive dislocation glide mechanisms.

Using the competing model proposed above, stress evolution of thin ($\leq$5µm) and thick (>5µm) electroplated Cu films can be predicted. For thin Cu films, Teh [141] reported a continuous stress decrease in 1-3µm Cu films which is quantitatively close to the findings observed in this study. So far, no other researcher has investigated thick Cu films, and therefore stress evolution always shows a tendency to either increase or decrease. Because of the specially defined film thickness, this study allows us to observe the complex stress evolution of the combined increase and decrease tendency. Stress evolution is film thickness dependent. The initiation of self-annealing is faster and it shows an accelerated transformation when the film thickness increases. The stress fluctuation is lessened when the film thickness decreases.
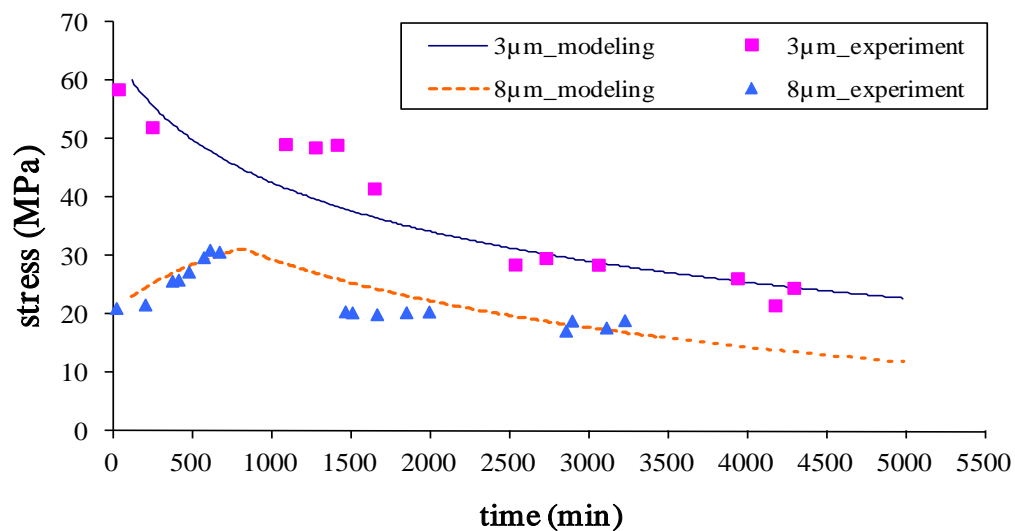
Figure 6.6: Experimental and modelled stress evolution of 3µm and 8µm electroplated Cu films at room temperature.

However, there is a notable limitation of the model which concerns the incubation of grain growth. As observed, particularly in the stress evolution curves of thick Cu films (8–20µm), stress increase does not start immediately after deposition but at ~200min after the deposition. This implies that the onset of grain growth is retarded and all fine grains remain as-deposited undergoing an incubation phase. The incubation of grain growth is not considered in the present

model. Thus, the simulated results only emphasise the stress evolution after the commencement of grain growth, but neglect the stress stabilisation during incubation. Nevertheless, compared to the total evolution time, the incubation time is relatively short.

6.3 Stress evolution and grain size development of electroplated Cu films at elevated temperatures

The stress and microstrcutural evolution of electroplated Cu films becomes more complex at elevated temperatures. The additionally stress contribution from CTE mismatch between Cu films and Si substrate must be considered. At high temperatures, other mechanisms beside dislocation glide might be triggered for stress relaxation. In this chapter, the mechanisms which are responsible for stress evolution in associate with the microstructural development will be analyzed.

6.3.1 Elastic properties of electroplated Cu films

As shown in Figure 5.14, the Cu films are initially in biaxial tension at room temperature. As the wafers are being heated, a linear decrease of tensile stress or an increase of compressive stress is observed. In this linear region, the films deform elastically. The film stress in an elastically deformed thin film can be given by Hooke's law:

$$\sigma_f = (\frac{E}{1-v})_f \varepsilon_{el} = M_f \varepsilon_{el} \qquad (6.15)$$

where σ_f is the film stress, E is Young's modulus of the film, v is the Poisson ratio of the film, ε_{el} is the elastic strain, and M_f is the biaxial modulus of the film.

During a thermal cycle, the elastic strain corresponds to the thermal strain which is applied in the elastic regime due to the difference in thermal expansion between the film and substrate. Hereby, the thermal strain $\varepsilon_{thermal}$ can be given by the following expression:

$$\varepsilon_{thermal} = (\alpha_f - \alpha_s)\Delta T = \Delta\alpha\Delta T \qquad (6.16)$$

where α_f and α_s are the thermal coefficients of the film and the substrate, respectively, and ΔT is the temperature difference between the ramp temperature and room temperature.

By combining (6.15) and (6.16), the slope of the initial portion of the heating curves can be calculated as:

$$\frac{\Delta\sigma}{\Delta T} = M_f \Delta\alpha \qquad\qquad (6.17)$$

If the thermal expansion coefficients of thin film and substrate and the biaxial modulus of the film are known, the theoretic slope of the linear elastic region of the heating curves can be calculated by (6.17). In the case of an isotropic Cu film, where Cu grains are randomly orientated and distributed, the biaxial Young's modulus is about 194GPa, taking the elastic modulus and Poisson ratio as 128GPa and 0.34, respectively. With the difference of thermal coefficients of Cu and silicon, $\alpha_f - \alpha_s = 1.4 \times 10^{-5} K^{-1}$, the theoretical elastic slope is then calculated to be equal to 2.6MPa/K. In contrast, the elastic slopes observed from experiments fall into the range of 2.0-2.5MPa/K, as shown in Figure 5.14–Figure 5.20. In this way, the theoretical elastic slope is slightly larger than the experimental ones obtained. This effect has been studied by some other researchers and several mechanisms have been proposed [170-173]. First of all, the defects in the films such as voids, microcracks, or more complicated grain boundaries, or small-scale inelasticity, will influence the elasticity of the films. Moreover, the inelastic relaxation process induced by grain boundary sliding is also believed to be responsible for the reduced elastic slope value of thin polycrystalline films.
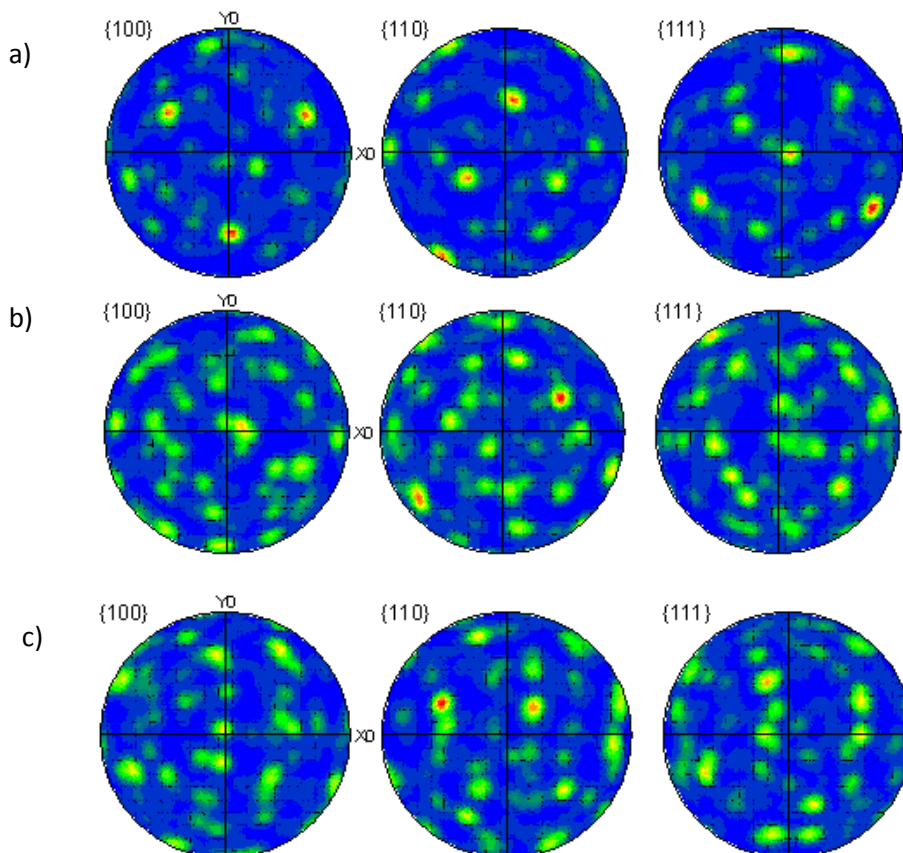
Figure 6.7: Pole figures of electroplated Cu films as-deposited. a) 3μm thick Cu film; b) 8μm Cu film; c) 20μm Cu film.

Furthermore, it is worth noticing that in Figure 5.14–5.20 the experimental elastic slope increases from 2.0 to 2.5MPa/K with the decreasing film thickness from 20 to 1.5μm accordingly. Therefore, it indicates that the thicker film has a slightly lower elastic slope. This behaviour could be attributed to the different presence of enhanced (100) or (111) oriented grains in films.
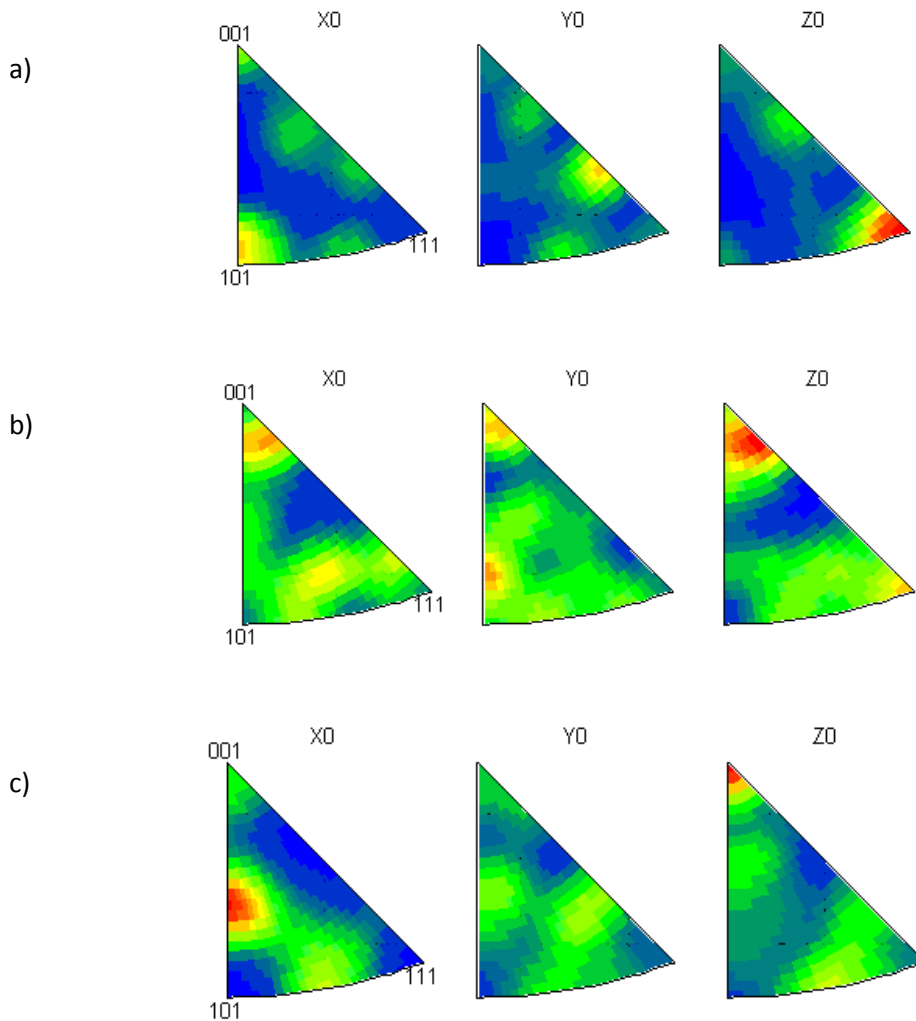
Figure 6.8: Reverse pole figures of electroplated Cu films as-deposited. a) 3μm Cu film; b) 8μm Cu film; c) 20μm Cu film.

A pole figure is normally used to display crystallographic texture. It is a stereographic projection that represents the orientation distribution of crystallographic lattice planes. The pole figures of all three Cu films show no strong texture, as shown in Figure 5.7. Each sample has been scanned in a 10x10μm area. In Figure 6.8, the reverse pole figures of electroplated Cu films as-deposited with the thickness of 3, 8 and 20μm are shown. While the pole figure shows how the specified crystallographic direction of grains are distributed in the sample reference frame, the inverse pole figure shows how the selected direction in the sample reference frame is distributed in the

reference frame of the crystal. The 3µm thick Cu film shows very weak texture in (111) direction, while 20µm thick Cu film shows very weak texture in (100) direction. In the case of (111) textured Cu film, the value of the biaxial modulus (about 261GPa) is considered to be much higher than in the non-textured Cu film, which results in an elastic slope of about 3.7MPa/K. This explains the higher elastic slope observed in more (111) textured Cu film, such as the 1.5µm thick Cu film [156, 174-176]. However, one must note that the texture difference in all electroplated Cu films in this study is trivial. For this reason the elastic slope observed from these experiments is not noticeably different.

6.3.2 Grain growth during thermal annealing

In the elastic region, due to the different CTE between Cu film and Si substrate, an elastic strain (stress) is induced in the film by mechanical bending of the film/substrate system. Film stress acts as the interface counterbalancing force. However, film stress is not only created by elastic deformation. As observed in Figure 5.27, grain growth exists during the whole heating period, though the magnitude of the increase of grain size in the low-temperature region (elastic region) is much smaller than that in the high-temperature region (plastic region). Grain growth increases film stress in tension. Thus, film stress in the elastic region is determined by both grain growth in Cu film and the CTE difference of film and substrate. Nevertheless, the contribution of CTE difference to film stress is the major factor, or even dominant.

After a linear region of elastic deformation, electroplated Cu films behave plastically with further heating above 150°C. There is a significant decrease in compressive stress for all Cu films. Most of the films (1.5–10µm) have such a decreasing tendency continuously until 600°C and show an overall stress decrease of 150–200MPa. On the contrary, Cu films with thicknesses of 15 and 20µm show an overall stress decrease of about 100MPa until 500°C and 400°C, respectively. Afterwards, they exhibit a stress plateau for both films. As clearly seen from FIB analysis, grains grow continuously during the whole heating process. Meanwhile, dislocations which were constrained by fine grains can now slide through coarse grains much more easily. This dislocation plasticity also induces a stress relaxation by dislocation glide. Therefore, these two mechanisms work together on the stress evolution.

As discussed in Chapter 5.2.1, the grain growth model from Chaudhari can well present the stress increase due to the grain boundary loss. By using the data, grain size development obtained by the experiment in Figure 5.27, the stress increase of 1.5 and 20µm electroplated Cu films induced by grain growth can be plotted, as in Figure 6.9 and Figure 6.10. The grain boundary parameter α used is here 0.68, which is larger than that used for self-annealing investigation [104]. It must be noted that, since the grain growth and coalescence is not

homogeneous, the α values will differ if local stress values are used or if the actual grain morphology is included [156]. In the study of thermal annealing, local stress is measured by multiple laser beam technique. In contrast, the global average stress is measured by a capacitive sensor technique in the study of self-annealing. Moreover, the grain size is much larger and Cu films are much more compressively bent, which may also create less density in the grain boundaries and lead to a larger grain boundary parameter.

Other studies about thermal annealing of electroplated Cu films mostly focus on the investigations of mechanisms of plasticity [14, 50, 156, 177-180]. Usually Cu films have been pre-annealed, which totally excludes the microstructure influence on plasticity mechanisms and stress evolution during thermal cycling. Nevertheless, some other researchers who have studied the self-annealing phenomenon of Cu films at room temperature applied Chaudhari's theory to model the tensile stress increase due to grain growth. For instance, Harper [104] observed stress evolution of 1μm Cu film, initially starting from -45MPa (compressive stress) and stagnating at near zero, which shows stress increase of 45MPa in tensile direction. Similarly, Lee [144, 156] also investigated the stress evolution of 1μm Cu films but developed this further with respect to electroplating of various current densities. It was found that the initial stress after deposition is ~-40MPa and the overall stress increase in tensile direction ranges from 40-120MPa, depending on the current density of the electroplating. Different from the other studies, microstructure evolution which is significant for an unannealed Cu film during thermal cycling will be considered and discussed in the following section about plasticity mechanisms.
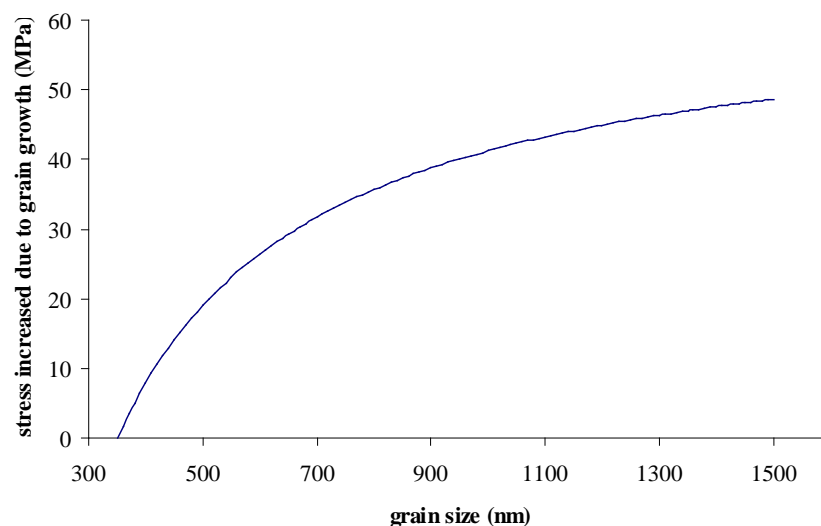
Figure 6.9: Stress increase in tensile direction of 1.5μm electroplated Cu films due to grain boundary loss during grain growth by thermal annealing. Chaudhari's model is applied for the stress calculation. The original and final grain sizes are set to 350nm and 1.5μm based on the experimental data. (E=121GPa, v=0.33, a=0.36148nm)
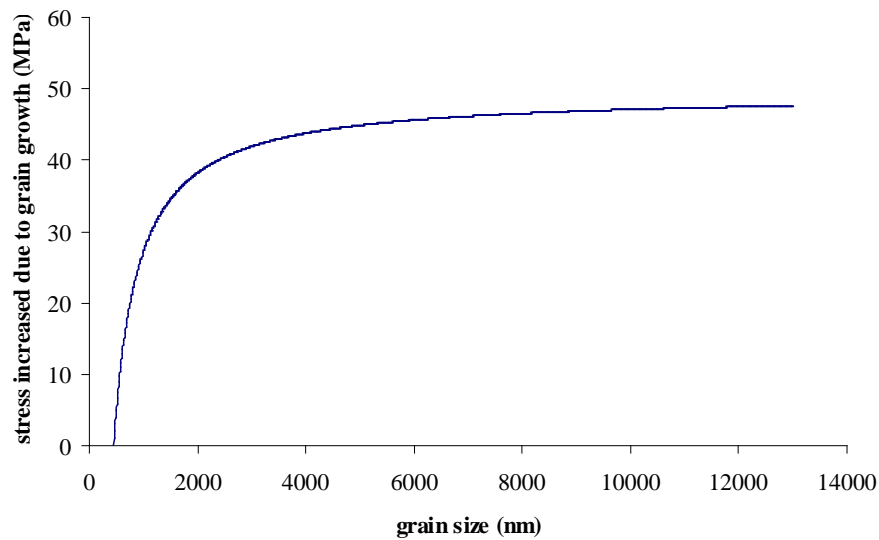
Figure 6.10. Stress increase in tension of 20µm electroplated Cu films due to grain boundary loss by thermal annealing. The original and final grain sizes are set to 450nm and 13µm based on the experimental data.

Another part of compressive stress decrease during heating is caused by dislocation plasticity and can be calculated using the Hall-Petch law, which is plotted in Figure 6.11 and Figure 6.12.
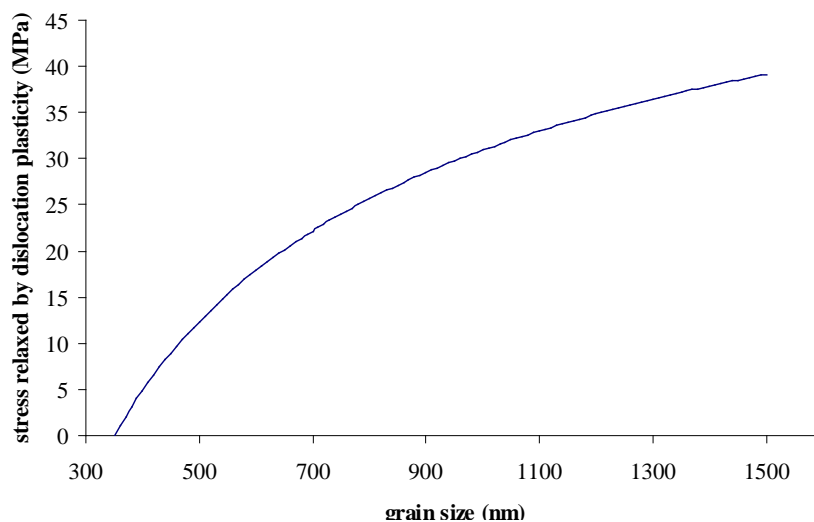
Figure 6.11. Compressive stress relaxation of 1.5µm electroplated Cu films due to dislocation plasticity during grain growth by thermal annealing. The Hall-Petch law is applied for the stress calculation. The original and final grain sizes are set to 350nm and 1.5µm based on the experimental data. (K= 0.0448 MN/m$^{3/2}$)
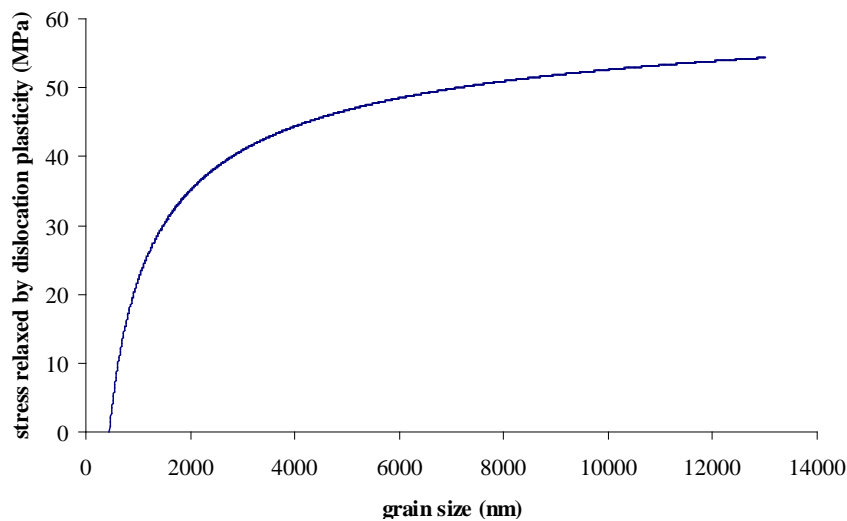
Figure 6.12. Compressive stress relaxation of 20μm electroplated Cu films due to dislocation plasticity during grain growth by thermal annealing. The original and final grain sizes are set to 450nm and 13μm based on the experimental data.

For the 1.5μm Cu film, the compressive stress decrease due to grain growth and dislocation plasticity proceeds continuously during the entire grain growth period. In contrast, for the 20μm Cu film the major stress change happens during the grain growth from original grain size up to about 4–5μm, which falls within the annealing temperature range of 400–450°C, as shown in Figure 5.27. Subsequently, there is no significant stress change, as the stress plateau explicitly reveals. This demonstrates that stress evolution is not only grain growth dependent but also grain size dependent. The most amount of stress change will be accomplished by grain growth up to 4–5μm. Afterwards, the further grain growth will not effect stress evolution in terms of grain boundary loss and dislocation plasticity.

Certainly there are other mechanisms involved, especially diffusion, (e.g. surface diffusion and grain boundary diffusion) which will also have an influence on stress evolution [181, 182]. In order to minimise the total film energy, Cu atoms are more likely to move to the film surface. As a result, film stress will be reduced by relaxing. However, from the FIB images in Figure 5.23-5.26, a Cu oxidation layer which is mainly composed of Cu_2O and Cu_3O_4 is observed and cannot be ignored. Particularly, above the thermal annealing temperature of 400°C, oxidation is even extended into grain boundaries. Therefore, surface diffusion at high temperatures above 400°C is hindered. Another possible path for Cu atom diffusion is grain boundaries. However, with increasing grain size, the grain boundary density is reduced. This means that at a high temperature the grain boundary diffusion is weakened due to the lack of grain boundaries. Usually diffusion should be enhanced by an increase in temperature due to the additional thermal energy but in our case, grain growth and oxidation restrict the diffusion. Therefore

diffusion plays only a minor role in stress evolution compared to grain growth and dislocation plasticity. It has also been demonstrated in the study from Weiss [179] that a passivation layer on a Cu film can hinder the stress relaxation of the film in terms of thermo-mechanical behaviour. Similarly, Thouless [51] showed some experimental evidences that an oxidation surface layer which acts as the passivation capping layer on Cu films suppresses diffusional relaxation mechanisms due to the dense and thermally stable oxide. Therefore, it is a reasonable assumption that surface diffusion doesn't play a role in the diffusional creep. Nevertheless, if atomic diffusion at the film/passviation or/and film/substrate interface is not totally suppressed, a certain amount of stress relaxation can still be realized by the diffusional creep depending on the interfacial (film/passviation and film/substrate) conditions. It was experimentally observed by Weiss that the heating curve of a 0.5μm self-passviating Cu film exhibits a small stress drop (~15MPa) at 320-400°C. Upon a closer inspection in Figures 5.15 and 5.16, it is found that a small stress drop (~20-30MPa) also occur in the heating curves of the 1.5 and 3μm Cu films at 250-300°C and 350-400°C, respectively. The stress drops for different Cu films occurring at different temperatures indicates that the activation energy of interfacial diffusion varies by the conditions of interfaces. If the bonding between a substrate or an oxide layer and a film is strong, it requires higher activation energy for interfacial diffusion. Consequently, the small stress drop can be interpreted by the interfacial diffusion which could open a diffusion path for stress relaxation. However, the investigation for the impact of interface properties on stress evolution of Cu films is not planned within the scope of the thesis.

Compared to the stress-temperature curves shown in Figures 5.14-5.20, Weiss [179] observed additionally in unpassivated Cu films an intriguing characteristic which is a remarkable stress drop in the heating at 250-300°C, which leaded him to derive a constrained-diffusional creep model which is in accordance with the stress relaxation observed at high temperature for pure Cu films. At the end, it was concluded in his work that the thermo-mechanical behaviour of Cu thin films can be described by two deformation mechanisms, thermally activated dislocation glide and constrained diffusional creep. Meantime, a semi-empirical model which combines the two preceding mechanism was derived to predict stress evolution during thermal cycling. The simulation results showed a good agreement with the experimental observations. However, his model doesn't include the microstructure evolution of Cu films during thermal cycling since his samples have been pre-annealed. In my study, grain growth is significant and plays a predominate role in the determination of stress evolution, which is a major difference from the study of Weiss. In another words, the stress evolution investigated in this study is microstructure driven. Hall-Petch law was chosen to model the dislocation plasticity of Cu films for stress relaxation, because it is closely linked with grain size and therefore can directly reflect the effect of microstructure evolution on the stress evolution. As shown in Figure 6.12, the stress

relaxation of 20μm Cu film calculated by Hall-Petch model is about 50MPa. Together with the stress evolution (45MPa) from grain growth in Figure 6.10, it reaches the overall stress evolution of 95MPa, which conforms well to the experimental observation (about 100MPa) in the heating curves in Figure 5.14. Besides that, regarding the shape of heating curves the stress stagnation at about 400°C in Figure 5.14 is also reflected by the calculations shown in Figures 6.10 and 6.12 at the grain size of about 4μm. This means the stress evolution during the heating is contributed by grain growth and dislocation plasticity. Though the grain growth is still proceeding by the further heating above 400°C, the stress remains stagnated which also shows diffusional creep is not valid. For the 1.5μm Cu films shown in Figure 5.15, a continuous stress relaxation is observed which again conforms well to the calculation in Figures 6.9 and 6.11 where stress evolution induced by grain growth and dislocation plasticity is constantly developing. Therefore, it can be concluded that the thermo-mechanical behaviour of Cu films in this study is dominated by the mechanisms of grain growth and dislocation plasticity. Accordingly, the Chaudhari model and Hall-Petch law can well predict and interpret the stress evolution of these Cu films. For further work, it is suggested to incorporate the Chaudhari model and Hall-Petch into a constitutive equation which can be directly applied to simulate stress evolution during thermal cycling

6.3.3   Residual stress after thermal annealing

Residual stress is the stress that remains in the film after the thermal annealing cycle. Residual stress is caused by a variety of mechanisms, including microstructure evolution and plastic deformation. In order to analyse the residual stress, it is essential to understand the sources that may determine the stress. As observed in Figure 5.23–5.26, grain growth occurs during almost the whole annealing process. Due to the volume loss of grain boundaries, the film stress will increase in the tensile direction if the film still bonds firmly on the substrate. Thus, residual tensile stress increases with the increasing annealing temperature as grain growth proceeds further. Secondly, dislocation plasticity will also play an important role in determining the residual stress. Dislocation glide/climb can reduce the film stress. Based on the Hall-Petch law, the larger grain size makes the dislocation glide more easily. Last but not least, the diffusion must be taken into account. In this case, grain boundary and surface are the main paths for atomic diffusion. Thus, grain boundary and surface diffusion are the dominant mechanisms which are responsible for stress relaxation, especially at a high temperature range. Due to the observed oxide layer on the Cu films in Figure 5.23–5.26, especially with the thermal cycles up to

500°C and 600°C, surface diffusion will be mostly hindered as the diffusion path is blocked by the oxide.

a)
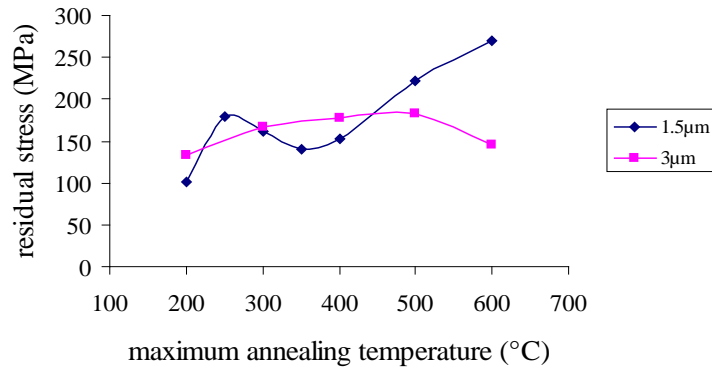
b)
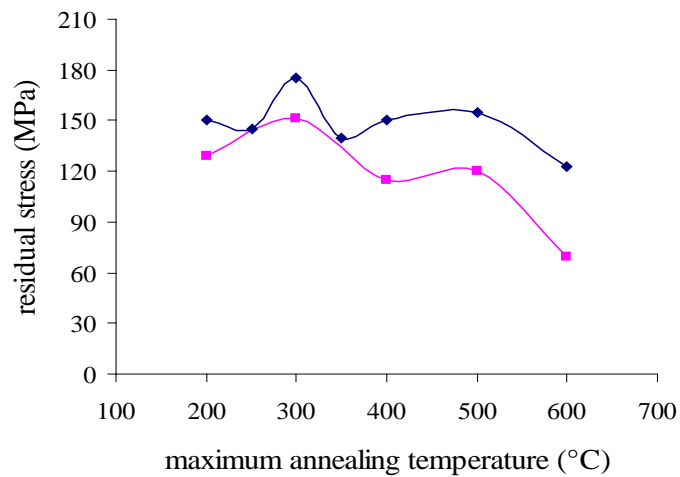
c)
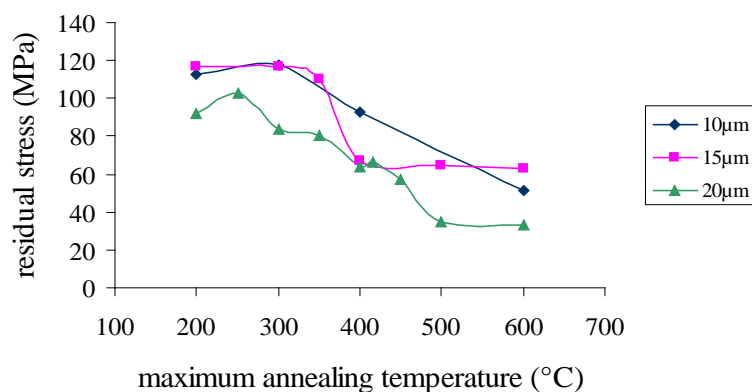
Figure 6.13: Residual stress as a function of maximum annealing temperature for electroplated Cu films with different thicknesses. The residual stress has a different tendency in a), b) and c), which indicates three different mechanisms.

Figure 6.13 summarises the residual stresses of all the investigated Cu films with different thicknesses after each thermal cycle by different maximum annealing temperatures. However, it is not easy to analyse the residual stress tendency as a function of annealing temperatures, as the residual stress of each film develops quite differently. Therefore, the plots of residual stress are divided into 3 different sub-figures a), b) and c) based on the criteria of a similar tendency of residual stress, which reflects the dominant mechanism which determines the residual stress.

For the 1.5μm thick Cu film, residual stress generally increases by increasing the maximum annealing temperature, though from 250–350°C the residual stress is slightly decreased. By increasing the temperature, grains continuously grow, leading to the densification of the Cu film. This causes an increased tensile stress in the film, which explains the general increasing tendency of residual stress of 1.5μm Cu film. Nevertheless, stress decrease still occurs. This indicates that dislocation glide or diffusion must be effective as stress relaxation mechanisms. As in the low temperature range (250–350°C) diffusion cannot be effectively activated, dislocation glide is the major mechanism for the stress decrease. Similarly to the 3μm thick Cu film, the main tendency of residual stress increases with increased maximum annealing temperature. However, a stress decrease is observed for the 3μm thick Cu film at a high temperature above 500°C. As explained before, residual stress increase is induced by grain growth. At a low temperature range, stress decrease due to dislocation glide is compensated by stress increase due to grain boundary loss. Thus, stress decrease in this temperature range is not observed. By further heating, grain boundary/interfacial diffusion becomes more and more significant, which leads to stress relaxation at a high temperature range.

For 5μm and 8μm Cu films, residual stress first increases until 300°C and then decreases until 350°C and 400°C, respectively. Subsequently, it increases again until 500°C and then decreases. This hump tendency of residual stress shows more complicated competing mechanisms. The first increase of residual stress indicates that grain growth is the dominant mechanism that determines residual stress. Due the loss of grain boundaries during grain growth, tensile stress is accumulated. Thus, a higher residual stress can be expected. The subsequent decrease in residual stress is then again the effect of dislocation glide. Both during the heating and cooling process of temperature cycles below 400°C, the dislocation plasticity is triggered to be the dominant mechanism which is responsible for stress relaxation. The residual stress is therefore reduced by dislocation glide. The further heating up to 500°C generates more tensile stress, because the tensile stress increase caused by grain growth is beyond the stress relaxation induced by dislocation glide. The completing between two mechanisms results in a further increase of residual stress. Above 500°C, grain boundary/interfacial diffusion becomes more significant which reduces the residual stress at the end.

For 10, 15, and 20μm thick Cu films, dislocation glide and grain boundary diffusion account for the determination of residual stress. Therefore, the residual stress generally shows a decreasing tendency. Due to the large grain size at high temperatures, the lack of grain boundaries or the reduction of grain boundary density also weakens grain boundary diffusion. Thus, the decrease of residual stress is no longer that significant at a high temperature range.

From the experimental data plot of the residual stress of Cu films with various thicknesses and annealing temperatures, it can be shown that the determination of residual stress is complex. Several mechanisms are involved during thermal annealing processes and contribute differently to the stress change at each temperature stage. Nevertheless, the tendency of residual stress can be differentiated according to film thickness, which actually controls the grain size development. If the film thickness is small, residual stress is driven by grain growth. If the film thickness is medium, grain growth, dislocation glide and diffusion dominate the stress change alternately. If it is a thick film, dislocation glide and diffusion are the mechanisms responsible for determining the residual stress.

7 Summary and conclusions

The stress involved in electroplated Cu films plays an important role in the reliability of chip components in semiconductor industry. The persistent trend towards the miniaturisation of devices creates new challenges to enhance the stable performance of the complex layered structure of thin films in application. Thus, to gain a basic understanding of thin films in terms of mechanical and thermo-mechanical properties has become increasingly important. Copper metallisation is used more and more frequently in power devices due to its advantages over conventional aluminium. The demand for increased power density in devices results in the increase of the film thickness of power metallisation, for example, Cu. On the other hand, thick Cu metallisation can be also used as a heat sink for dissipating the heat more effectively. Therefore the thickness of Cu metallisation has been dramatically increased from a few micrometres in the past to tenths of micrometres. The goal of this dissertation is to investigate the mechanical and thermo-mechanical properties of electroplated Cu films in order to address these academic and industrial interests.

Prior to the theoretical analysis of the material properties of Cu films it was essential to set up an appropriate measurement apparatus as a first step in order to acquire accurate mechanical data of Cu films. The multiple laser technique was chosen as our mechanical characterisation method. Based on that, a novel apparatus for measuring the local stress of thin films by an array of parallel laser beams has been developed. The measurement can be effectively performed not only at room temperature but also at elevated temperatures, as well as under cryo-conditions. The evaluation tests demonstrate that the vibrational noise can be reduced more than 10 times by using an array of parallel laser beams compared to a single laser beam scanning. As a result, the resolution of curvature measurements is greatly improved. Moreover, due to the fast data acquisition (<30ms) the local stress measurement during the rapid thermal processing becomes reliable, from which the study of time-dependent material properties will benefit. Additionally, the evaluation tests also prove that the new insights into the materials' behaviours and thin film properties can be explored by the effective in-situ sample cleaning.

A series of experiments were carried out in order to investigate the effects of film thickness, film microstructure, and annealing temperature on the elastic-plastic behaviour of electroplated Cu films. Cu films with a thickness ranging from 1.5µm to 20µm were fabricated by electroplating. The microstructure was carefully characterised using a variety of microscopic techniques, such as FIB, EBSD and TEM. Stress in Cu films was measured either as a function of time at room

temperature or as a function of temperature at elevated temperatures based on a substrate deflection technique. Afterwards, the mechanical properties could be compared between Cu films with different thickness, grain size and annealing temperature.

Regarding electroplated Cu films after deposition at room-temperature storage, new insights have been gained into the stress and sheet resistance evolution during self-annealing. In the first ~500min after deposition, the film stress (except 1.5–5µm thick films) and sheet resistance remain rather constant. This is explained by the segregation of impurities towards the grain boundaries. Secondly, grain growth is observed by focused ion beam studies. This is explained by the segregation of impurities towards the film surface and interface unpinning the grain boundaries. Grain growth leads to a decrease in sheet resistance. For thick films the low as-deposited tensile stress increases due to the annihilation of excess volume, while for thin films (due to the already pre-existing high as-deposited tensile stress) grain growth induces yielding and thus a reduction in film stress. Eventually grain growth terminates and stress relaxation by dislocation glide is exhausted. The film stress and sheet resistance stagnate at a certain value which scales with film thickness. The present study reveals that the stress and sheet resistance evolution after deposition of electroplated copper films can be explained by grain growth and grain size-dependent yielding. For applications of electroplated Cu films in devices, thicker films are technologically more suitable as (meta)stable conditions are reached after shorter time periods during room-temperature annealing, while thinner films reveal substantial changes in stress and sheet resistance over longer time periods.

Subsequently, a numerical model with competing mechanisms was developed to simulate the stress evolution of electroplated Cu films at room temperature. The model is based on the mechanisms of grain growth and dislocation plasticity. On the one hand, the stress increase is modelled by the loss of grain boundary volume due to grain growth. On the other hand, dislocation glide is responsible for the stress decrease. The incorporation of the model of grain size development makes it possible to include the time as a parameter in the competing model. The results show an accurate correlation between experimental data and simulated values. To extend the model, the incubation phase of grain growth may be considered. Further, EBSD or TEM for the investigation of subgrains is required in order to determine important model parameters, such as the Hall-Petch coefficient.

As far as the thermo-mechanical properties of electroplated Cu films are concerned, it was observed that the shape of stress-temperature curves varies according to the film thickness. The crystallographic texture does not differ among various film thicknesses. It was found that the film thickness has a negligible effect on the elastic modulus of Cu films. Grain growth is observed continuously during the heating process until 600°C. For Cu films with the same film thickness, a higher annealing temperature results in larger grain size. For Cu films with the different film

thickness and annealing at the same temperature, the final grain size is constrained and determined by film thickness. The significant stress decrease in the compression region during heating is due to the loss of grain boundary induced by grain growth which brings in the increase of film stress in tension. The residual stress after thermal annealing shows a strong size effect. The relation between residual stress and annealing temperature (grain size) is quite film-thickness dependent. Usually the Hall-Petch law maintains that flow stress is higher in Cu films with smaller grain size, but the breakdown of the Hall-Petch law becomes more and more obvious with the decreasing film thickness. Qualitatively, it can be concluded that grain growth, dislocation plasticity and even diffusion alternatively play a dominant role in the determination of residual stress. However, to model quantitatively the residual stress combined with thermal annealing remains a challenge.

8 Outlook

It was demonstrated that grain size, film thickness, storage time and annealing temperature have a significant influence on the elastic-plastic behaviour of electroplated Cu films. In addition to the mechanism identified in this study, there are some other mechanisms which can affect the mechanical properties of thin metal films, which can be further explored in future work.

For example, the experiments in this study show a strong temperature dependence of the flow stress for electroplated Cu films. This can be attributed to thermally activated dislocation glide and diffusional creep. However, it is not clear which mechanism is more dominant at a given temperature range. To better understand this, time-dependent deformations of Cu films should be studied. A series of stress relaxation tests need to be carried out under an iso-thermal condition. In this case, stress is measured continuously at a certain defined temperature over a long time period. Afterwards, the strain rate can be calculated from the experimental data by the stress relaxation rate. From the analysis of strain rate, the dominant plasticity mechanism can be better understood.

Furthermore, although not discussed in this study, the hardening behaviour of thin metal films can also be strongly influenced by impurities or precipitates evolved into film microstructure during the film deposition process. The precipitation strengthening can be investigated by the modification of the microstructure of electroplated Cu films.

Extensive TEM work is also required to further study the action of impurities and dislocation sources in Cu films. Important parameters, such as the impurity and dislocation density as a function of film thickness, are necessary for a quantitative evaluation.

The fatigue behaviour and fracture toughness of thin metal films are also of great practical interest. As a part of a zero defect strategy power devices must survive hundreds of thousands of operation cycles. Therefore, it is crucial to keep all types of metallisation implemented in the power device away from material degradation. High fatigue resistance is thus critical to the development of robust metallisation. The fatigue behaviour of thin metal films can be studied by a pulsed power supply on a defined test chip that contains all the necessary features about metallisation which need to be studied.

Appendix I

Wolfram Mathematica 6.0 code for the calculation of grain growth rate of 3μm and 8μm electroplated Cu films at room temperature

E_m=121×10^9; (*Pa=N/m^2=J/m^3*)(*copper E-modulus*)

v=0.33; (*copper Poisson's ratio*)

a=3.6148×10^{-10}; (*m*) (*Cu atomic distance*)

$\boldsymbol{\alpha}$=0.12 (*grain boundary parameter*)

$\boldsymbol{\gamma}$=0.625; (*J/m^2*) (*copper grain boundary energy per unit area*)

$A=\dfrac{E_m\,(\Delta a)^2}{4(1-v)\gamma}$ (*m*)

K=1.38×10^{-23}; (*J/K) (*Boltzmann constant*)

T = 303; (*K*) (*temperature*)

δ=3.6148×10^{-10}; (*m*) (*average jump distance in a grain boundary*)

ρ=1.182×10-29; (*m^3*) (*atomic volume*)

D_0=3.04×10-5; (*m^2/s*) (*diffusivity constant of a grain boundary*)

E_a=1.46×10-19; (*J*) (*activation energy of grain boundary diffusion*)

$D_g=D_0\ exp(-\dfrac{E_a}{kT})$; (*diffusivity of a grain boundary)

$B=\dfrac{D_g\,\rho\,2\gamma}{kT\,\delta}$; (*m^2/s*)

L_0=105×10^{-9}; (*m*) (3μm Cu film); or L$_0$=135×10^{-9}; (*m*) (8μm Cu film)

solution = NDSolve$\left[\left\{\partial_t L[t] == \dfrac{B}{L[t]}\left(1 - A\left(\dfrac{1}{L_0} - \dfrac{1}{L[t]}\right)\right), L[7200] == L_0\right\}, \{L\}, \{t, 7200, 300000\}\right]$;

Plot $[L[t]/$. solution, $\{t, 7200, 300000\}]$

Appendix II

Intermetallic diffusion at the interfaces of Cu/Ti/SiO$_2$

It was observed by FIB measurements that the interface of Cu/Ti/SiO$_2$ changes during the heating process, as shown in Figure AII.1. After electroplating of Cu films or even heating up to 400℃, the interface is very clear and can be easily distinguished. When heating up to 600℃, the interface becomes vague and hilly. Therefore, it is speculated that inter-diffusion occurs between layers due to the high temperature, which may have impact on the stress status in Cu film. In order to clarify this, transmission electron microscopy (TEM) and energy dispersive X-ray spectroscopy (EDX) have been used for the investigation of intermetallic diffusion.
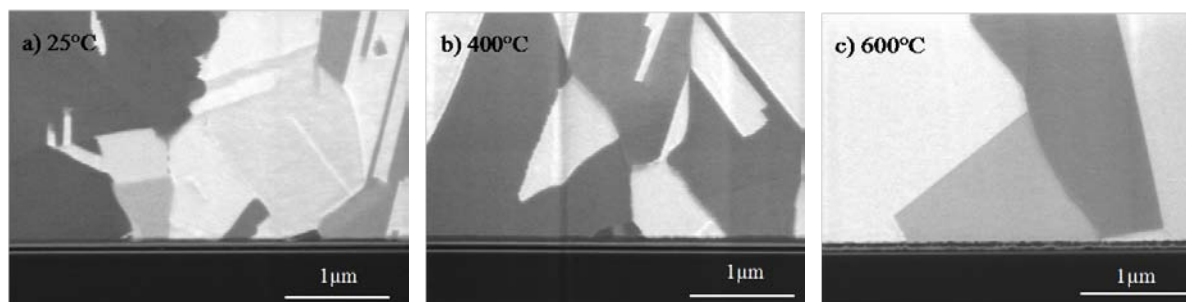
Figure AII.1: FIB images of cross-section view of 5µm Cu film, focusing on the interface part of Cu/Ti/SiO$_2$. a) after electroplating; b) and c) being annealed at 400° and 600℃, respectively.

A Tecnai F20 TEM operated at 200kV was used to investigate the microstructure and the element diffusion in thin films. The TEM specimens have to be thin enough to achieve electron transparency and at the same time maintain mechanical stability. These conditions require complex and time-consuming preparation procedures. In our case, the 20µm thick copper film was reduced to 2µm by mechanical polishing. Prior to TEM analysis, cross-sectional specimens were prepared by the method of FIB Dual Beam in-situ Lift out. A thin electron transparent lamella (50–100nm) was cut out of the sample and transferred onto a Cu grid with a micro-manipulator.

Figure AII.2 a) shows a cross-section view of a 20µm electroplated Cu film annealed at 600℃. On the silicon substrate, a 70–75nm silicon oxide layer is followed by a 39nm thick titanium double layer and the top copper film. The Ti layer is transformed into two different layers by contrast. Scanning transmission electron microscope (STEM) is different from conventional TEM by focusing the electron beam into a narrow spot which is scanned over the sample in a raster. The rastering of the beam across the sample makes it suitable for analysis techniques such as

mapping by energy dispersive X-ray (EDX) spectroscopy. These signals can be obtained simultaneously, allowing the direct correlation of image and quantitative data. EDX is an analytical technique used for the elemental analysis or chemical characterisation of a sample. Its characterisation capabilities rely on the fundamental principle that each element has a unique atomic structure which allows X-rays that are characteristic of an element's atomic structure to be identified uniquely from one another. Usually, EDX systems are integrated with electron microprobes. Based on the STEM image shown in Figure AII.2 b), an intensity profile of the interface can be obtained by an EDX linescan. As shown in Figure AII.2 c), it is not possible to detect copper within the substrate or silicon oxide layer. There may be two reasons for this. Either there is no copper existing within the silicon and the silicon oxide layer, or the concentration of copper is below the detection limit. There is a detectable Cu diffusion into the Ti layer, as the intensity curve of Cu exhibits a peak in the upper Ti layer. The diffusion of Si into the Ti layer can also be noticed, though the effect is even more trivial than that of Cu diffusion. The region of the Cu/Ti interface diffusion is less than 100nm, which is thin compared to the 20μm thickness of Cu film. Therefore it can be concluded that the interface diffusion between the Cu and Ti layer has a negligible impact on the mechanical behaviour of Cu films at high temperatures (>400°C).
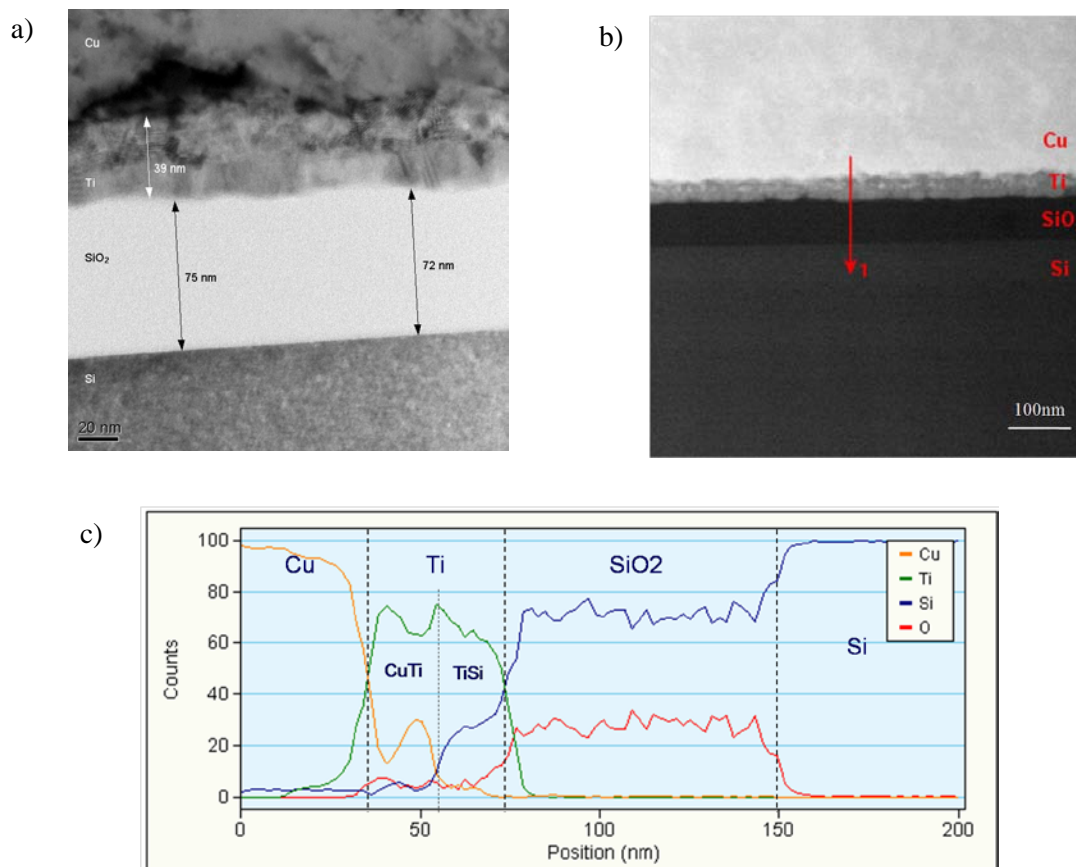
Figure AII.2: a) TEM bright field image for Cu/Ti/SiO$_2$/Si interface, with the magnification of 97K; b) STEM image of the interface; c) Intensity profile of the interface by EDX linescan.

References

[1] S. M. Spearing, "Matrials issues in micrelectromechanical systems (MEMS)," in *Acta Materialia*. vol. 48, 2000, pp. 179-196.

[2] E. Arzt, "Size effects in materials due to microstructural and dimensional constraints: a comparative review," in *Acta materialia*. vol. 46: Elsevier, 1998, pp. 5611-5626.

[3] J. Proost and F. Spaepen, "Evolution of the growth stress, stiffness, and microstructure of alumina thin films during vapor deposition," in *Journal of Applied Physics*. vol. 91, 2002, pp. 204-216.

[4] C. V. Thompson and R. Carel, "Stress and grain growth in thin films," *Journal of the Mechanics and Physics of Solids,* vol. 44, pp. 657-673, 1996.

[5] F. Spaepen, "Interfaces and stresses in thin films," in *Acta Materialia*. vol. 48: Elsevier, 2000, pp. 31-42.

[6] R. P. Vinci and J. J. Vlassak, "Mechanical behavior of thin films," in *Annual Review of Materials Science*. vol. 26, 1996, pp. 431-462.

[7] R. Venkatraman and J. C. Bravman, "Separation of film thickness and grain boundary strengthening effects in Al thin films on Si," in *Journal of Materials Research*. vol. 7, 1992, pp. 2040–2048.

[8] C. V. Thompson, "The yield stress of polycrystalline thin films," in *Journal of Materials Research*. vol. 8, 1993, pp. 237-238.

[9] R. M. Keller, S. P. Baker, and E. Arzt, "Quantitative analysis of strengthening mechanisms in thin Cu films: Effects of film thickness, grain size, and passivation," in *Journal of Materials Research*. vol. 13: Pittsburgh, PA: Published for the Materials Research Society by the American Institute of Physics, c1986-, 1998, pp. 1307-1317.

[10] B. von Blanckenhagen, P. Gumbsch, and E. Arzt, "Dislocation sources and the flow stress of polycrystalline thin metal films," in *Philosophical Magazine*. vol. 83, 2003, pp. 1-8.

[11] L. B. Freund, J. A. Floro, and E. Chason, "Extensions of the Stoney formula for substrate curvature to configurations with thin substrates or large deformations," in *Applied Physics Letters*. vol. 74, 1999, pp. 1987-1989.

[12] J. J. Clement and C. V. Thompson, "Modeling electromigration induced stress evolution in confined metal lines," in *Journal of Applied Physics*. vol. 78: AIP, 2009, pp. 900-904.

[13] C. K. Hu, B. Luther, F. B. Kaufman, J. Hummel, C. Uzoh, and D. J. Pearson, "Copper interconnection integration and reliability," *Thin Solid Films* vol. 262, pp. 84-92, 1995.

[14] M. D. Thouless, J. Gupta, and J. M. E. Harper, "Stress Development and Relaxation in Copper-Films During Thermal Cycling," *Journal of Materials Research,* vol. 8, pp. 1845-1852, Aug 1993.

[15] B. D. Knowlton, J. J. Clement, and C. V. Thompson, "Simulation of the effects of grain structure and grain growth on electromigration and the reliability of interconnects," in *Journal of Applied Physics*. vol. 81-88, 1997, p. 6073.

[16] R. H. Havemann and J. A. Hutchby, "High-performance interconnects: An integration overview," in *Proceedings of the IEEE*. vol. 89, 2001, pp. 586-601.

[17] C. V. Thompson and J. Cho, "A new electromigration testing technique for rapid statistical evaluation of interconnect technology," in *IEEE Electron Device Letters*. vol. 7: IEEE, 2005, pp. 667-668.

[18]   B. C. Valek, N. Tamura, R. Spolenak, W. A. Caldwell, A. A. MacDowell, R. S. Celestre, H. A. Padmore, J. C. Bravman, B. W. Batterman, and W. D. Nix, "Early stage of plastic deformation in thin films undergoing electromigration," in *Journal of Applied Physics*. vol. 94, 2003, pp. 3757-3761.

[19]   B. Zhao and M. Brongo, "Integration of Low-Dielectric Constant Materials in Advanced Aluminum and Copper Interconnects." vol. 564: Warrendale, Pa.; Materials Research Society; 1999, 1999, pp. 485-498.

[20]   B. Zhao, D. Feiler, V. Ramanathan, Q. Z. Liu, M. Brongo, J. Wu, H. Zhang, J. C. Kuei, D. Young, and J. Brown, "A Cu/low-k dual damascene interconnect for high performance and low cost integrated circuits," p. 28, 1998.

[21]   L. Lu, Y. Shen, X. Chen, L. Qian, and K. Lu, "Ultrahigh strength and high electrical conductivity in copper," in *Science*. vol. 304: AAAS, 2004, p. 422.

[22]   D. Edelstein, J. Heidenreich, R. Goldblatt, W. Cote, C. Uzoh, N. Lustig, P. Roper, T. McDevitt, W. Motsiff, and A. Simon, "Full copper wiring in a sub-0.25 μm CMOS ULSI technology," in *Electron Devices Meeting*, 1997, pp. 773-776.

[23]   L. T. Romankiw, "A path: from electroplating through lithographic masks in electronics to LIGA in MEMS," *Electrochimica Acta,* vol. 42, pp. 2985-3005, 1997.

[24]   P. C. Andricacos, C. Uzoh, J. O. Dukovic, J. Horkans, and H. Deligianni, "Damascene copper electroplating for chip interconnections," *IBM JOURNAL OF RESEARCH AND DEVELOPMENT,* vol. 42, pp. 567-574, 1998.

[25]   R. Rosenberg, D. C. Edelstein, C. K. Hu, and K. P. Rodbell, "Copper Metallization for High Performance Silicon Technology," in *Annual Review of Materials Research*. vol. 30, 2000, pp. 229-262.

[26]   G. E. Dieter, *Mechanical Metallurgy*. New York: McGraw-Hill, 1986.

[27]   G. Q. Zhang, W. D. Driel, and X. J. Fan, *Mechanics of Microelectronics*: Springer London, Limited, 2006.

[28]   J. M. Gere and B. J. Goodno, *Mechanics of materials*: Cl-Engineering.

[29]   L. S. Srinath, *Advanced Mechanics Of Solids*: McGraw-Hill Education (India) Pvt Ltd, 2009.

[30]   P. Boch and J. C. Nièpce, *Ceramic materials: processes, properties and applications*: ISTE, 2007.

[31]   S. Huang, *Continuum theory of plasticity*: John Wiley & Sons, 1995.

[32]   R. Hill, "A theory of the yielding and plastic flow of anisotropic metals." vol. 193: The Royal Society, 1948, pp. 281-297.

[33]   A. Nadai, "Plastic Behavior of Metals in the Strain-Hardening Range. Part I," in *Journal of Applied Physics*. vol. 8: AIP, 1937, pp. 205-213.

[34]   C. Kittel and P. McEuen, *Introduction to solid state physics* vol. 119: Wiley New York, 1996.

[35]   R. E. Reed-Hill and R. Abbaschian, *Physical metallurgy principles* vol. 267: Van Nostrand Princeton, N. J, 1964.

[36]   W. D. Callister and D. G. Rethwisch, "Materials science and engineering: an introduction," John Wiley & Sons New York, 1997.

[37]   T. G. Nieh and J. Wadsworth, "Hall-Petch relation in nanocrystalline solids," in *Scripta Metallurgica et Materialia*. vol. 25, 1991, pp. 955-958.

[38]   W. F. Smith and J. Hashemi, *Foundations of materials science and engineering*: McGraw-Hill New York, 2006.

[39]   N. Ohno and J. D. Wang, "Kinematic hardening rules with critical state of dynamic recovery, part I: formulation and basic features for ratchetting behavior," in *International Journal of Plasticity*. vol. 9: Elsevier, 1993, pp. 375-390.

[40]   K. Hashiguchi, "Subloading surface model in unconventional plasticity," in *International Journal of Solids and Structures*. vol. 25: Elsevier, 1989, pp. 917-945.

[41]   T. Hassan and S. Kyriakides, "Ratcheting in cyclic plasticity, part I: uniaxial behavior," in *International Journal of Plasticity*. vol. 8: Elsevier, 1992, pp. 91-116.

[42]   B. K. Chun, J. T. Jinn, and J. K. Lee, "Modeling the Bauschinger effect for sheet metals, part I: theory," in *International Journal of Plasticity*. vol. 18: Elsevier, 2002, pp. 571-595.

[43]   C. O. Frederick and P. J. Armstrong, "A mathematical representation of the multiaxial Bauschinger effect," in *Materials at High Temperatures*. vol. 24: Science Reviews 2000 Ltd, 2007, pp. 1-26.

[44]   M. Abdel-Karim and N. Ohno, "Kinematic hardening model suitable for ratchetting with steady-state," in *International Journal of Plasticity*. vol. 16: Elsevier, 2000, pp. 225-240.

[45]   J. L. Chaboche, "Constitutive equations for cyclic plasticity and cyclic viscoplasticity," in *International Journal of Plasticity*. vol. 5: Elsevier, 1989, pp. 247-302.

[46]   K. C. Valanis, "On the foundations of the endochronic theory of viscoplasticity," in *Archiwum Mechaniki Stosowanej*. vol. 27, 1975, pp. 857-868.

[47]   O. Watanabe and S. N. Atluri, "Internal time, general internal variable, and multi-yield-surface theories of plasticity and creep: a unification of concepts," in *International Journal of Plasticity*. vol. 2: Elsevier, 1986, pp. 37-57.

[48]   H. Okada, H. Rajiyah, and S. N. Atluri, "Non-hyper-singular integral-representations for velocity (displacement) gradients in elastic/plastic solids (small or finite deformations)," in *Computational mechanics*. vol. 4: Springer, 1989, pp. 165-175.

[49]   D. Weiss, "Deformation mechanisms in pure and alloyed copper films," 2000.

[50]   P. A. Flinn, "Measurement and Interpretation of Stress in Copper-Films as a Function of Thermal History," *Journal of Materials Research,* vol. 6, pp. 1498-1501, Jul 1991.

[51]   M. D. Thouless, K. P. Rodbell, and C. Cabral Jr, "Effect of a surface layer on the stress relaxation of thin films," in *Journal of Vacuum Science & Technology A: Vacuum, Surfaces, and Films* vol. 14: AVS, 1996, pp. 2454-2461.

[52]   P. Duval, M. F. Ashby, and I. Anderman, "Rate-controlling processes in the creep of polycrystalline ice," in *Journal of Physical Chemistry*. vol. 87: ACS Publications, 1983, pp. 4066-4074.

[53]   A. S. Helle, K. E. Easterling, and M. F. Ashby, "Hot-isostatic pressing diagrams: new developments," in *Acta Metallurgica*. vol. 33: Elsevier, 1985, pp. 2163-2174.

[54]   T. H. Courtney and T. Hugh, *Mechanical behavior of materials*. New York McGraw-Hill New York, 1990.

[55]   O. Kraft, L. B. Freund, R. Phillips, and E. Arzt, "Dislocation plasticity in thin metal films," in *MRS bulletin*. vol. 27: Materials Research Society, 2002, pp. 30-37.

[56]   G. Dehm, T. J. Balk, H. Edongué, and E. Arzt, "Small-scale plasticity in thin Cu and Al films," in *Microelectronic Engineering*. vol. 70: Elsevier, 2003, pp. 412-424.

[57]   T. J. Balk, G. Dehm, and E. Arzt, "Parallel glide: Unexpected dislocation motion parallel to the substrate in ultrathin copper films," in *Acta Materialia*. vol. 51: Elsevier, 2003, pp. 4471-4485.

[58]   M. T. Péerez-Prado and J. J. Vlassak, "Microstructural evolution in electroplated Cu thin films," in *Scripta Materialia*. vol. 47, 2002, pp. 817-823.

[59]   F. R. Brotzen, "Mechanical testing of thin films," in *International materials reviews* vol. 39, 1994, pp. 24-45.

[60]   O. Kraft and C. A. Volkert, "Mechanical testing of thin films and small structures," in *Advanced Engineering Materials*. vol. 3, 2001, pp. 99-110.

[61]   P. A. Flinn, D. S. Gardner, and W. D. Nix, "Measurement and Interpretation of stress in aluminum-based metallization as a function of thermal history," in *IEEE Transactions on Electron Devices*. vol. 34, 1987, pp. 689-699.

[62]   M. Moske and K. Samwer, "New UHV dilatometer for precise measurement of internal stresses in thin binary alloy films from 20 to 750 K," in *Review of Scientific Instruments*. vol. 59: AIP, 2009, pp. 2012-2017.

[63]   J. Laconte, F. Iker, S. Jorez, N. Andre, J. Proost, T. Pardoen, D. Flandre, and J. P. Raskin, "Thin films stress extraction using micromachined structures and wafer curvature measurements," in *Microelectronic Engineering*. vol. 76: Elsevier, 2004, pp. 219-226.

[64]   M. F. Doerner and W. D. Nix, "Stresses and deformation processes in thin films on substrates," *Critical Reviews in Solid State and Materials Sciences,* vol. 14, pp. 225-268, 1988.

[65]   L. B. Freund and S. Suresh, *Thin Film Materials: Stress, Defect Formation, and Surface Evolution*: Cambridge University Press, 2003.

[66]   W. D. Nix, "Mechanical Properties of Thin Films," *Metallurgical Transactions A,* vol. 20, pp. 2217-2245, 1989.

[67]   G. G. Stoney, "Tension of electro-deposited films," in *Proceedings of the Royal Society of London*. vol. 82, 1909, p. 172.

[68]   C. V. Thompson and R. Carel, "Texture development in polycrystalline thin films," in *Materials Science and Engineering B*. vol. 32: Elsevier, 1995, pp. 211-219.

[69]   K. Mirpuri and J. Szpunar, "Impact of annealing, surface/strain energy and linewidth to line spacing ratio on texture evolution in damascene Cu interconnects," *Materials Characterization,* vol. 54, pp. 107-122, Feb 2005.

[70]   K. Pantleon, J. A. D. Jensen, and M. A. J. Somers, "Interpretation of quantitative crystallographic texture in copper electrodeposits on amorphous substrates," *Journal of the Electrochemical Society,* vol. 151, pp. C45-C51, Jan 2004.

[71]   C. Lingk, M. E. Gross, and W. L. Brown, "Texture development of blanket electroplated copper films," *Journal of Applied Physics,* vol. 87, pp. 2232-2236, Mar 2000.

[72]   B. Hong, C. H. Jiang, and X. J. Wang, "Texture of electroplated copper film under biaxial stress," *Materials Transactions,* vol. 47, pp. 2299-2301, Sep 2006.

[73]   D. N. Lee, "Effect of stacking fault energy on evolution of recrystallization and grain growth textures of metals," in *3rd International Conference on Recrystallization and Grain Growth, ReX and GG III*, Jeju Isl, SOUTH KOREA, 2007, pp. 93-100.

[74]   J. W. Hutchinson, "Plasticity at the micron scale," in *International Journal of Solids and Structures*. vol. 37: Elsevier, 2000, pp. 225-238.

[75]   R. P. Vinci, E. M. Zielinski, and J. C. Bravman, "Thermal strain and stress in copper thin films." vol. 262: Elsevier, 1995, pp. 142-153.

[76]   Y. Huang, H. Gao, W. D. Nix, and J. W. Hutchinson, "Mechanism-based strain gradient plasticity--II. Analysis," in *Journal of Mechanics Physics of Solids*. vol. 48: Elsevier, 2000, pp. 99-128.

[77]   L. Nicola, E. Van der Giessen, and A. Needleman, "Discrete dislocation analysis of size effects in thin films," in *Journal of Applied Physics*. vol. 93: AIP, 2009, pp. 5920-5928.

[78]   A. Needleman and E. Van der Giessen, "Discrete dislocation and continuum descriptions of plastic flow," in *Materials Science and Engineering A*. vol. 309: Elsevier, 2001, pp. 1-13.

[79]   K. W. Schwarz and J. Tersoff, "Interaction of threading and misfit dislocations in a strained epitaxial layer," in *Applied Physics Letters*. vol. 69, 1996, pp. 1220-1222.

[80]   H. Gao, Y. Huang, W. D. Nix, and J. W. Hutchinson, "Mechanism-based strain gradient plasticity-- I. Theory," *Journal of the Mechanics and Physics of Solids,* vol. 47, pp. 1239-1263, 1999.

[81]   R. S. Fertig Iii and S. P. Baker, "Dislocation dynamics simulations of dislocation interactions and stresses in thin films," in *Acta Materialia*. vol. 58: Pergamon, pp. 5206-5218.

[82]   S. Takeuchi, Aregon, A.S., "Steady-state creep of single-phase crystalline matter at high temperature," *Journal of Materials Science,* vol. 11, pp. 1542-1566, 1976.

[83]   M. F. Ashby and H. J. Frost, "Deformation-Mechanism Maps," in *Pergamon press*, 1982.

[84]   R. Spolenak and C. Volkert, "Mechanical properties of electroplated copper thin films," in *Thin Films--Stresses and Mechanical Properties* 1999, pp. 63-68.

[85]   E. O. Hall, "The deformation and ageing of mild steel," in *Proceedings of the Physical Society. Section B*. vol. 64: IOP Publishing, 1951, p. 747.

[86]   N. J. Petch, "The cleavage strength of polycrystalline," in *Journal of Iron Steel Instrument*. vol. 173, 1953, pp. 25–28.

[87]   C. V. Thompson, "Structure evolution during processing of polycrystalline films," in *Annual Review of Materials Science*. vol. 30, 2000, pp. 159-190.

[88]   A. Tzanavaras, G. Young, and S. Gleixner, "The microstructure and grain size of jet electroplated copper films in damascene trench features," *Journal of the Electrochemical Society,* vol. 153, pp. C509-C516, 2006.

[89]   J. M. E. Harper and K. P. Rodbell, "Microstructure control in semiconductor metallization." vol. 15: AVS, 1997, p. 763.

[90]   A. Godfrey and D. A. Hughes, "Physical parameters linking deformation microstructures over a wide range of length scale," *Scripta Materialia,* vol. 51, pp. 831-836, 2004.

[91]   M. H. Shih, C. Y. Yu, P. W. Kao, and C. P. Chang, "Microstructure and flow stress of copper deformed to large plastic strains," *Scripta Materialia,* vol. 45, pp. 793-799, 2001.

[92]   T. Muppidi, D. P. Field, J. E. Sanchez, and C. Woo, "Barrier layer, geometry and alloying effects on the microstructure and texture of electroplated copper thin films and damascene lines," *Thin Solid Films,* vol. 471, pp. 63-70, Jan 2005.

[93]   A. Tzanavaras, G. Young, and S. Gleixner, "The grain size and microstructure of jet-electroplated damascene copper films," *Journal of the Electrochemical Society,* vol. 152, pp. C101-C107, 2005.

[94]   C. V. Thompson, "Grain Growth in Thin Films." vol. 20: Annual Reviews, 1990, pp. 245-268.

[95]   A. A. Volinsky, J. Vella, I. S. Adhihetty, V. Sarihan, L. Mercado, B. H. Yeung, and W. W. Gerberich, "Microstructure and Mechanical Properties of Electroplated Cu Thin Films." vol. 649: Warrendale, Pa.; Materials Research Society; 1999, 2001, pp. 5-5.

[96]   C. Ryu, K. W. Kwon, A. L. S. Loke, H. Lee, T. Nogami, V. M. Dubin, R. A. Kavari, G. W. Ray, and S. S. Wong, "Microstructure and reliability of copper interconnects." vol. 46, 1999, pp. 1113-1120.

[97]   M. Ohring, *The Materials Science of Thin Films* Academic Press, 1992.

[98]   C. J. Simpson and K. T. Aust, "Grain boundary migration," in *Surface Science*. vol. 31: Elsevier, 1972, pp. 479-497.

[99]   W. W. Mullins, "The Effect of Thermal Grooving on Grain Boundary Motion," *Acta Metallurgica,* vol. 6, pp. 414-427, 1958.

[100]   M. Winning, G. Gottstein, and L. S. Shvindlerman, "On the mechanisms of grain boundary migration," in *Acta Materialia*. vol. 50: Elsevier, 2002, pp. 353-363.

[101]   C. M. F. Rae and D. A. Smith, "On the mechanisms of grain boundary migration," in *Philosophical Magazine A*. vol. 41: Taylor & Francis, 1980, pp. 477-492.

[102]   D. A. Smith, "On the Mechanisms of Grain Boundary Migration," in *Materials Science Forum*. vol. 94: Trans Tech Publ, 1992, pp. 221-232.

[103]   H. Gleiter, "The mechanism of grain boundary migration," in *Acta Metallurgica*. vol. 17: Elsevier, 1969, pp. 565-573.

[104]   J. M. E. Harper, C. Cabral Jr, P. C. Andricacos, L. Gignac, I. C. Noyan, K. P. Rodbell, and C. K. Hu, "Mechanisms for microstructure evolution in electroplated copper thin films near room temperature," *Journal of Applied Physics,* vol. 86, pp. 2516-2525, 1999.

[105]   A. Gangulee, "The Structure of Electroplated and Vapor Deposited Copper Films," in *Journal of Applied Physics*. vol. 43: AIP, 2009, pp. 867-873.

[106]   I. V. Tomov, D. S. Stoychev, and I. B. Vitanova, "Recovery and recrystallization of electrodeposited bright copper coatings at room temperature. II. X-ray investigation of primary recrystallization," in *Journal of Applied Electrochemistry*. vol. 15: Springer, 1985, pp. 887-894.

[107]   C. Lingk and M. E. Gross, "Recrystallization kinetics of electroplated Cu in damascene trenches at room temperature," *Journal of Applied Physics,* vol. 84, pp. 5547-5553, Nov 1998.

[108]   G. Schmidt, R. Zelsacher, M. Bar, W. Werner, and B. Winkler, "Semiconductor component and micromechanical structure," Google Patents, 2005.

[109]   L. L. Mishnaevsky Jr and D. Gross, "Deformation and failure in thin films/substrate systems: methods of theoretical analysis," in *Applied Mechanics Reviews*. vol. 58, 2005, p. 338.

[110]   P. A. Flinn and C. Chiang, "X ray diffraction determination of the effect of various passivations on stress in metal films and patterned lines," *Journal of Applied Physics,* vol. 67, pp. 2927-2931, 2009.

[111]   A. Segmüller, J. Angilelo, and S. J. La Placa, "Automatic x-ray diffraction measurement of the lattice curvature of substrate wafers for the determination of linear strain patterns," in *Journal of Applied Physics*. vol. 51, 1980, p. 6224.

[112]   I. C. Noyan and J. B. Cohen, *Residual Stress—Measured by Diffraction and Interpretation*: MRE Springer, 1987.

[113]   P. R. Besser, S. Brennan, and J. C. Bravman, "An x-ray method for direct determination of the strain state and strain relaxation in micron-scale passivated metallization lines during thermal cycling," *Journal of Materials Research,* vol. 9, pp. 13-24, 1994.

[114]   W. M. Kuschke and E. Arzt, "Investigation of the stresses in continuous thin films and patterned lines by x-ray diffraction," *Applied Physics Letters,* vol. 64, pp. 1097-1099, 2009.

[115]   K. S. Chen, T. Y. F. Chen, C. C. Chuang, and I. K. Lin, "Full-field wafer level thin film stress measurement by phase-stepping shadow moiré," in *IEEE Transactions on Components and Packaging* vol. 27, 2004, pp. 594-601.

[116] M. Grédiac, "The use of full-field measurement methods in composite material characterization: interest and limitations," in *Composites Part A*. vol. 35: Elsevier, 2004, pp. 751-761.

[117] D. Chocyk, A. Proszynski, and G. Gladyszewski, "Diffusional creep induced stress relaxation in thin Cu films on silicon," in *12th European Workshop on Materials for Advanced Metallization*, Dresden, GERMANY, 2008, pp. 2179-2182.

[118] A. B. Mann, J. Tapson, D. v. Heerden, A. C. Lewis, D. Josell, and T. P. Weihs, "Apparatus to measure wafer curvature for multilayer systems in a vacuum furnace," in *Review of Scientific Instruments*. vol. 73: AIP, 2002, pp. 1821-1827.

[119] V. Weihnacht, W. Bruckner, and C. M. Schneider, "Apparatus for thin-film stress measurement with integrated four-point bending equipment: Performance and results on Cu films," in *Review of Scientific Instruments*. vol. 71: AIP, 2000, pp. 4479-4482.

[120] E. H. Chason, J. A. Floro, C. H. Seager, and M. B. Sinclair, "Measurement of the curvature of a surface using parallel light beams," Google Patents, 1999.

[121] J. A. Floro and E. Chason, "Curvature-Based Techniques for Real-Time Stress Measurement During Thin-Film Growth," Wiley-Interscience, 2001, p. 191.

[122] R. Huang, C. A. Taylor, S. Himmelsbach, H. Ceric, and T. Detzel, "Apparatus for measuring local stress of metallic films, using an array of parallel laser beams during rapid thermal processing," in *Meas. Sci. Technol.* vol. 21, p. 055702.

[123] B. C. Platt, "History and principles of Shack-Hartmann wavefront sensing," in *Journal of Refractive Surgery*. vol. 17: SLACK INCORPORATED, 2001, pp. 573-577.

[124] W. C. Dash and R. Newman, "Intrinsic optical absorption in single-crystal germanium and silicon at 77 K and 300 K," in *Physical Review*. vol. 99: APS, 1955, pp. 1151-1155.

[125] T. S. Moss, *Optical properties of semi-conductors*: Butterworths Scientific Publications, 1959.

[126] Y. S. Chu, I. K. Robinson, and A. A. Gewirth, "Comparison of aqueous and native oxide formation on Cu (111)," in *The Journal of Chemical Physics*. vol. 110, 1999, p. 5952.

[127] Y. Z. Hu, R. Sharangpani, and S. P. Tay, "In situ rapid thermal oxidation and reduction of copper thin films and their applications in ultralarge scale integration," in *Journal of the Electrochemical Society*. vol. 148, 2001, p. G669.

[128] J. H. Han and M. T. A. Saif, "In situ microtensile stage for electromechanical characterization of nanoscale freestanding films," in *Review of Scientific Instruments*. vol. 77, 2006, p. 045102.

[129] S. H. Brongersma, E. Richard, I. Vervoort, H. Bender, W. Vandervorst, S. Lagrange, G. Beyer, and K. Maex, "Two-step room temperature grain growth in electroplated copper," *Journal of Applied Physics,* vol. 86, p. 3642, 1999.

[130] K. Pantleon and M. A. J. Somers, "In situ investigation of the microstructure evolution in nanocrystalline copper electrodeposits at room temperature," *Journal of Applied Physics,* vol. 100, Dec 2006.

[131] W. Wu, D. Ernur, S. H. Brongersma, M. Van Hove, and K. Maex, "Grain growth in copper interconnect lines," *Microelectronic Engineering,* vol. 76, pp. 190-194, Oct 2004.

[132] V. Weihnacht and W. Brückner, "Abnormal grain growth in {111} textured Cu thin films," *Journal of Applied Physics,* vol. 418, pp. 136-144, 2002.

[133] C. H. Seah, G. Z. You, C. Y. Li, and R. Kumar, "Characterization of electroplated copper films for three-dimensional advanced packaging," *Journal of Vacuum Science & Technology B,* vol. 22, pp. 1108-1113, May-Jun 2004.

[134] S. P. Hau-Riege and C. V. Thompson, "In situ transmission electron microscope studies of the kinetics of abnormal grain growth in electroplated copper films," *Applied Physics Letters,* vol. 76, pp. 309-311, Jan 2000.

[135] M. Stangl, M. Lipták, A. Fletcher, J. Acker, J. Thomas, H. Wendrock, S. Oswald, and K. Wetzig, "Influence of initial microstructure and impurities on Cu room-temperature recrystallization (self-annealing)," *Microelectronic Engineering,* vol. 85, pp. 534-541, 2008.

[136] J. M. E. Harper, C. Cabral Jr, P. C. Andricacos, L. Gignac, I. C. Noyan, K. P. Rodbell, and C. K. Hu, "Mechanisms for microstructure evolution in electroplated copper thin films near room temperature," *Journal of Applied Physics,* vol. 86, p. 2516, 1999.

[137] M. T. Pérez-Prado and J. J. Vlassak, "Microstructural evolution in electroplated Cu thin films," *Journal of Applied Physics,* vol. 47, pp. 817-823, 2002.

[138] Q. T. Jiang and M. E. Thomas, "Recrystallization effects in Cu electrodeposits used in fine line damascene structures," *Journal of Vacuum Science & Technology B: Microelectronics and Nanometer Structures,* vol. 19, pp. 762-766, 2001.

[139] D. Kwon, H. Park, S. Ghosh, C. M. Lee, H. T. Jeon, and J. G. Lee, "Recrystallization of the copper films deposited by pulsed electroplating on ECR plasma-cleaned copper seed layers," *Journal of the Korean Physical Society,* vol. 44, pp. 1108-1112, May 2004.

[140] S. Lagrange, S. H. Brongersma, M. Judelewicz, A. Saerens, I. Vervoort, E. Richard, R. Palmans, and K. Maex, "Self-annealing characterization of electroplated copper films," *Microelectronic Engineering,* vol. 50, pp. 449-457, Jan 2000.

[141] W. H. Teh, L. T. Koh, S. M. Chen, J. Xie, C. Y. Li, and P. D. Foo, "Study of microstructure and resistivity evolution for electroplated copper films at near-room temperature," *Microelectronics Journal,* vol. 32, pp. 579-585, 2001.

[142] K. B. Yin, Y. D. Xia, C. Y. Chan, W. Q. Zhang, Q. J. Wang, X. N. Zhao, A. D. Li, Z. G. Liu, M. W. Bayes, and K. W. Yee, "The kinetics and mechanism of room-temperature microstructural evolution in electroplated copper foils," *Scripta Materialia,* vol. 58, pp. 65-68, 2008.

[143] K. B. Yin, Y. D. Xia, W. Q. Zhang, Q. J. Wang, X. N. Zhao, A. D. Li, Z. G. Liu, X. P. Hao, L. Wei, C. Y. Chan, K. L. Cheung, M. W. Bayes, and K. W. Yee, "Room-temperature microstructural evolution of electroplated Cu studied by focused ion beam and positron annihilation lifetime spectroscopy," *Journal of Applied Physics,* vol. 103, pp. 066103-3, 2008.

[144] H. Lee, W. D. Nix, and S. S. Wong, "Studies of the driving force for room-temperature microstructure evolution in electroplated copper films," *Journal of Vacuum Science & Technology B,* vol. 22, pp. 2369-2374, Sep-Oct 2004.

[145] V. A. Vas'ko, I. Tabakovic, S. C. Riemer, and M. T. Kief, "Effect of organic additives on structure, resistivity, and room-temperature recrystallization of electrodeposited copper," *Microelectronic engineering,* vol. 75, pp. 71-77, 2004.

[146] W. Robl, M. Melzl, B. Weidgans, R. Hofmann, and M. Stecher, "Last Metal Copper Metallization for Power Devices," in *IEEE Transactions on Semiconductor Manufacturing*, 2008, pp. 358-362.

[147] C. Detavernier, S. Rossnagel, C. Noyan, S. Guha, C. Cabral, and C. Lavoie, "Thermodynamics and kinetics of room-temperature microstructural evolution in copper films," *Journal of Applied Physics,* vol. 94, pp. 2874-2881, Sep 2003.

[148] G. E. Dieter and D. Bacon, *Mechanical metallurgy*: McGraw-Hill, 1988.

[149] D. N. Lee and H. J. Lee, "Self-annealing textures of copper damascene interconnects," in *Recrystallization and Grain Growth, Pts 1 and 2*. vol. 467-470, 2004, pp. 1333-1338.

[150] W. Dong, H. Zhang, J. W. Zheng, and H. W. Sheng, "Self-annealing of electrodeposited copper thin film during room temperature storage," *Materials Letters,* vol. 62, pp. 1589-1591, Apr 2008.

[151] T. Ritzdorf, L. Graham, S. Jin, C. Mu, and D. Fraser, "Self-annealing of electrochemically deposited copper films in advanced interconnect applications," 1998, pp. 166-168.

[152] C. Detavernier, D. Deduytsche, R. L. Van Meirhaeghe, J. De Baerdemaeker, and C. Dauwe, "Room-temperature grain growth in sputter-deposited Cu films," *Applied Physics Letters,* vol. 82, pp. 1863-1865, Mar 2003.

[153] H. Wendrock, W. Bruckner, M. Hecker, T. G. Koetter, and H. Schloerb, "Room temperature grain growth in electroplated copper thin films," *Microelectronics Reliability,* vol. 40, pp. 1301-1304, Aug-Oct 2000.

[154] C. Cabral, P. C. Andricacos, L. Gignac, I. C. Noyan, K. P. Rodbell, T. M. Shaw, R. Rosenberg, J. M. E. Harper, P. W. DeHaven, and P. S. Locke, "Room temperature evolution of microstructure and resistivity in electroplated copper films," in *Advanced Metallization Conference*, Colorado, 1998, p. 81.

[155] M. Stangl and M. Militzer, "Modeling self-annealing kinetics in electroplated Cu thin films," *Journal of Applied Physics,* vol. 103, Jun 2008.

[156] H. Lee, S. S. Wong, and S. D. Lopatin, "Correlation of stress and texture evolution during self- and thermal annealing of electroplated Cu films," *Journal of Applied Physics,* vol. 93, pp. 3796-3804, Apr 2003.

[157] P. Chaudhari, "Grain Growth and Stress Relief in Thin Films," in *Journal of Vacuum Science and Technology*. vol. 9, 1972, pp. 520-522.

[158] Q. T. Jiang, R. Mikkola, B. Carpenter, and M. E. Thomas, "Room temperature film property changes in electro-deposited Cu thin films," 1998, pp. 177-181.

[159] Q. Z. Hong, J. M. E. Harper, and S. Q. Hong, "Stresses and morphological instabilities in silicide/polycrystalline Si layered structures." vol. 62, 1993, p. 2637.

[160] P. G. Shwemon, *Transformations in Metals*. New York: McGraw-Hill, 1969.

[161] C. M. F. Rae and D. A. Smith, "On the Mechanisms of Grain-Boundary Migration," *Philosophical Magazine a-Physics of Condensed Matter Structure Defects and Mechanical Properties,* vol. 41, pp. 477-492, 1980.

[162] D. W. Gan, P. S. Ho, R. Huang, J. Leu, J. Maiz, and T. Scherban, "Isothermal stress relaxation in electroplated Cu films. I. Mass transport measurements," *Journal of Applied Physics,* vol. 97, pp. 103531-1-103531-8, May 2005.

[163] D. Zoellner and P. Streitenberger, "Three-dimensional normal grain growth: Monte Carlo Potts model simulation and analytical mean field theory," in *Scripta materialia*. vol. 54: Elsevier, 2006, pp. 1697-1702.

[164] M. P. Anderson, D. J. Srolovitz, G. S. Grest, and P. S. Sahni, "Computer simulation of grain growth--I. Kinetics," in *Acta metallurgica,*. vol. 32: Elsevier, 1984, pp. 783-791.

[165] G. Liu, H. Yu, X. Song, and X. Qin, "A new model of three-dimensional grain growth: theory and computer simulation of topology-dependency of individual grain growth rate," in *Materials & Design*. vol. 22: Elsevier, 2001, pp. 33-38.

[166] M. Hillert, "On the theory of normal and abnormal grain growth," in *Acta Metallurgica*. vol. 13: Elsevier, 1965, pp. 227-238.

[167] W. Blum and X. H. Zeng, "A simple dislocation model of deformation resistance of ultrafine-grained materials explaining Hall-Petch strengthening and enhanced strain rate sensitivity," *Acta Materialia,* vol. 57, pp. 1966-1974, 2009.

[168] E. A. Holm, M. A. Miodownik, and A. D. Rollett, "On abnormal subgrain growth and the origin of recrystallization nuclei," *Acta Materialia,* vol. 51, pp. 2701-2716, 2003.

[169] F. J. Humphreys, "A unified theory of recovery, recrystallization and grain growth, based on the stability and growth of cellular microstructures--I. The basic model," *Acta Materialia,* vol. 45, pp. 4231-4240, 1997.

[170] Y. L. Shen and U. Ramamurty, "Constitutive response of passivated copper films to thermal cycling," in *Journal of Applied Physics*. vol. 93, 2003, p. 1806.

[171] H. Huang and F. Spaepen, "Tensile testing of free-standing Cu, Ag and Al thin films and Ag/Cu multilayers," in *Acta Materialia*. vol. 48: Tarrytown, NY: Elsevier Science Inc., 1996-, 2000, pp. 3261-3270.

[172] A. J. Kalkman, A. H. Verbruggen, and G. Janssen, "Young's modulus measurements and grain boundary sliding in free-standing thin metal films," in *Applied Physics Letters*. vol. 78, 2001, p. 2673.

[173] S. P. Baker, R. P. Vinci, and T. Arias, "Elastic and anelastic behavior of materials in small dimensions," in *MRS bulletin*. vol. 27, 2002, pp. 26–29.

[174] S. P. Baker, A. Kretschmann, and E. Arzt, "Thermomechanical behavior of different texture components in Cu thin films," in *Acta Materialia*. vol. 49: Elsevier, 2001, pp. 2145-2160.

[175] S. H. Hong, K. S. Kim, Y. M. Kim, J. H. Hahn, C. S. Lee, and J. H. Park, "Characterization of elastic moduli of Cu thin films using nanoindentation technique," in *Composites Science and Technology*. vol. 65: Elsevier, 2005, pp. 1401-1408.

[176] Y. Xiang, X. Chen, and J. J. Vlassak, "The mechanical properties of electroplated Cu thin films measured by means of the bulge test technique." vol. 695: Warrendale, Pa.; Materials Research Society; 1999, 2002, pp. 189-196.

[177] G. Andreasen, P. L. Schilardi, O. Azzaroni, and R. C. Salvarezza, "Thermal annealing of patterned metal surfaces," *Langmuir,* vol. 18, pp. 10430-10434, Dec 2002.

[178] K. Gall, M. L. Dunn, Y. Zhang, and B. A. Corff, "Thermal cycling response of layered gold/polysilicon MEMS structures," *Mechanics of Materials,* vol. 36, pp. 45-55, 2004.

[179] D. Weiss, "Deformation mechanisms in pure and alloyed copper films," in *PhD thesis*, 2000.

[180] I. Dutta, C. Park, and J. Vella, "Effect of internal stresses on thermo-mechanical stability of interconnect structures in microelectronic devices," *Materials Science and Engineering: A,* vol. 421, pp. 118-132, 2006.

[181] M. D. Thouless, "Effect of Surface-Diffusion on the Creep of Thin-Films and Sintered Arrays of Particles," *Acta Metallurgica Et Materialia,* vol. 41, pp. 1057-1064, Apr 1993.

[182] U. Welzel and E. J. Mittemeijer, "Stress evolution in thin films; diffusion and reactions," in *International Workshop on Diffusion and Stresses*, Lillafured, HUNGARY, 2006, pp. 71-78.

List of Publications

[1]   R. Huang, W. Robl, H. Ceric, T. Detzel, and G. Dehm, "Stress, Sheet Resistance, and Microstructure Evolution of Electroplated Cu films during Self-annealing," *IEEE Trans. Dev. Mater. Rel.,* vol. 10, no. 1, pp. 47–54, 2010.

[2]   R. Huang, C. A. Taylor, S. Himmelsbach, H. Ceric, and T. Detzel, "Apparatus for Measuring Local Stress of Metallic Films, Using an Array of Parallel Laser Beams during Rapid Thermal Processing," *Meas. Sci. Technol.,* vol. 21, no. 5, pp. 55702–55710(9), 2010.

[3]   R. Huang, W. Robl, T. Detzel, and H. Ceric, "Modeling of Stress Evolution of Electroplated Cu Films during Self-annealing," in *Proc. IRPS,* pp. 911–917, 2010.

[4]   R. Huang, W. Robl, G. Dehm, H. Ceric, and T. Detzel, "Disparate Tendency of Stress Evolution of Thin and Thick Electroplated Cu Films at Room Temperature," in *Proc. IPFA,* pp. 1–6, 2010.

[5]   M. Lederer, J. Zarbakhsh, R. Huang, T. Detzel, and B. Weiss, "Thermomechanical Stresses in Copper Films at Elevated Temperature," *J. Microelectro. Elect. Packag.,* vol. 7, no. 2, pp. 99-104(6), 2010.

[6]   J. Zarbakhsh, M. Lederer, R. Huang, T. Detzel, and B. Weiss, "Modeling of Multi-temperature-cycle Wafer Curvature," in *Proc. ITherm,* pp. 1–6, 2010.

[7]   M. Lederer, J. Zarbakhsh, R. Huang, T. Detzel, and B. Weiss, "Thermomechanical Stresses in Copper Films at Elevated Temperature," in *Proc. HiTEC,* pp. 1–7, 2010.

[8]   J. Zarbakhsh, T. Detzel, R. Huang, M. Leicht, P. Nelle, and S. Woehlert, "Prediction of Wafer Bow through Thermomechanical Simulation of Patterned Hard Coated Copper Films," in *Proc. EuroSimE,* pp, 1–5, 2008.

Curriculum Vitae

M.Sc. Rui Huang

Date of Birth: 15.11.1980

Nationality: Chinese

Marital status: Single

Address: Chiemgaustraße 64a

81549 Munich

Germany

Email: hrzjdx@hotmail.com

Educational Experience

08/2006 - 11/2012   Vienna University of Technology (Austria)

Institute of Microelectronics

Dissertation

10/2003 - 11/2005   University of Kiel (Germany)

Materials Science and Engineering

Master of Science (M.Sc.)

09/1999 - 07/2003   Zhejiang University (China)

Materials Science and Engineering/Business Administration

Bachelor of Engineering (B.Eng.)/Bachelor of Business Administration (BBA)

Working Experience

10/2010 - now   Infineon Technologies AG, Munich, Germany

       Simulation engineer for thermo-mechanical simulation for chip-package-board interactions with FEM tool-ANSYS

08/2006 - 09/2010 KAI Kompetenzzentrum Automobil- und Industrieelektronik GmbH, Villach, Austria

       Project engineer in the project "Robust Metallization and Interconnect'' at Infineon Technologies Austria AG

12/2005 - 04/2006 Robert Bosch GmbH, Stuttgart, Germany

       Intern in Applied Research-Physical Technologies Department

12/2005 - 04/2006 University of Kiel, Kiel, Germany

       Research Assistant in Nanotechnology Laboratory

07/2003 - 10/2003 BOC Gases Co.LTD , Suzhou, China

       Trainee